

## ABSTRACT

### A Method for Replicating Ice Accretion Roughness Using Multi-Scale Analog Distributions

John-Mark Clemenson, M.S.M.E

Mentor: Stephen T. McClain, Ph.D.

A new approach of creating an analog surface for a surface with natural roughness is presented based on the hypothesis that the dominant skin friction and heat transfer augmentation mechanisms are 1) the vortex shedding from the roughness elements and 2) the interaction of the shed vortices with the next downstream roughness elements. An autocorrelation function was employed on a real ice surface to capture the root-mean-square-roughness height, the primary streamwise wavelength, and the aspect ratio of surface microscales. Two distributions of deterministic roughness, one of ellipsoids and one of elliptical cones, were created to match the primary features of the real ice surface. This work describes the analog surface creation method and characterizes the convective enhancement and velocity boundary layer development of the analog surfaces. The convective enhancement and velocity boundary layer results associated with the analog surfaces are then compared to those of the real ice surface.

A Method for Replicating Ice Accretion Roughness Using Multi-Scale Analog Distributions

by

John-Mark Clemenson, B.S.M.E

A Thesis

Approved by the Department of Mechanical Engineering

---

Kenneth Van Treuren, Ph.D., Chairperson

Submitted to the Graduate Faculty of  
Baylor University in Partial Fulfillment of the  
Requirements for the Degree  
of  
Masters of Science in Mechanical Engineering

Approved by the Thesis Committee

---

Stephen T. McClain, Ph.D., Chairperson

---

Yue Ling, Ph.D.

---

Enrique Blair, Ph.D.

Accepted by the Graduate School

May 2018

---

J. Larry Lyon, Ph.D., Dean

Copyright © 2018 by John-Mark Clemenson

All rights reserved

## TABLE OF CONTENTS

LIST OF FIGURES .....	viii
LIST OF TABLES .....	xi
NOMENCLATURE .....	xii
ACKNOWLEDGMENTS .....	xvii
DEDICATION .....	xix
CHAPTER ONE .....	1
Introduction.....	1
Motivation.....	1
Objectives .....	4
Presentation Outline.....	4
CHAPTER TWO .....	5
Technical Background .....	6
Surface Roughness.....	6
Surface Analysis .....	10
Height Parameters.....	11
Spatial Parameters.....	12
Hybrid Parameters .....	12
Individual Feature Parameters .....	13
Predictive Method Using Surface Statistics.....	14
Fluid Mechanics and Heat Transfer .....	15

Viscous Boundary Layers .....	15
Thermal Boundary Layers .....	17
Airfoils .....	20
Aircraft Icing.....	22
Icing Terms .....	22
Ice Accretion Process.....	23
Ice Accretion Modeling .....	24
Recent Ice Roughness Investigations.....	27
Real Ice Roughness Surface.....	28
Laser Scanning.....	29
Real Ice Surface Creation .....	32
CHAPTER THREE .....	36
Materials and Methodology .....	36
Analog Surfaces .....	36
Autocorrelation of Real Ice Surface .....	37
Analog Surface Generation.....	39
Manufacturing Model Surfaces.....	45
Instrumented Test Plate.....	45
Plexiglas Sub-Plate .....	46
Instrumentation and Wiring .....	47
Mylar Film Heaters .....	49
Aerodynamic Features .....	50
Ceiling Insert for Flow Acceleration .....	50

Ceiling Insert Design .....	50
Ceiling Insert Construction .....	52
Experimental Setup and Procedure .....	52
Convection Measurements .....	55
Velocity Boundary Layer Measurements .....	60
Data Reduction and Uncertainty .....	62
Convection Measurements .....	62
Air Properties .....	64
Thermocouple Calibration .....	65
Smooth Surface Validation .....	66
Uncertainty Analysis .....	66
Velocity Boundary Layer Measurements .....	68
CHAPTER FOUR .....	71
Results and Discussion .....	71
Convection Results .....	71
Discussion .....	83
Velocity Boundary Layer Results .....	84
CHAPTER FIVE .....	87
Conclusions .....	87
Summary of Work .....	87
Future Work .....	89
APPENDIX .....	90
APPENDIX A .....	91

REFERENCES .....104

## LIST OF FIGURES

Figure 2.1	Effective sand-grain roughness correlation of Dirling [15].....	8
Figure 2.2:	Velocity boundary layer development on a flat plate (not to scale) .....	15
Figure 2.3:	Thermal boundary layer on a flat plate (not to scale) .....	18
Figure 2.4:	Surface pressure distribution on an airfoil .....	20
Figure 2.5:	Boundary layer separation on an airfoil (not to scale).....	21
Figure 2.6:	Early stage ice accretion on airfoil leading edge [34].....	24
Figure 2.7:	Modes of energy transfer for an unheated airfoil in icing in icing conditions [35] .....	25
Figure 2.8:	Comparison of measured roughness height with predicted sand-grain roughness height [37].....	27
Figure 2.9	Topographies of the 113012.04 real ice surface displaying a) ice thickness, and b) ice roughness.....	29
Figure 2.10:	Coordinate systems used in the SOM method [44] .....	30
Figure 2.11:	Surface thickness distribution of laser scanned ice roughness points [8]..	31
Figure 2.12:	Surface height distribution of laser scanned ice roughness points [8].....	32
Figure 2.13:	Resampled surface height map after quadratic interpolation [8] .....	33
Figure 2.14:	Surface panel assemblies of the a) 113012.04_IRT, and b) 113012.04_RealIce [41].....	34
Figure 2.15	Local Stanton number measurements presented for surface comparison in a) flow with negligible acceleration, and b) accelerated flow .....	34
Figure 3.1:	a) Region of 113012.04 Surface Analyzed for Surface Characteristics and b) Autocorrelation result.....	38
Figure 3.2:	Primary autocorrelation features replicated for analog surfaces.....	39

Figure 3.3:	Multi-scale roughness distribution of hemispheres .....	40
Figure 3.4:	Autocorrelation comparison of a) real ice surface and b) ellipsoid surface, and c) elliptical cone surface.....	41
Figure 3.5:	Streamwise centerline autocorrelation height comparison .....	42
Figure 3.6:	Unwrapped and Wind-Tunnel Scaled RMS Roughness Height Variation for the 113012.04 Surface and the Roughness Height Scaling Function ..	43
Figure 3.7:	Solid models of a) real ice surface, b) ellipsoidal surface, and c) elliptical cone surface .....	44
Figure 3.8	Surface statistics of the 113012.04 surface and analog surfaces: a) root- mean-square roughness height, b) skewness, c) equivalent sand-grain roughness .....	44
Figure 3.9:	Solid model of test plate [3].....	46
Figure 3.10:	Plexiglas sub-plate [3].....	47
Figure 3.11:	Side view of test plate showing thermocouple placement from the leading edge of the Plexiglas sub-plate (dimensions in inches, flow is from left to right) [3] .....	48
Figure 3.12:	Layout of the heated sections on the Plexiglas sub-plate (dimensions in inches, flow is from left to right) [3].....	49
Figure 3.13:	Scaled airfoil velocity variation and design velocity variation [7] .....	51
Figure 3.14:	Solid model of ceiling insert [7] .....	53
Figure 3.15:	Side view of experimental setups for a) the convection tests and b) velocity boundary layer tests (not to scale) [7].....	54
Figure 3.16:	Side view of convection test section [7] .....	55
Figure 3.17:	Modified wood cart outfitted with experimental equipment [7].....	58
Figure 3.18	Wind tunnel ceiling with two-dimensional traversing system [7] .....	61
Figure 3.19	Heated section one-dimensional heat schematic (not to scale).....	62
Figure 3.20	Hot-film probe calibration plot.....	69

Figure 4.1:	Convection coefficient contour maps of plastic surfaces without ceiling insert for the a) 113012.04 RealIce surface, b) ellipsoid surface, and c) elliptical cone surface .....	73
Figure 4.2:	Convection coefficient contour maps of aluminum surfaces without ceiling insert for the a) 113012.04 RealIce surface, b) ellipsoid surface, and c) elliptical cone surface .....	74
Figure 4.3:	Convection coefficient contour maps of plastic surfaces with ceiling insert for the a) 113012.04 RealIce surface, b) ellipsoid surface, and c) elliptical cone surface .....	75
Figure 4.4:	Convection coefficient contour maps of aluminum surfaces with ceiling insert for the a) 113012.04 RealIce surface, b) ellipsoid surface, and c) elliptical cone surface .....	76
Figure 4.5:	Stanton number plots for a) plastic surfaces with negligible acceleration, b) aluminum surfaces with negligible acceleration, c) plastic surfaces with acceleration, and d) aluminum surfaces with acceleration .....	77
Figure 4.6	Stanton number plots comparing the IRT surfaces, analog surfaces, and the 113012.04 Real Ice surface in flow with negligible acceleration: a) Plastic IRT cones and elliptical cones, b) plastic IRT hemispheres and ellipsoids, and c) aluminum IRT cones and elliptical cones.....	78
Figure 4.7	Stanton number plots comparing IRT surfaces, analog surfaces, and the 113012.04 Real Ice surface in accelerated flow: a) plastic IRT cones and elliptical cones, b) plastic IRT hemispheres and ellipsoids, and c) aluminum IRT cones and elliptical cones.....	79
Figure 4.8	Velocity boundary layer traces with negligible acceleration for the a) 113012.04 Real Ice surface, b) ellipsoid surface, and c) elliptical cone surface .....	85
Figure 4.9	Velocity boundary layer traces with acceleration for the a) 113012.04 Real Ice surface, b) ellipsoid surface, and c) elliptical cone surface .....	86

## LIST OF TABLES

Table 3.1:	Comparison of sample statistics from the 113012.04 surface with sample statistics from the ellipsoidal analog and elliptical cone analog surfaces .....42
Table 3.2:	Conduction parameter values [4] .....65
Table 3.3:	Convective heat transfer coefficient measurement uncertainty [7] .....67

## NOMENCLATURE

$a$	Streamwise microscale
$A_f$	Element frontal area
$A_{\text{pix}}$	Pixel area (4.00E-04 in <sup>2</sup> )
$A_S$	Wetted surface area
$A_t$	Total area of heated section
$b$	Spanwise microscale
$b^n$	Winning codebook vector
$B_T$	Correlated uncertainty (1.4 K)
$c$	Airfoil chord length
$c_f$	Skin friction coefficient
$C_k$	Conduction parameter for the $k^{\text{th}}$ heated section (0.9, 0.9, 1.05, 1.1, 1.05)
$c_p$	Specific heat of fluid
$C_p$	Pressure coefficient
$D$	Roughness element diameter
$D_{\text{mean}}$	Average roughness element diameter
$E$	Voltage across heater
$F_D$	Diameter scaling factor
$F_s$	Surface geometry scaling factor (10)
$F_t$	Transition function
$F_x$	Spanwise scaling factor

$h$	Convective heat transfer (convection) coefficient
$H$	Roughness element height OR local ceiling insert height
$H_s$	Distance from test plate surface to test section ceiling without insert (12")
$I$	Current through heater
$k_f$	Thermal conductivity of fluid
$k_p$	Thermal conductivity of Plexiglas (0.205 W/mK)
$L_{ha}$	Length of heated section
$l_t$	Transition length
$N$	Measurement sample size
$N_{f,stag}$	Freezing fraction at stagnation point
$N_x^j$	Orthogonal distance from an ice surface point to the mean ice shape
$P$	Roughness element spacing
$P_{mean}$	Average roughness element spacing
$Pr$	Prandtl number
$Q_{conv}$	Convection term in data reduction equation
$Q_{cond}$	Conduction term in data reduction equation
$Q_{gen}$	Heat generation term in data reduction equation
$Q_{rad}$	Radiation term in data reduction equation
$q''_w$	Wall heat flux
$r_a$	Leading edge radius of curvature of NACA 0012 airfoil
$R_{AC}$	Autocorrelation root-mean-square height
$Re$	Reynolds number
$R_q$	Roughness height root-mean-square

$s$	Surface direction along airfoil
$S$	Standard deviation (in uncertainty calculations)
$S$	Shape factor (in roughness density parameter)
$S_E$	Element diameter standard deviation
$S_x$	Surface scaling function
$St$	Stanton number
$Ssk$	Skewness
$T_\infty$	Freestream temperature
$T_{IR}$	IR camera temperature reading
$T_s$	Surface temperature
$T_{SS}$	Calibrated subsurface thermocouple temperature
$T_{UP}$	Calibrated under plate thermocouple temperature
$t$	Student's t-value
$t_p$	Plexiglas sub-plate thickness (0.72")
$u$	Streamwise velocity
$U$	Uncertainty
$U_\infty$	Freestream velocity
$U_{CI}$	Cut in velocity (5 m/s)
$U_e$	Local freestream velocity
$V_{eff}$	Effective velocity measured by hot-film wire(s)
$V_{meas}$	Measured velocity by Pitot-static probe
$V_N$	Velocity normal to hot-film wire
$V_T$	Velocity tangential to hot-film wire

$W_{ha}$	Width of heated section
$x$	Streamwise location on plate
$x_{cr}$	Critical distance for flow transition
$x_k$	Sand-grain equivalent roughness height in LEWICE
$x_t$	Transition location
$w$	Wall-normal velocity
$y$	Height above mean roughness elevation
$z$	Wall-normal distance from plate surface
<i>Greek</i>	
$\alpha$	Thermal diffusivity OR angle of wire of x-array probe
$\delta$	Velocity boundary layer height
$\delta_T$	Thermal boundary layer height
$\Delta t_s$	Ice accretion time
$\Delta \theta$	Change in momentum thickness
$\varepsilon$	Emissivity (0.95)
$\varepsilon$	Eccentricity (from autocorrelation)
$\lambda$	Roughness density (in roughness equations)
$\lambda$	Primary wavelength (in autocorrelation descriptions)
$\zeta$	Dummy variable representing $x$ in Stanton number correlations
$\kappa$	Tangential velocity attenuation factor (0.115)
$\mu$	Dynamic fluid viscosity
$\nu$	Kinematic fluid viscosity
$\xi$	Unheated starting length (1.7285")

$\rho$	Fluid density
$\rho_{ice}$	Ice density
$\sigma$	Stefan-Boltzmann constant (5.67E-8 W/m <sup>2</sup> K <sup>4</sup> )
$\tau_w$	Wall shear stress

### *Subscripts*

TC,cal	Thermocouple temperature measurement during calibration
TC,test	Thermocouple temperature measurement during test
IR,cal	Infrared temperature measurement during calibration

### *Abbreviations*

IRT	Icing research tunnel
LWC	Liquid water content
MVD	Median volumetric diameter
RMH	Roughness maximum height
RMS	Root-mean-square

## ACKNOWLEDGMENTS

I owe much thanks to Dr. Stephen McClain for serving as my mentor and providing not only academic knowledge, but valuable life lessons and comedic relief as well. His guidance, support, and patience throughout this project are sincerely appreciated. I would also like to thank Dr. Yue (Stanley) Ling and Dr. Enrique (Erik) Blair for serving as members of my thesis committee.

Thank you to my predecessors in the Baylor Icing Group, Logan Tecson, Chris Walker, Tim Shannon, and Matt Hawkins, for beginning the work on this project that allowed an opportunity for expansion. I offer my sincerest thanks to Mr. Ashley Orr for his time and assistance in creating the analog roughness surfaces used in this investigation. To my fellow graduate students, Jaime McCarrell, Zac Williams, Taber Miyauchi, Nic Mosser, and Berkley Bonjonia, thank you for your assistance with this project, your friendship, and for providing amusement in the long hours we spent together.

I would also like to thank my family and friends for their constant love and support that made this document possible. Mom and Dad, thank you for instilling strong values in me and for your sacrifices that provided me an outstanding education. To my siblings, Michael David, Caitlin, and Mariela, thank you for your friendship, phone calls, and continuous encouragement throughout this process. Finally, I would like to thank my Lord and Savior, Jesus Christ, for making the ultimate sacrifice to allow me to be where I am today. I attribute all of my gifts and talents to Him.

The efforts reported in this work were supported as part of NASA Collaborative Agreement No. NNX16AN32A. Any opinions presented in this work are those of the author and do not reflect the views of NASA or the United States government.

## DEDICATION

To my family

## CHAPTER ONE

### Introduction

#### *Motivation*

Understanding fluid flow interactions with surfaces exhibiting natural random roughness has long been a topic of research as it is significant in many engineering applications. For example, roughness in conduits (channels and pipes), ship hull roughness, gas-turbine blade roughness, and in-flight ice accretion roughness all affect performance and efficiency in their respective applications. In comparison with a smooth surface, a roughened surface will experience higher skin friction leading to increased drag and, in the case of heat transfer, experience increased rates of convection.

Characterizing natural random roughness can be difficult because random roughness often exhibits repeating patterns at a wide range of wavelengths in all surface directions. In the 1930's, Nikuradse [1] and Schlichting [2] conducted experiments to characterize the effect of surface roughness on skin friction. Nikuradse used sand grains cemented to surfaces to create roughness and investigated the skin friction in rough tubes, channels, and plane surfaces. To simplify the surface roughness descriptions, Schlichting used ordered arrays of spheres, spherical segments, and cones in consistent patterns with varying roughness density to determine skin friction in a roughened channel. The use of geometric shapes in ordered arrays allowed for an equivalent sand-grain roughness to be determined based on the work of Nikuradse. Experimental studies of roughness since have followed the model of Schlichting by attempting to capture skin friction and heat

transfer enhancement using ordered arrays of geometric shapes such as cones and spheres. The use of deterministic roughness features allows for simple mathematical descriptions of rough surfaces leading to direct implementation of conceptual models, faster generation of computational grids, and easier generation of solid models for experimental studies.

This study focuses primarily on in-flight ice accretion roughness in an attempt to aid in the improvement of NASA's ice accretion prediction code, LEWICE. The goal of LEWICE is to accurately predict the size and shape of an ice accretion for given icing conditions. The code uses historical roughness correlations based on the equivalent sand-grain roughness model and the discrete element method to predict the convective heat transfer from the ice roughness. While LEWICE is capable of predicting the convective heat transfer of ice roughness, there are still areas for improvement in the code as real ice roughness differs in several ways from the surfaces used to create the LEWICE correlations. First, the methods used simulate roughness in systematic arrays of basic geometries whereas real ice roughness develops in random distributions of element size and location. Additionally, real ice roughness characteristics vary in the flow direction with a smooth-to-rough transition region which is not captured by ordered arrays of elements with constant height. Lastly, ice accretions on airfoils experience accelerating flow over the ice roughened surface due to the shape of the airfoil.

Multiple investigations have isolated LEWICE's areas for improvement to better understand heat transfer correlations. Studies done in the Baylor University Subsonic Wind Tunnel (BUSWT) have advanced the understanding of ice roughness by continually adding characteristics of ice accretions. Tecson [3] and Walker [4] used a

Lagrangian droplet simulator to create a random roughness distribution to capture the random nature of ice. The surfaces created for those studies exhibited an abrupt smooth-to-rough transition and constant roughness properties downstream of the leading edge. However, studies of laser scanned ice accretions showed that roughness properties reach a maximum height and decay in the flow direction with a transition region that is not abrupt [5,6]. Shannon [7] progressed the study of ice roughness by creating new surfaces that included simulated roughness element variations in the flow direction as measured by laser scans of real ice accretions. Hawkins [8] used a laser scan of an ice accretion to create a surface model of real ice roughness from a NACA 0012 airfoil and investigated the convective heat transfer of the real surface.

In this study, a new method of analog surface roughness creation is proposed. Upon performing statistical analysis of the laser scanned ice accretion studied by Hawkins, analog surfaces comprised of elliptical cones and ellipsoids were created to match the surface statistics of the real ice accretion in the region of maximum roughness. An autocorrelation analysis was performed to capture the real ice roughness pattern including the accretion ridge spacing and the root mean square height. Elliptical roughness elements were implemented to imitate the ridge-like structure found in real ice roughness. The surfaces were generated based on the assumption that the processes leading to increased heat transfer and skin friction are the vortices shed from individual roughness elements and the interaction of those shed vortices with the next downstream roughness elements.

A base distribution of random roughness elements was created using a Lagrangian droplet simulator and then modified to match multiple length scales present in the real ice

surface. The analog surfaces match the root-mean-square height, the aspect ratio of surfaces microscales, and the distance between rows of roughness elements in the region of maximum roughness. Through the use of this method, streamwise variations in the roughness statistics of the real ice surface are captured, the ridge-like structure of real ice accretions is present in the elliptical analog surfaces, and the spacing between elements on the analog surfaces allows for equivalent vortex shedding interaction to that found on the real ice surface.

### *Objectives*

The objectives of this study are to 1) create a method to analyze laser-scanned ice accretions and generate simulated roughness elements to match the characteristics found in real ice accretions, 2) generate two surfaces analogous to the real ice surface tested by Hawkins, 3) create and test the surfaces using the same methods as Hawkins, and 4) measure the convective heat transfer and boundary layer development for comparison between the real ice surface and the two analog surfaces.

All surfaces were made of both ABS plastic and machined aluminum. Heat transfer and velocity boundary layer measurements were performed in flows with negligible acceleration and in flows matching the acceleration found on a NACA 0012 airfoil.

### *Presentation Outline*

Chapter Two presents a technical background of surface roughness, autocorrelation analysis, aircraft icing, fluid mechanics, and heat transfer. Chapter Three outlines the experimental procedures and testing apparatuses used for data collection, as

well as the data reduction process and uncertainty calculations. Chapter Four presents the results from the convective heat transfer and boundary layer tests and discusses the significance of results. Chapter Five provides conclusions drawn from this investigation and proposes suggestions for future work.

## CHAPTER TWO

### Technical Background

#### *Surface Roughness*

Surface roughness has long remained a topic of thermal engineering experimental studies because of its appearance in numerous situations and the effect it has on flow fields and heat transfer enhancement. An early experiment performed by Nikuradse [1] implemented the use of sand grains cemented to the walls of pipes and channels to create measurable roughness. The study investigated the effect that the sand grain roughness had on the turbulent boundary layer and derived correlations for flows with large Reynolds numbers. Schlichting [2] continued the work of Nikuradse by investigating boundary layers in roughened channels. However, Schlichting performed the experiments using geometric shapes such as spheres, spherical segments, cones, and short and long angles. Schlichting was able to relate his work to Nikuradse's by deriving a relation known as the "equivalent sand roughness" in which the size of the sand grain studied by Nikuradse has the same resistance of the geometric shapes investigated by Schlichting. This relationship became useful to many researchers in cataloging the effect of various surface geometries in terms of a common factor.

Since then, many experimental studies have employed the use of deterministic roughness features to simplify the problem that roughness poses in engineering settings. Hama [9], Clauser [10], and Rotta [11] furthered the study of rough surfaces by deriving a skin-friction law dependent on the downward shift found in the inner variable velocity

profile, the roughness geometry, and the density of the roughness. The concept of the law is to express the inner variable velocity profile deficit in terms of the density of the deterministic surface pattern. However, the skin-friction law was only applicable to flows with a zero pressure gradient. Dvorak [12] expounded on the work of his predecessors by using the skin-friction law, the momentum integral equation, and an auxiliary equation to describe the shape factor of turbulent boundary layers under non-zero pressure gradients. Using the equivalent roughness height and a known roughness density, Dvorak was able to correlate a predictive method to find shape factor and momentum thickness development for a wide range of roughness geometries. Dvorak's rough surface law is given in Eq. (2.1)

$$\frac{U}{U_\tau} = \left(\frac{1}{K}\right) \ln \left| \frac{yU_\tau}{\nu} \right| + A - \frac{\Delta U}{U_\tau} \left( \frac{kU_\tau}{\nu}, \lambda \right) \quad (2.1)$$

where  $K$  and  $A$  are the smooth wall constants,  $k$  is the relative roughness height,  $y$  is the height measured above the mean elevation of the roughness,  $\lambda$  is the roughness density,  $U$  is the local velocity outside of the boundary layer, and  $U_\tau$  is the friction velocity. The new skin-friction law described by Dvorak along with the momentum integral equation provided a prediction method of the development of turbulent boundary layers over rough surfaces in varying pressure gradients.

The turbulent boundary layer correlations presented by Dvorak [12] and Betterman [13] were furthered by Simpson [14] shortly after the data was published. Simpson explained that the skin-friction law and roughness density correlations used in previous work were strictly for small roughness heights in relation to boundary layer thickness. Further, the correlation only applied to the vicinity immediately away from the wall in the region of constant shear stress. Simpson investigated similar roughness

geometries as those in previous studies with larger roughness intensities. In the presence of a pressure gradient, Simpson explained that the stress exerted on the wall is partly due to the form drag produced by the pressure distribution on the roughness elements [14]. From his experiments, Simpson was able to prove his hypothesis and provide a more generalized parameter for roughness density.

Around the time of the investigations of Simpson and Dvorak, Dirling [15] was investigating surface roughness heat transfer rates on reentry nose tips. Dirling provided an effective sand-grain roughness correlation for arbitrary rough surfaces with experimental data considering both shape and spacing of roughness elements. Dirling's findings were important as they unified the data and correlations of two-dimensional and three-dimensional roughness investigations. A plot of Dirling's experimental data that led to his correlation between equivalent sand-grain roughness and roughness density is given in Figure 2.1.

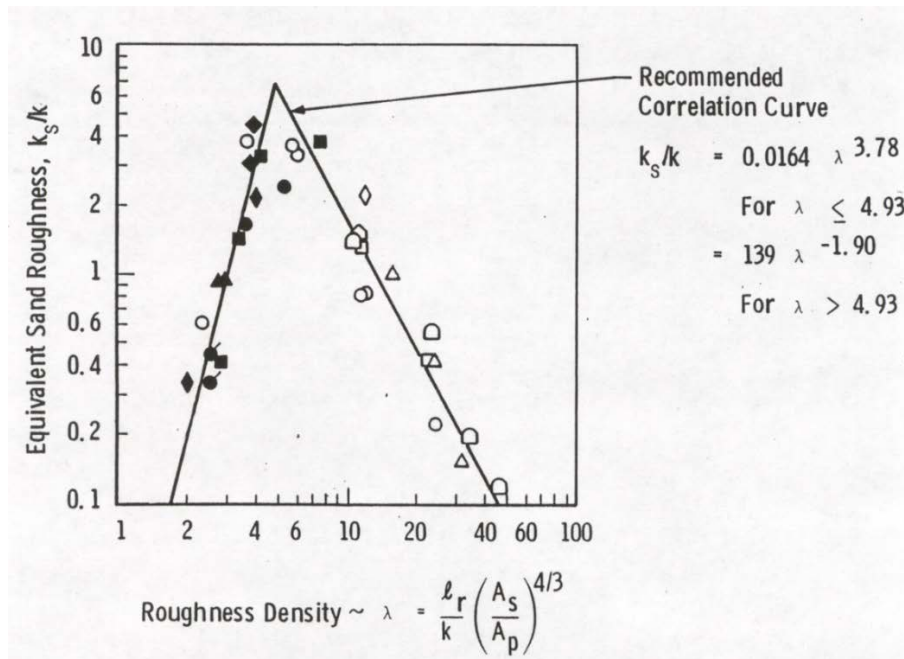


Figure 2.1: Effective sand-grain roughness correlation of Dirling[15]

As the experimental database for surface roughness grew, Coleman et al. [16] questioned several of the assumptions made by Schlichting [2] in early experiments. The re-evaluation of Schlichting's original data led to finding the original skin friction coefficients were higher than the corrected values by amounts ranging from 0.5 to 73 percent. The equivalent sand roughness values presented by Schlichting were also studied and found to be higher than the corrected values by amounts ranging from 26 to 555 percent. Coleman et al. presented a new correlation for skin-friction and also corrected values for equivalent sand roughness for a wide range of geometric shapes. Upon the correction of these parameters, Sigal and Danberg [17] presented a new correlation for the density parameter that Simpson had previously proposed. The new density parameter was effective in calculating the displacement of the logarithmic-wall profile for two-dimensional and three-dimensional roughness allowing for a better understanding of the turbulent boundary layer over a wider range of roughness densities. The Sigal-Danberg roughness density parameter is given by Eq. (2.2) where  $S/S_f$  is the unity shape factor,  $A_f$  is the element frontal area, and  $A_S$  is the windward wetted surface area.

$$\Delta_S = \frac{S}{S_f} \left( \frac{A_f}{A_S} \right)^{-1.6} \quad (2.2)$$

Along with the equivalent sand-grain roughness method, Schlichting [2] proposed the discrete element method (DEM), in which the addition of the skin friction drag on the flat plate and the form drag on individual roughness elements are used to find the total drag on a rough surface. While the equivalent sand-grain roughness model is still used to find skin-friction values on realistic rough surfaces, it does not accurately predict heat transfer enhancement. The DEM has proven effective in characterizing the heat transfer

from rough surfaces and is therefore commonly used in experimental studies of roughness.

Bons [18] showed that the Sigal-Danberg roughness density parameter was difficult to define using roughness elements with random spacing, shape, and size. Therefore, McClain et al. [19] adapted the DEM to allow for prediction of skin friction and heat transfer for flows over randomly rough surfaces. The model evaluates the effects of roughness by considering the physical characteristics of roughness elements in the solution of the boundary-layer equations. McClain et al. [20] used the mean elevation of randomly rough surfaces as the computational location of the no-slip surface which proved to agree well with experimental skin friction measurements. Another advancement in the DEM was made by McClain et al. [21] with the Extended Surface – Discrete Element Method (ES-DEM). In randomly rough surfaces, the ES-DEM treats individual roughness elements as extended surfaces such as fins. The use of this model allows for better characterization of heat transfer by incorporating temperature changes that occur along the height of individual roughness elements.

Computational simulations have also been used to better understand flow over rough surfaces. However, this method requires a vast number of grid points in order to capture and resolve complex roughness geometries. Grid-resolved simulations performed by Bons et al. [22] showed superior agreement with experimental data compared to the DEM but require significantly more computational time.

### *Surface Analysis*

As mentioned in the previous chapter, an autocorrelation analysis was used for pattern recognition in the analysis of real ice surface statistics. The autocorrelation

function used in this study analyzed a large number of parameters from the real ice surface studied by Hawkins including height parameters, spatial parameters, hybrid parameters (involving both height and directional analysis), and individual feature parameters [23]. The following section gives a detailed account of the important parameters used to analyze the real ice surface and create the analog surfaces for this investigation.

### *Height Parameters*

To analyze height parameters, a reference surface is defined at a height of 0 and the displacement from the reference surface to the roughness height is evaluated. From the displacement values the following height parameters are calculated: root-mean-square (RMS) height, skewness, maximum peak height, maximum pit height, maximum height, and the arithmetical mean height.

The RMS height corresponds to the standard deviation of distance from the mean roughness height. It is better understood as the equivalent to the standard deviation of all roughness element heights. It is defined in Eq. (2.3) where A is the definition area of the autocorrelation, Z is the height, and x and y are the ordinate values.

$$R_q = \sqrt{\frac{1}{A} \iint Z^2(x, y) dx dy} \quad (2.3)$$

The skewness represents the symmetry of the distribution. It is defined as the degree of bias, or asperity, of the individual roughness shapes. Eq. (2.4) shows the calculation for skewness. For a Gaussian distribution, the skewness is zero.

$$Ssk = \frac{1}{R_q} \left[ \frac{1}{A} \iint Z^3(x, y) dx dy \right] \quad (2.4)$$

Maximum peak height and maximum pit height are simply defined by name. The maximum height parameter is defined as the sum of the maximum peak height and maximum pit height, basically the largest difference in height over the roughness surface being analyzed. The arithmetical mean height is the mean of the absolute value of the height of the roughness surface ordinate points.

### *Spatial Parameters*

The spatial parameters calculated in the autocorrelation function focus on the direction of the plane (wavelength direction) in which the roughness is being analyzed. These parameters are the predominant indicators of many surface features such as the periodicity of the roughness, or the length scale from ridge to ridge in which shed vortices interact with the next downstream elements. The spatial parameters include the autocorrelation length, texture aspect ratio, and texture direction. The autocorrelation length is defined as the horizontal distance of the region that the autocorrelation function analyzes. The texture aspect ratio is a measure of the uniformity of the surface texture and the texture direction represents the lay of the surface texture. The combination of the spatial parameters aids in identifying surface features and provides a better understanding of the surface statistics.

### *Hybrid Parameters*

The hybrid parameters used in analysis focus on both the height direction and the plane direction. The root mean square gradient is calculated as the root mean square of slopes at all points. The developed interfacial area ratio is defined as the percentage of the definition area's additional surface area contributed by the texture as compared to the

planar definition area. Hybrid parameters are important in the study of surface roughness as they are used to capture additional surface features that may not be captured by strictly analyzing the height and planar directions.

### *Individual Feature Parameters*

Individual feature parameters are implemented in the analysis of the real ice roughness surface so that all aspects of the surface are included in analysis.

Encompassing these parameters in the autocorrelation provides a full understanding of the surface and allows for the partitioning of regions with similar roughness heights. This aids in the simplification of representing a complex rough surface with geometric shapes and proved helpful in the surface generation process of this study. Feature parameters include peaks, hills, course lines, pits, dales, ridge lines, saddle points, local peak heights, and local pit heights.

Through the use of these feature parameters a watershed algorithm can be employed to partition regions. The watershed algorithm is a computational tool in which “water” is poured over a rough surface. As the water runs along the shape of the surface it captures the individual feature parameters and settles in the pits of the surface. Areas in which the water in different pits make contact with each other form ridge lines that are used to partition the surface into regions. By inverting the process, the same can be done for peaks and hill to further identify regions of the surface.

All of the parameters defined in this section are then taken and implemented in a surface creation program used to generate the analog surfaces containing either elliptical cones or half-ellipsoids.

### *Predictive Method Using Surface Statistics*

In 2010, Flack and Schultz [24] provided a predictive method for the equivalent sand-grain roughness height that relied solely on the measurement of surface statistics. After reviewing previous data of flows in the fully rough regime, they built upon the correlations of prior researchers by using the equivalent sand-grain roughness height as the roughness scale. Their study incorporated a variety of three-dimensional rough surfaces to investigate the relationship between physical roughness surface statistics and the equivalent sand-grain roughness height. The results of the investigation showed that the most effective surface parameters in describing a rough surface are the root-mean-square roughness height and the skewness of the surface elevation. Using these parameters, Flack and Schultz provided a correlation to predict the equivalent sand-grain roughness height given in Eq. (2.5).

$$k_s = 4.43R_q(1 + Ssk)^{1.37} \quad (2.5)$$

The prediction of the equivalent sand-grain roughness height also allowed for the prediction of the frictional drag coefficient using a new correlation presented by Flack and Schultz [24]. Through the use of boundary layer similarity scaling, the correlation determines the overall frictional drag coefficient as a function of the ratio of the equivalent sand-grain roughness height to the length of the rough surface. The relationship for the frictional drag coefficient is given by Flack and Schultz as Eq. (2.6).

$$\sqrt{\frac{2}{C_f}} = -2.186 \ln\left(\frac{k_s}{L}\right) + 0.495 \quad (2.6)$$

*Viscous Boundary Layers*

Viscous boundary layers, also referred to as velocity boundary layers, were first discovered by Prandtl in 1904. This discovery is widely considered as the biggest breakthrough for practical fluids engineering as it applies to nearly every flow field studied in fluid mechanics [25]. Prandtl found that any flow near a solid surface has a relatively thin layer near the surface in which shear stresses are non-negligible and viscous forces dominate [26]. This region is known as the viscous boundary layer. Outside of the viscous boundary layer, flow is considered inviscid and irrotational. Figure 2.2 shows the development of a boundary layer near a solid wall.

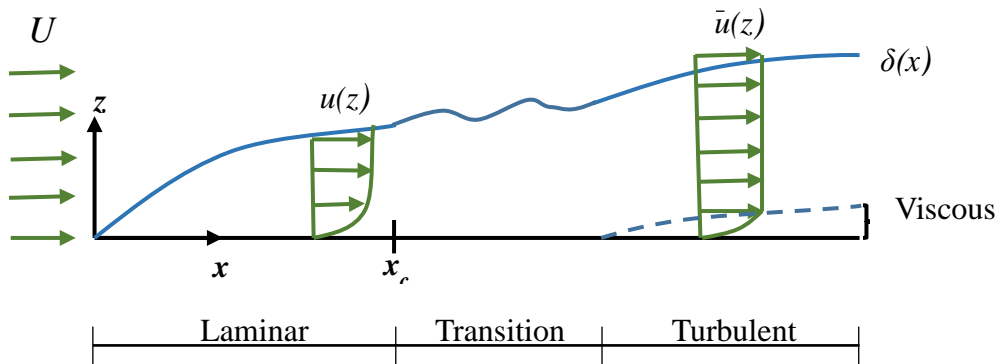


Figure 2.2: Viscous boundary layer development on a flat plate (not to scale)

The inviscid freestream velocity field ( $U_\infty$ ) flows over the flat plate as the boundary layer begins to form in the laminar region. The velocity boundary layer thickness ( $\delta$ ) is a function of the distance along the plate ( $x$ ) and is measured as the vertical distance from the plate until the velocity field reaches the freestream velocity. Flow in the laminar regime is uniform as fluid particles follow stream lines. Once the

flow reaches the critical point ( $x_{cr}$ ), it begins to transition into the turbulent regime in which the fluid particles behave chaotically. Due to the high amount of shear stress produced by the velocity gradient, the fluid begins to swirl in eddy like motions causing disruption in the flow field. However, a viscous sublayer begins to form near the wall in which the flow remains uniform while the flow outside of the sublayer is chaotic. The uniformity in the viscous sublayer is a result of reduced eddy interactions near the wall because of the small length scale. While the flow in the turbulent region is chaotic, time-averaged instantaneous velocity profiles appear nearly uniform and geometrically similar to the velocity profile in the laminar region.

The no-slip condition assumes that the fluid “sticks” to the wall at the boundary and thus the velocity at the wall is zero. As a result of fluid motion and the fluid sticking to the boundary, a wall shear stress ( $\tau_w$ ) develops. Eq. (2.7) describes the calculation of wall shear stress for a Newtonian fluid as the dynamic viscosity of the fluid multiplied by the velocity gradient at the wall.

$$\tau_w = \mu \left. \frac{\partial u}{\partial z} \right|_{z=0} \quad (2.7)$$

Wall shear stress can be non-dimensionalized in the form of the skin friction coefficient ( $c_f$ ) shown in Eq. (2.8) where  $\rho$  is the fluid density and  $U_\infty$  is the freestream velocity.

$$c_f = \frac{\tau_w}{1/2 \rho U_\infty^2} \quad (2.8)$$

As mentioned previously in the surface roughness section, the skin friction coefficient is important to characterize drag on various surfaces under similar flow conditions.

Reynolds number is another important non-dimensional parameter used to relate cases of flow over roughened surfaces. Flows with similar Reynolds numbers are

predicted to behave similarly making it a common comparison parameter for a number of fluids related experiments. From scale analysis, the Reynolds number can be better understood as a geometric slenderness ratio that describes the boundary layer thickness in relation to the flow domain length. Eq. (2.9) gives the local Reynolds number for flow over a flat plate

$$\text{Re}_x = \frac{\rho U_\infty x}{\mu} \quad (2.9)$$

where  $\rho$  is the fluid density,  $U_\infty$  is the freestream velocity,  $x$  is the location on the plate from the leading edge, and  $\mu$  is viscosity. Flows with Reynolds numbers larger than  $5 \times 10^5$  are considered turbulent and anything below that is considered laminar [27].

### *Thermal Boundary Layers*

For many flows over rough surfaces there commonly exists a temperature difference between the fluid and the surface with which it is interacting. This temperature difference will cause a thermal boundary layer to grow that is similar to the velocity boundary layer. Figure 2.3 shows the growth of a thermal boundary layer on a flat plate in which the temperature of the plate ( $T_s$ ) is higher than the freestream fluid temperature ( $T_\infty$ ). As the fluid flows over the plate, a temperature gradient begins to form within the fluid creating the thermal profile ( $T$ ) as a function of the vertical distance from the plate ( $z$ ). The thermal boundary layer height ( $\delta_T$ ) is defined as the vertical distance from the plate to the height where the fluid is equal to the freestream temperature. The thermal boundary layer height is a function of the streamwise distance along the plate ( $x$ ) as it grows while moving along the plate.

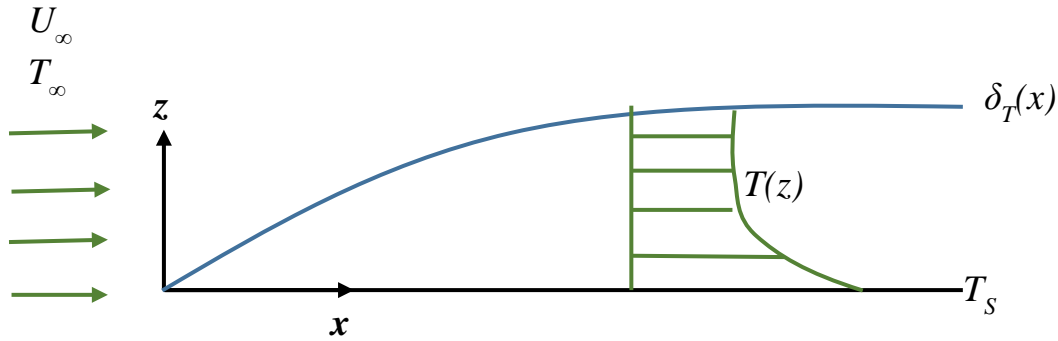


Figure 2.3: Thermal boundary layer on a flat plate (not to scale)

A non-dimensional parameter known as the Prandtl number relates the viscous boundary layer to the thermal boundary layer. The quantity of the Prandtl number is a direct comparison of the viscous boundary layer thickness to that of the thermal boundary layer, and represents the ratio of momentum diffusivity to thermal diffusivity in a fluid.

Eq. (2.10) shows the Prandtl number calculation

$$Pr = \frac{c_p \mu}{k_f} = \frac{\nu}{\alpha} \quad (2.10)$$

where  $c_p$  is the specific heat of the fluid,  $k_f$  is the thermal conductivity of the fluid,  $\nu$  is the kinematic viscosity of the fluid, and  $\alpha$  is the thermal diffusivity of the fluid. A fluid with a Prandtl number much less than one ( $Pr \ll 1$ ) means the thermal boundary thickness is much larger compared to the viscous boundary layer thickness. For Prandtl numbers much greater than one ( $Pr \gg 1$ ), the viscous boundary layer thickness is much larger than that of the thermal boundary layer. [28].

Comparable to the wall shear stress incurred due to viscous forces in a velocity boundary layer, the temperature gradient in a thermal boundary layer causes a heat flux between a surface and the moving fluid. The surface heat flux is shown in Eq. (2.11)

$$q_w'' = -k_f \left. \frac{\partial T}{\partial z} \right|_{z=0} \quad (2.11)$$

where the flux is equivalent to the thermal conductivity of the fluid multiplied by the temperature gradient at the surface.

To compare multiple experiments implementing various fluids and flow conditions, the surface heat flux is non-dimensionally represented by the local Stanton number shown in Eq. (2.12)

$$St_x = \frac{q_w''}{\rho U_\infty c_p (T_s - T_\infty)} = \frac{h}{\rho U_\infty c_p} \quad (2.12)$$

where  $h$  is the convective heat transfer coefficient at a given location  $x$ . The Stanton number is defined as the ratio of convective heat transfer to the thermal capacity of a fluid. Theoretical Stanton number correlations were used in this investigation for data comparison. For cases with negligible acceleration, Eqs. (2.13) and (2.14) were used and Eqs. (2.15) and (2.16) were used in the accelerated cases. For a full description of the correlations and their derivations, see Shannon [7].

$$St_{x,\text{laminar, no xcel}} = \left[ 1 - (\xi/x)^{3/4} \right]^{-1/3} 0.453 Re_x^{-1/2} Pr^{-2/3} \quad (2.13)$$

$$St_{x,\text{turbulent, no xcel}} = \left[ 1 - (\xi/x)^{9/10} \right]^{-1/9} 0.0308 Re_x^{-1/5} Pr^{-2/3} \quad (2.14)$$

$$St_{x,\text{laminar, xcel}} = \left[ 1 - (\xi/x)^{3/4} \right]^{-1/3} \frac{0.453 Re_x^{-1/2} Pr^{-2/3}}{\left[ \int_0^\zeta \left( \frac{U_e(\zeta)}{U_e(x)} \right)^{(2.95 Pr^{0.07})-1} \frac{d\zeta}{x} \right]^{1/2}} \quad (2.15)$$

$$St_{x,\text{turbulent, xcel}} = \left[ 1 - (\xi/x)^{9/10} \right]^{-1/9} \frac{0.0308 Re_x^{-1/5} Pr^{-2/3}}{\left[ \int_0^\zeta \left( \frac{U_e(\zeta)}{U_e(x)} \right) \frac{d\zeta}{x} \right]^{1/5}} \quad (2.16)$$

## Airfoils

Although this study is applicable to surface roughness in a vast area of engineering applications, its direct focus is ice roughness on airfoils. Airfoils are predominantly intended to accelerate fluid flow over the top surface causing a decrease in pressure, in correspondence with Bernoulli's equation, and thus creating lift. This decrease in pressure in the direction of the flow is known as a favorable pressure gradient. As Figure 2.4 shows, the flow will reach a minimum pressure and begin to increase again, known as an adverse pressure gradient.

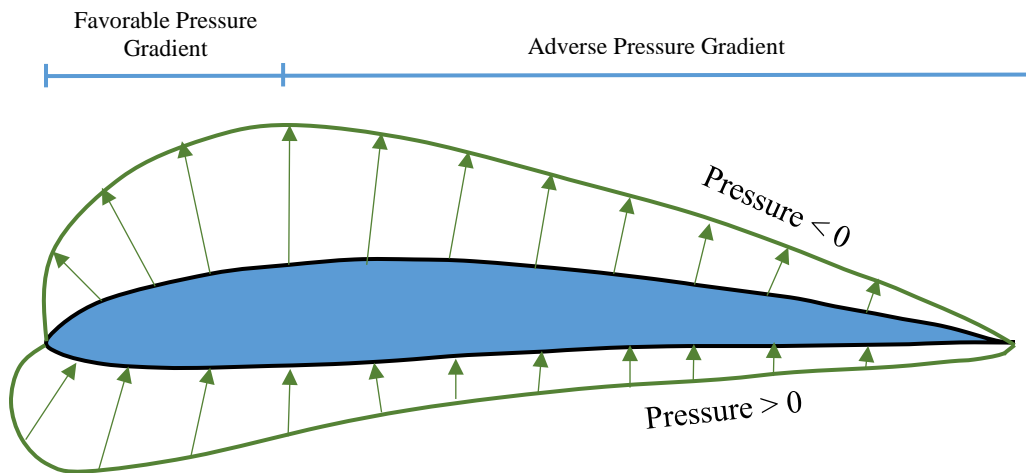


Figure 2.4: Surface pressure distribution on an airfoil

If an adverse pressure gradient exists, it is possible for the flow to detach from the airfoil. Once the boundary layer separates, a wake region forms in which flow reverses causing a significant increase in pressure drag. This separation occurs when the velocity gradient at the surface of the airfoil reaches zero as shown in Figure 2.5.

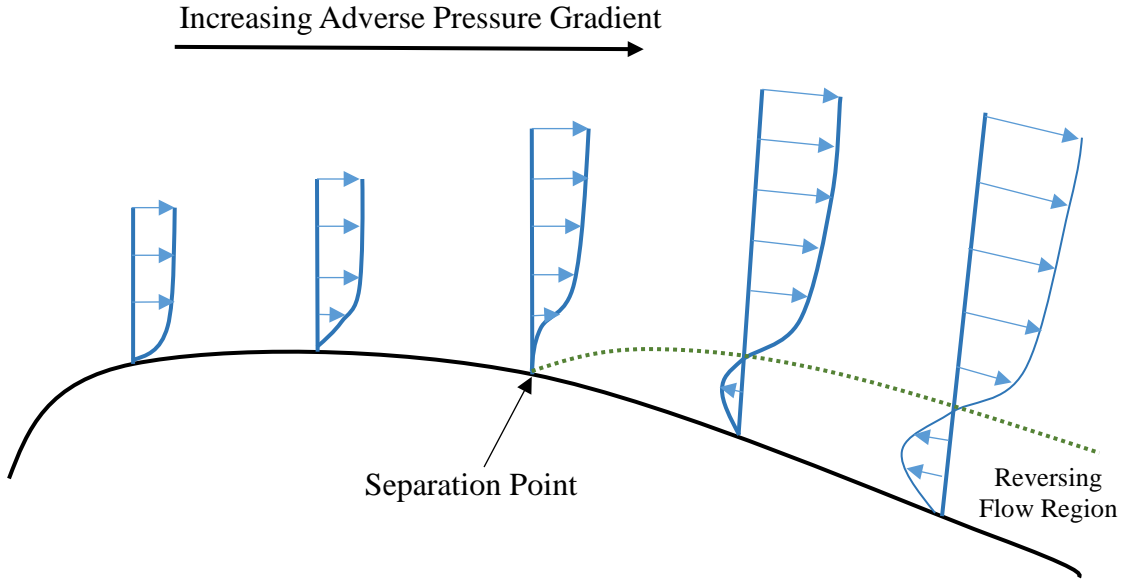


Figure 2.5: Boundary layer separation on an airfoil (not to scale)

The pressure distribution in a flow field is important to understanding the flow characteristics around any immersed body. The non-dimensional pressure coefficient given by Eq. (2.17) is a common way to represent the local pressure distribution as it is useful for scale modeling because of its independence from Reynolds number.

$$C_p = \frac{P - P_\infty}{1/2 \rho U_\infty^2} \quad (2.17)$$

In Eq. (2.17), the freestream pressure is  $p_\infty$  and the local pressure is  $p$ . A local velocity distribution may be found by applying Bernoulli's equation to Eq. (2.17), as given in Eq. (2.18).

$$U_e = U_\infty (1 - C_p)^{1/2} \quad (2.18)$$

The pressure and velocity distribution equations above were used to create a ceiling insert that matches the flow induced around a NACA 0012 airfoil. Therefore, the tests performed in this study implemented a flat plate yet still match the pressure and

velocity distributions found on the curved airfoil surface. This is significant as it allows for simpler wiring and infrared imaging for convective heat transfer testing. Additionally, flat plate data is abundant for heat transfer and boundary layer experiments allowing for validation and data comparison.

## *Aircraft Icing*

### *Icing Terms*

When flying through hazardous conditions, aircraft surfaces commonly take on impinging water droplets and ice particles. As layers of water continually freeze to the frame of an aircraft, a gradual buildup of ice forms known as an ice accretion. Two main parameters used by the Federal Aviation Administration (FAA) to describe cloud conditions that lead to ice accretions are the liquid water content (LWC) in a cloud and the median volumetric diameter (MVD) of water droplets. The LWC is defined as the mass of liquid water per unit volume of air in cloud. The MVD is defined as the diameter of a water droplet in a cloud where half of the droplets have a larger diameter and the other half have a smaller diameter. The LWC is related to the rate at which ice accretes on aircraft surfaces and the MVD is associated with the amount of ice accreted [29].

To be certified for flight in icing conditions, aircraft must meet specifications set by the FAA and deemed safe to operate. The atmospheric icing conditions set by the FAA are comprised of LWC and MVD, along with altitude, temperature, and extent of clouds [30]. Two types of conditions exist: Appendix C conditions and Appendix O conditions. Appendix C conditions refer to supercooled droplets in a cloud that have an MVD of 1-50  $\mu\text{m}$ . Appendix O conditions contain supercooled large droplets (SLD) with

an MVD  $> 50 \mu\text{m}$ . Historically, Appendix C conditions have been used for aircraft certification, but as of 2014, Appendix O conditions have become an important focus of ice protection and removal systems [31].

In relation to the atmospheric conditions in which an aircraft is flying, ice accretions form in two regimes: glaze ice and rime ice. Glaze ice, commonly referred to as clear ice, is a dense layer of hard, glossy ice that forms near the freezing temperature of water ( $32^\circ\text{F}$ ). In the glaze ice regime, only a portion of supercooled water droplets freeze upon impact, while the rest of the droplets impinge and run aft until freezing downstream of the stagnation point. The rime ice regime is characterized by temperatures well below the freezing point of water (near  $0^\circ\text{F}$ ) causing all impinging droplets to freeze upon impact. Because of this, small pockets of air are trapped between the freezing droplets causing irregular, roughened ice shapes that appear opaque and brittle. Mixed ice, a combination of both glaze and rime ice, can form if the size of water droplets vary drastically within a cloud. This is typically a hard and rough ice shape [32].

#### *Ice Accretion Process*

In 1986, Olsen and Walker [33] used a high speed camera in the Icing Research Tunnel (IRT) at NASA Glenn Research Center to film and photograph the process of ice accreting on an airfoil. A symmetric airfoil was mounted at a zero degree angle of attack and a series of tests were run at speeds ranging from 50 to 320 km/hr and temperatures ranging from above freezing to  $-25^\circ\text{C}$ . They observed that impinging supercooled water droplets began to merge and grow into a thin film. Once the aerodynamic drag on the thin film becomes greater than the surface tension on the airfoil that keeps the drops stationary, the thin film will begin to move downstream along the airfoil surface. The

film continues to move aft until it freezes to the surface of the airfoil and becomes a layer of ice roughness. As supercooled droplets continue to impinge and are pulled downstream, an ice plateau forms on the stagnation region in which there is a thick layer of ice with minimal roughness. The largest roughness forms downstream of the stagnation point in a region of enhanced convection where impinging droplets freeze to protruding ice shapes. Figure 2.6 depicts the distinct regions thought to be present in an ice shape on a symmetric airfoil at zero angle of attack.

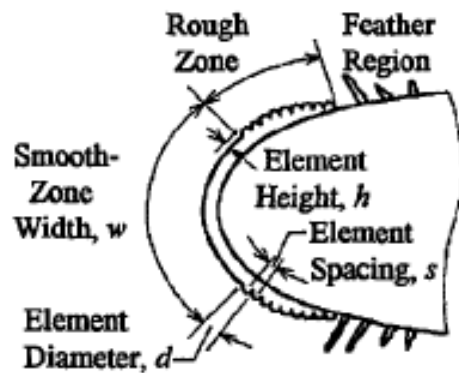


Figure 2.6: Early stage ice accretion on airfoil leading edge [34]

### *Ice Accretion Modeling*

In 1953, the initial model for airfoil icing was formed by Messinger [35]. Messinger's model was designed to analyze conditions governing the equilibrium temperature of an insulated, unheated surface exposed to icing through the use of a one-dimensional equilibrium energy balance. The one-dimensional energy balance considers energy input in the form of kinetic energy from droplet impingement, viscous heat from friction in the boundary layer, and latent heat from fusion. Energy losses are taken into account in the form of convection away from the surface, evaporation or sublimation, and

the heat lost through absorption from the impinging droplets. The significant forms of heat transfer considered by Messinger are shown in Figure 2.7.

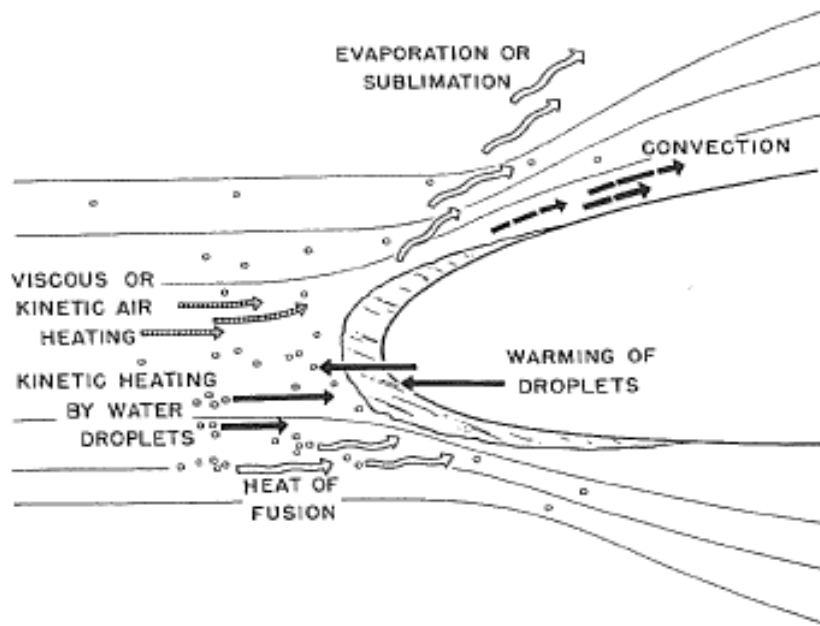


Figure 2.7: Modes of energy transfer for an unheated airfoil in icing conditions [35]

During his investigation of the unheated airfoil, Messinger [35] reported that some of the impinging droplets did not freeze on impact. Because of this observation, Messinger developed a non-dimensional parameter known as the freezing fraction. The freezing fraction is defined as the ratio of the number of droplets that freeze on impingement to the total number of supercooled impinging droplets. Therefore, a freezing fraction of one corresponds to every impinging droplet freezing on impact causing the formation of rime ice. If the freezing fraction is less than one, water runback is present on the airfoil surface leading to a region of glaze ice beginning at the stagnation point.

The Messinger model was foundational to the understanding of ice accretions on aircraft surfaces and although modified, is still used today. LEWICE, the ice prediction code developed by NASA, implements the use of the equivalent sand-grain roughness model developed by Schlichting and Nikuradse based on the freezing fraction defined by Messinger. Ice roughness heights are estimated using Eq. (2.19)

$$x_k = \frac{1}{2} \sqrt{0.15 + \frac{0.3}{N_{f,stag}}} \quad (2.19)$$

where  $N_{f,stag}$  is the freezing fraction at the stagnation point and is calculated separately.

LEWICE incorporates effective equations and models in an attempt to predict ice shapes but there remains opportunities for improvement. For example, predicting the ice roughness heights based on one parameter,  $N_{f,stag}$ , for various icing conditions is ineffective as realistic ice roughness differs in size and distribution density [36]. Shin [37] demonstrated this by comparing the roughness heights of real ice accretions created in the IRT to the sand-grain roughness heights predicted by LEWICE. Shin's investigation implemented varying icing conditions, and he concluded that LEWICE poorly predicted ice roughness trends. The comparison of the predicted sand-grain roughness heights and the measured roughness heights at set values of LWC is shown in Figure 2.8.

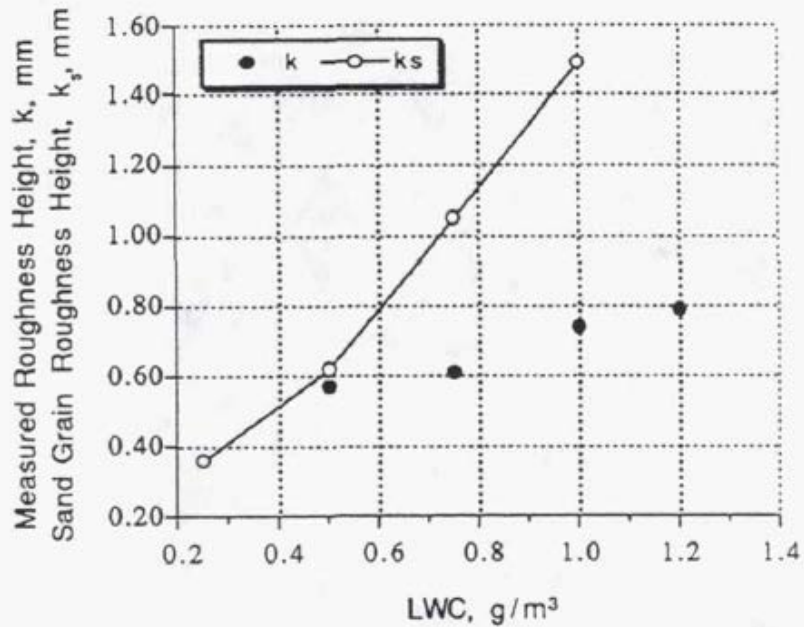


Figure 2.8: Comparison of measured roughness height with the predicted sand-grain roughness height [37]

#### *Recent Ice Roughness Investigations*

With a desire to remove empirical correlations from ice accretion prediction, Croce et al. [38] developed a Lagrangian droplet simulation technique to create ice shapes. The model was formed by investigating the behavior of individual water droplets upon impact with an airfoil. Croce's simulator accounted for additional stochastic processes of ice accretions, such as bead coalescence, nucleation, and growth, not captured by current ice prediction codes.

Tecson and McClain [39] created a similar simulation program that modeled droplet impingement on a flat surface to form realistic ice roughness. The output of the simulator is a random distribution of roughness in which bead diameter, location, and spacing varies without bead overlap. Hemispherical solid models of the simulator outputs were created to determine convective heat transfer with a constant flux boundary

condition in flows with negligible acceleration. The same surfaces were used in an investigation done by Walker et al. [40] with varying heat flux boundary conditions to assess convective heat transfer enhancement. Walker et al. found that varying the thermal boundary conditions on the solid models had minor effect on the enhancement of the convective heat transfer.

Shannon and McClain [41] developed two more random ice accretion surfaces using the Lagrangian droplet simulator. The first surface exhibited a smooth-to-rough transition from the leading edge to the roughness elements as is found in many historical studies of roughness. The second surface exhibited a variation in roughness height with parameters based on the 113012.04 test in the Icing Research Tunnel at NASA Glenn Research Center (designated the 113012.04\_IRT surface). Based on the formation of real ice accretions with fluid runback, the second surface exhibited a gradual transition region from the leading edge to the roughness. The two surfaces were then investigated for convective heat transfer in flows with negligible acceleration and flows with acceleration matching that of a NACA 0012 airfoil. With negligible acceleration, the difference in the transition region had little to no effect on the convective heat transfer. In the accelerated flow cases, the surface based on the real ice accretion had lower convective heat transfer values. Shannon and McClain [41] believed this to be the case because of lower turbulence intensity on the second surface from the more gradual transition region.

#### *Real Ice Roughness Surface*

Hawkins [8] used the 113012.04 laser scan performed by McClain et al. [42] to create a replica of the actual ice roughness surface from the laser scan. For a full account of the method used to create the 113012.04 real ice surface refer to Hawkins [8]. The

following is a brief description of the method based on the work of Hawkins and McClain because of its importance for the purposes of this investigation.

### *Laser Scanning*

The Icing Research Tunnel at the NASA Glenn Research Center was used to form an ice accretion on a 21” chord NACA 0012 airfoil at 0° angle of attack. The airfoil spanned the entirety of the 72” wind tunnel test section and the ice accretion parameter of the 113012.04 case was 0.195. Once thermal equilibrium was reached, the wind tunnel test velocity was reduced to approximately 5 m/s while maintaining a static temperature of about -4 °C to prevent the ice accretion from liquefying. The iced airfoil was then painted with titanium dioxide paint and the leading 120-150 mm of both sides of the leading edge of the airfoil were laser scanned with a Romer Absolute Arm. The laser scan performed at the center-span of the airfoil was approximately 100 cm wide in the spanwise direction. The mapped laser scan is shown in Figure 2.9.

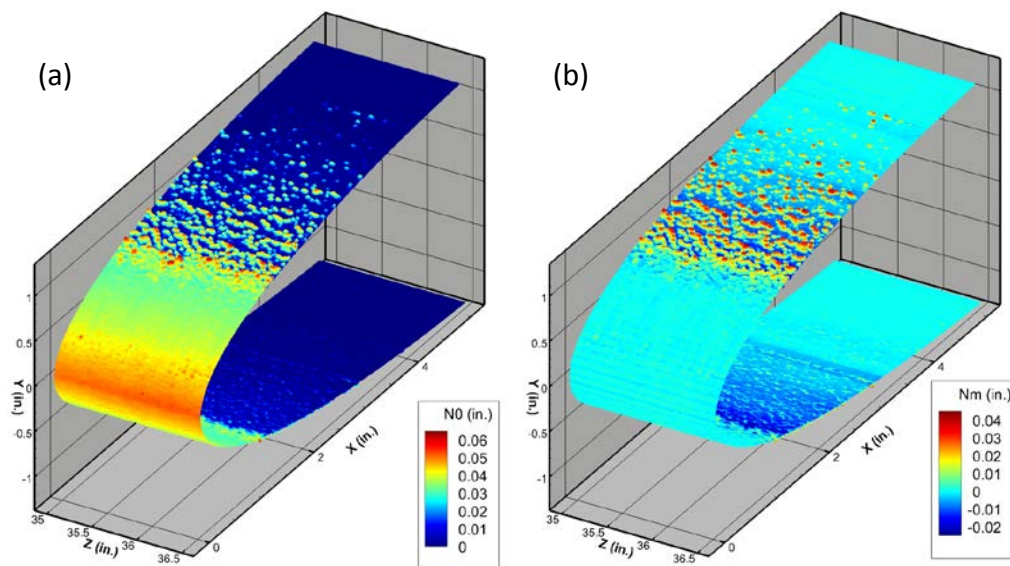


Figure 2.9: Topographies of the 113012.04 Real Ice surface displaying a) ice thickness, and b) ice roughness

The laser scanned ice accretion point cloud was analyzed using the self-organizing map (SOM) method of McClain and Kreeger [43]. The self-organizing map method uses a small set of codebook vectors to represent larger regions of data to capture the trends of large data sets. The codebook vectors representing clumps of data points are then linearly chained together to complete the SOM. The linearly chained codebook vectors represent the mean iced surface, also referred to as the ice manifold. The airfoil surface and mean ice manifold are referenced to an X-Y (chord-chord normal) plane as shown in Figure 2.10.

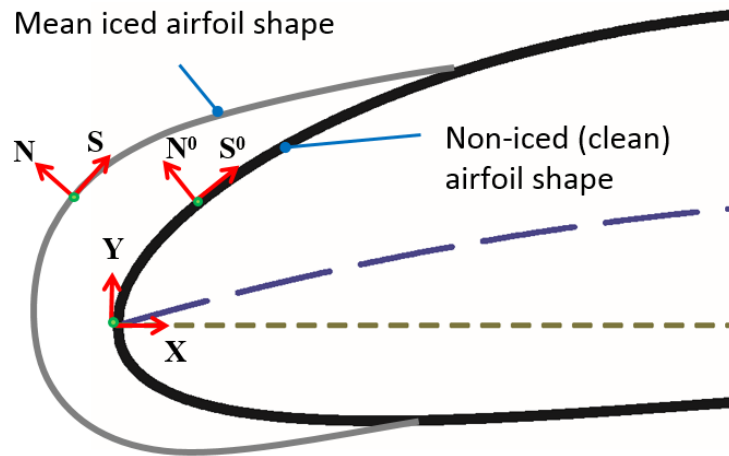


Figure 2.10: Coordinate systems used in the SOM method [44]

N represents the direction normal to the ice manifold and S represents the direction along the mean ice manifold in the flow direction.  $N^0$  and  $S^0$  are directionally similar but represent the directions at the non-iced airfoil surface. These coordinate systems were then used to convert the ice shape created around the curved airfoil into a surface that could be easily manufactured on a flat surface. A discrete arc-length approach implementing the S and N coordinate systems was used to “unwrap” the point cloud of the ice shape. The arc length at one end of the linearly chained codebook vectors

is a known distance away from the stagnation point of the airfoil so the surface distance of each codebook vector can be found as an S-distance along the ice manifold. The statistical height from the mean ice manifold surface in the N direction normal to the surface is described by the RMH value determined at each codebook vector. The point cloud was then converted into surface thicknesses in the  $S^0$ - $N^0$  coordinate system. Figure 2.11 shows the point cloud projection along with the SOM codebook vectors.

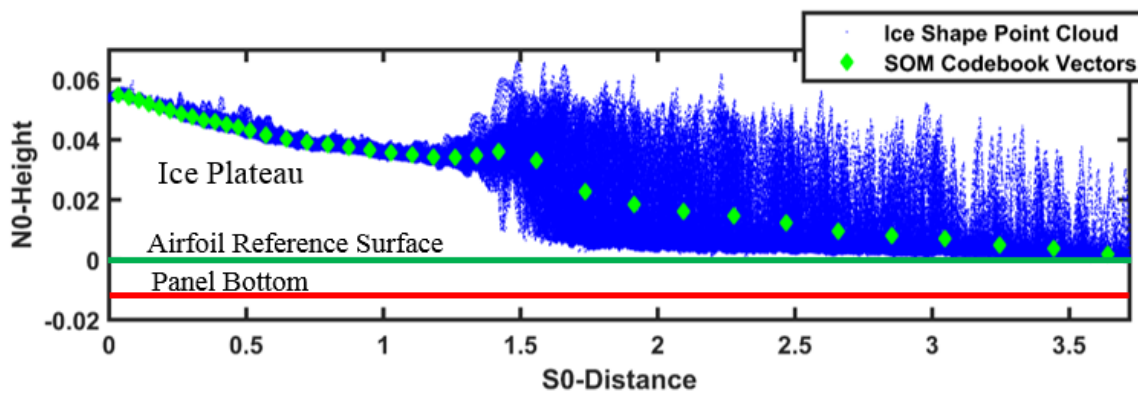


Figure 2.11: Surface thickness distribution of laser scanned ice roughness points [8]

As seen in the figure above, the lowest height of the point cloud data and the lowest codebook vector lie just above the airfoil reference surface. Also, the first ten to fifteen inches of the scaled real ice surface do not have significant roughness which is referred to as the glaze ice plateau. The surface thickness in this region near the leading edge occurs due to a thin film liquid layer freezing just beyond the stagnation point. Since this study focuses on ice roughness rather than ice thickness, the data points were shifted due to negligible roughness in the ice plateau region. The  $S^0$ - $N^0$  points and codebook vectors were leveled with respect to the leading edge by applying a shift into the S-N

coordinate system. This allowed for specification of the ice roughness by eliminating the ice thickness from the mean ice manifold

Although the significant roughness had been identified and leveled, a portion of the roughness fell beneath the panel bottom and the trailing edge roughness was raised above the panel bottom. To retain significant roughness and prepare the point cloud for full surface creation, the points were shifted once more. Figure 2.12 shows the final point cloud used to model the 113012.04 case. The points that fell below the panel bottom were shifted up and the points near the trailing edge were shifted down to sit flush with the panel bottom. Furthermore, the leading 7.5 inches of roughness were removed to match the smooth entry region of previous test panels.

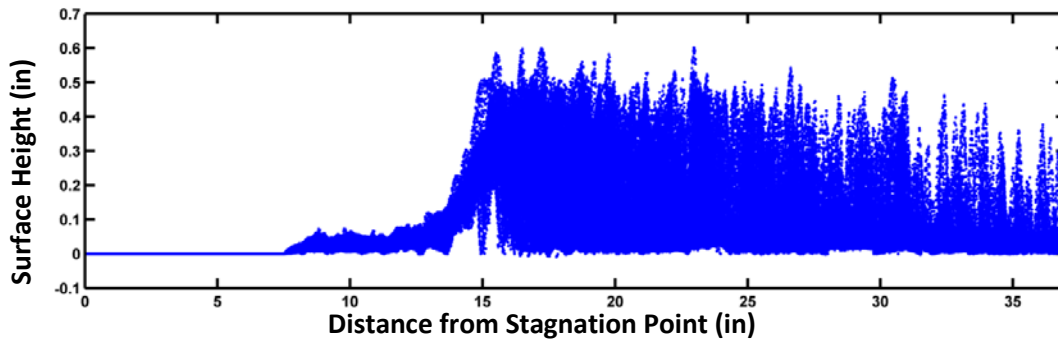


Figure 2.12: Surface height distribution of laser scanned ice roughness points [8]

### *Real Ice Surface Creation*

The unwrapped point cloud was then projected onto a flat surface in three dimensions. In order to create a full surface for manufacturing, a quadratic interpolation code was used to generate a surface function to fit the point cloud data. A region of the 113012.04 surface can be seen in Figure 2.13. These resampled surface files were exported as STL files for use in 3D printing and CNC manufacturing.

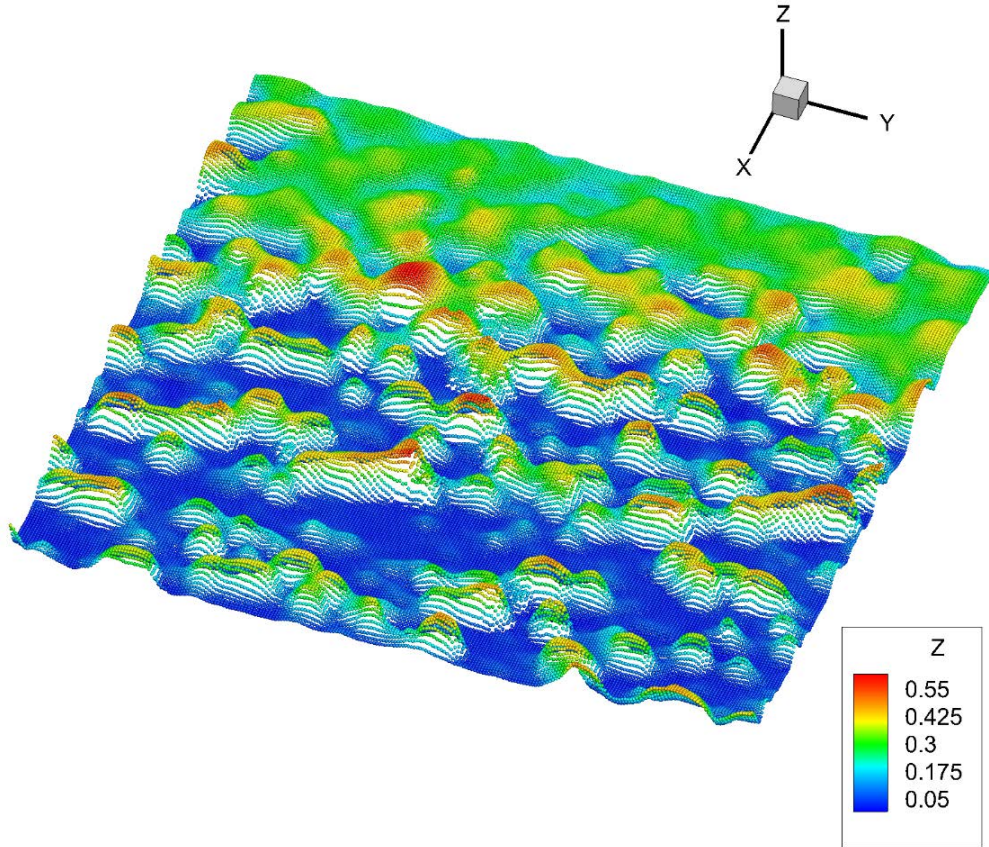


Figure 2.13: Resampled surface height map after quadratic interpolation [8]

After creating the real ice surface, Hawkins investigated the convective heat transfer and boundary layer behavior of the surface. The real ice surface created was expected to behave similarly to that of the realistic simulated surface created by Shannon and McClain [41] when exposed to similar heating and flow conditions. However, the real ice surface created using the SOM method did not behave similarly to the realistic Lagrangian droplet surface created by Shannon and McClain. A comparison of the real ice surface and the Lagrangian droplet surface implementing the streamwise variation of the real ice surface is given in Figure 2.14 and a comparison of results is given by the Stanton numbers plots in Figure 2.15.

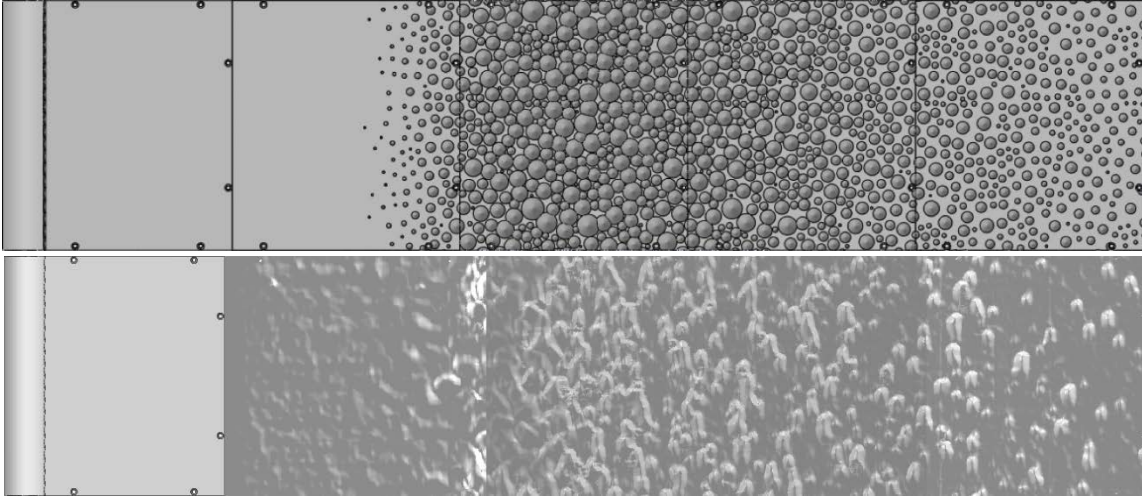


Figure 2.14: Surface panel assemblies of the a) 113012.04\_IRT, and b) 113012.04\_RealIce [41]

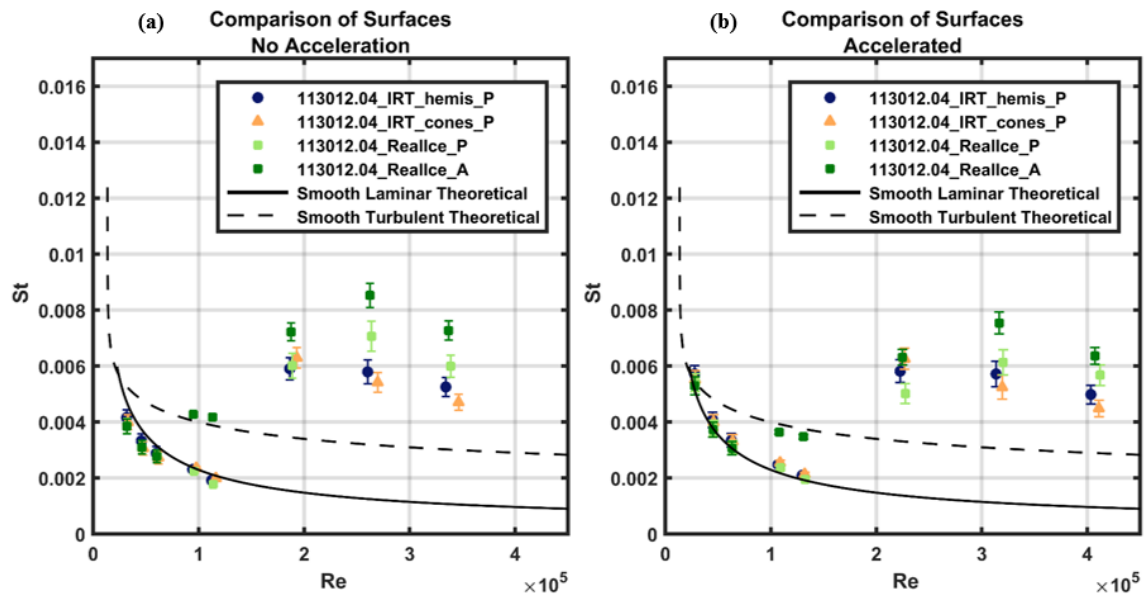


Figure 2.15: Local Stanton number measurements presented for surface comparison in a) flow with negligible acceleration, and b) accelerated flow (flow is from left to right). Note that both the 113012.04\_IRT hemisphere and cone data sets were taken from Shannon [7], and are replicated here for comparison alongside the RealIce surface data taken by Hawkins [8]

From the results shown in Figure 2.15, Hawkins concluded that the real ice surface exhibited different convective enhancement trends than the simulated surfaces

based on the sparseness of roughness elements in the real ice surface. Figure 2.14 shows that the IRT surface exhibits closely packed roughness elements throughout the entire surface while the real ice surface has a ridge-like structure with peaks and valleys. The difference in convective enhancement trends is because the simulated surface only matches one length scale of the real ice surface with the global streamwise height variation. The objective of this investigation is to expand on the work of Hawkins by creating a new method that matches multiple length scales of a real ice accretion with multi-scale deterministic features.

## CHAPTER THREE

### Materials and Methodology

To match the global, macroscale, and microscale properties of a real ice laser scanned point cloud, two distributions of roughness elements were digitally created and manufactured for testing. To verify the convective heat transfer performance and boundary layer behavior of the flow over the analog surfaces, a series of experiments were performed. This chapter presents the methodology behind the surface generation process, the design of the apparatuses used for the experiments, instrumentation used for data collection, and the experimental procedures. The data reduction processes used for the convective heat transfer and boundary layer tests are presented. Additionally, the uncertainty associated with the heat transfer coefficients from convection testing is described.

#### *Analog Surfaces*

Two analog surfaces were created to replicate the roughness characteristics of the 113012.04 real ice surface investigated by Hawkins [8]. The goal of the new surface generation process proposed is to match multiple length scales of a real ice surface and recreate repeating roughness patterns using deterministic features. As mentioned previously, the main hypothesis of this study is that the dominant process leading to enhanced convection on ice roughness is vortex shedding from roughness features and the interaction of shed vortices with downstream roughness. Therefore, if the wavelengths present in the streamwise and spanwise directions of a real ice surface are

replicated, the convective heat transfer and flow characteristics of the analog surfaces and the real ice surface will be similar.

The two analog surfaces incorporate elements with elliptical shaped bases in an effort to match the ridge-like structure of the real ice surface. The first surface is comprised of conical elements with elliptical bases and the second is comprised of ellipsoidal elements (hemispherical elements with elliptical bases).

### *Autocorrelation of Real Ice Surface*

The generation of the two surfaces began by running an autocorrelation on the real ice laser scanned point cloud for pattern recognition of the ice shape. The autocorrelation function was used to determine average characteristics of individual roughness elements and to identify the primary streamwise wavelength of the real ice surface (the ridge to ridge length scale). The autocorrelation function is given by Eqs. (3.1) and (3.2).

$$R_{AC}(\Delta x, \Delta z) = \left[ \frac{1}{N_x N_z} |\sum Y'(x + \Delta x, z + \Delta z)| \right]^{0.5} \cdot \text{sign}(\sum Y'(x + \Delta x, z + \Delta z)) \quad (3.1)$$

where

$$Y'(x, z) = Y(x, z) - \bar{Y} \quad (3.2)$$

The autocorrelation function gives the surface root-mean-square roughness height ( $R_{AC}$ ) for  $\Delta x = 0$  and  $\Delta z = 0$ . The sign function multiplier on the right hand side of Eq. (3.1) is used to differentiate the peaks of the roughness surface from the valleys. Without the multiplier, additional peaks appear at the half-wavelength surface locations.

The autocorrelation function evaluated an 8" by 8" area approximately 18" downstream of the leading edge in order to capture the characteristics of the ice accretion

in the peak roughness region. The region of the real ice surface analyzed can be seen in Figure 3.1(a) and the results of the autocorrelation can be seen in Figure 3.1(b). The autocorrelation result can be understood as a central element that represents an average roughness element, ridges that encompass the spanwise connectivity and separation between rib-like features of the real ice surface, and the directional alignment of the ridges.

To replicate flow interactions found on the real ice surface, the autocorrelation results are used to reproduce the surface aspect ratio and length scale features on the analog surfaces. The important characteristics drawn from the autocorrelation results can be seen in Figure 3.2. The primary features from the real ice surface matched on the analog surfaces are: 1) the magnitude of the central peak ( $R_{AC}(0,0)$ ) which represents the root-mean-square roughness height ( $R_q$ ), 2) the streamwise distance from the maximum peak to the secondary ridge, which is the primary streamwise wavelength,  $\lambda$ , and 3) the aspect ratio of the surface microscales, which is used in the analog surfaces as the average roughness element eccentricity in Eq. (3.3).

$$\varepsilon = \frac{a}{b} \tag{3.3}$$

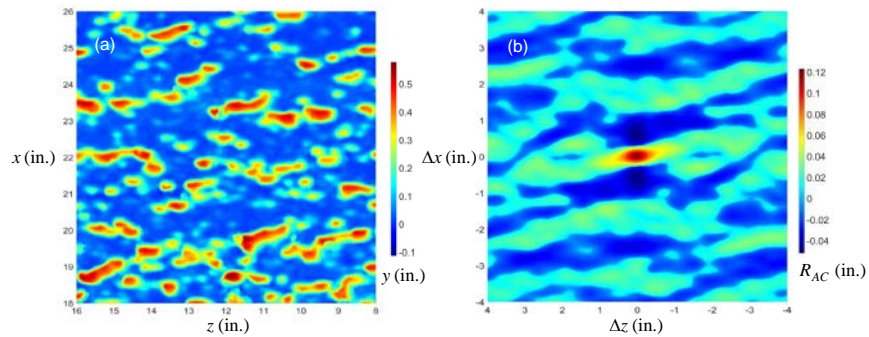


Figure 3.1: a) Region of 113012.04 Surface Analyzed for Surface Characteristics and b) Autocorrelation result

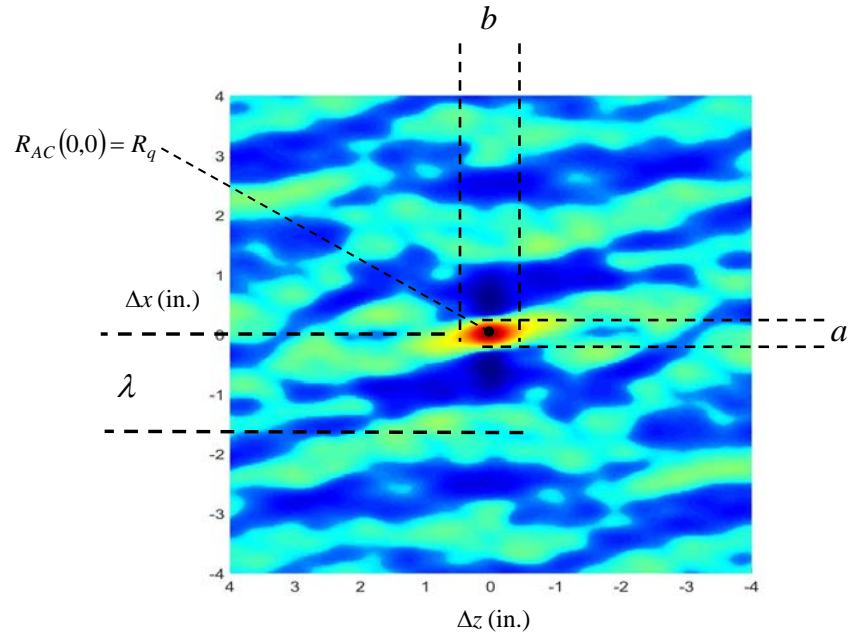


Figure 3.2: Primary autocorrelation features replicated for analog surfaces

From the real ice autocorrelation, the root-mean-square height and ice accretion ridge spacing of the real ice surface were recorded. To find the eccentricity,  $\varepsilon$ , implemented in the elliptical elements, multiple points were extracted from the autocorrelation and parabolized from the maximum value ( $R_{AC}(0,0)$ ) to the axis in the streamwise and spanwise directions to determine the microscale features of the real ice surface. The value where each parabola intersected the surface was recorded and used to calculate the eccentricity used in the creation of the elliptical elements. The eccentricity of the peak in the real ice autocorrelation was found to be 0.5962.

### *Analog Surface Generation*

The surface creation began with a random distribution of roughness elements created by a Lagrangian droplet simulator [39]. Figure 3.3 shows a multi-scale distribution of hemispheres that demonstrates the random size and placement of

roughness elements created by the simulator. Three parameters are used to designate roughness elements: 1) the streamwise location,  $X_i$ , 2) the spanwise location,  $Z_i$ , and 3) the element base diameter,  $D_i$ .

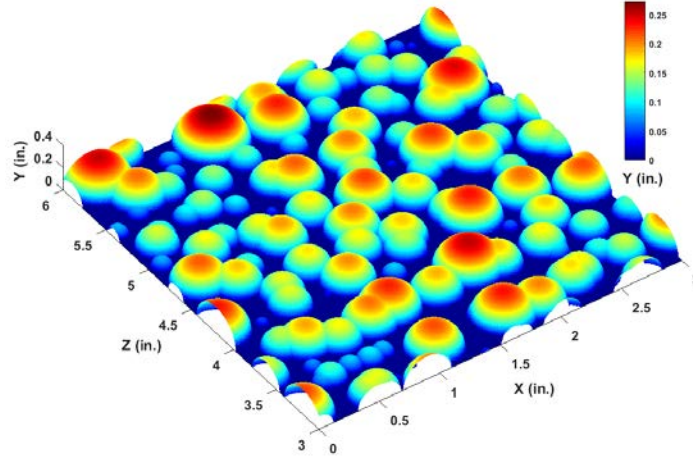


Figure 3.3: Multi-scale roughness distribution of hemispheres

To match the important surface features presented in Figure 3.8 using both ellipsoids and elliptical cones, the random distribution of elements was modified. The three parameters used to modify the distributions were the eccentricity attained from the surface microscales,  $\varepsilon$ , a diameter scaling factor,  $F_D$ , and a spanwise scaling factor,  $F_x$ . Eqs. (3.4 – 3.7) show the modification process to transform the random distributions into distributions of ellipsoids and elliptical cones.

$$a_i = F_D D_i \quad (3.4)$$

$$b_i = \frac{F_D}{\varepsilon} D_i \quad (3.5)$$

$$\tilde{Z}_i = \frac{F_D}{\varepsilon} Z_i \quad (3.6)$$

$$\tilde{X}_i = F_x X_i \quad (3.7)$$

In order to match the ridge spacing and root-mean-square height of the real ice surface, an iterative process varying the streamwise and spanwise element spacing was run in the surface generation program. Characterizing and matching the ice accretion ridge spacing was significant to the study as it allowed the analog surfaces to replicate the downstream eddy interactions found in the real ice surface.

Upon generation, an autocorrelation was applied to each of the new surfaces in the same region as that of the real ice surface. The figures were compared for surface matching confirmation. The centerline heights were also extracted from the autocorrelation data to compare the ice accretion ridge spacing of each surface in the streamwise direction. The autocorrelation results for each surface are shown in Figure 3.4 and the centerline heights extracted from the autocorrelation results are shown in Figure 3.5.

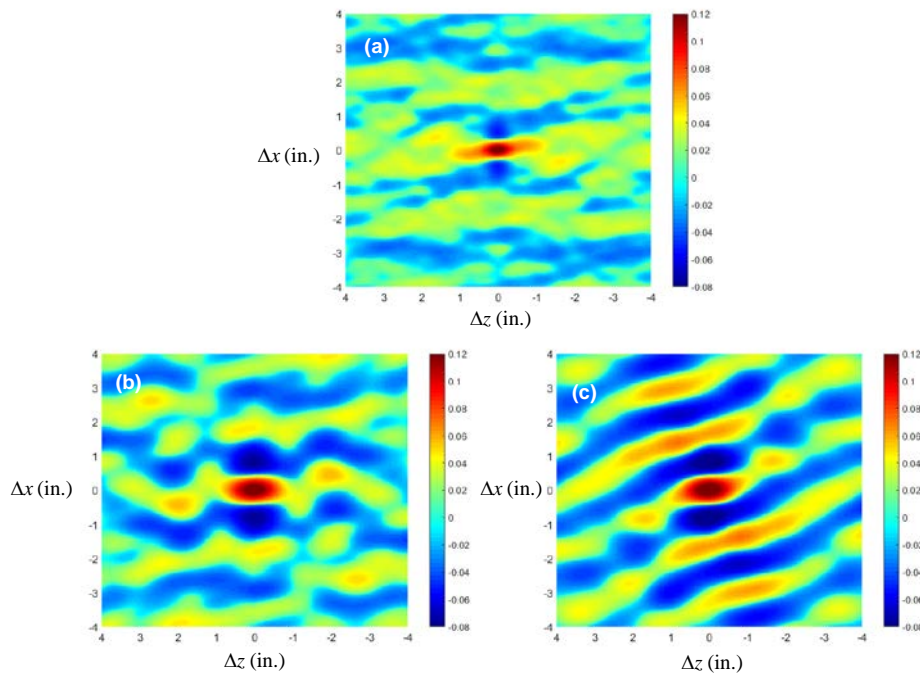


Figure 3.4: Autocorrelation comparison of a) real ice surface and b) ellipsoid surface, and c) elliptical cone surface

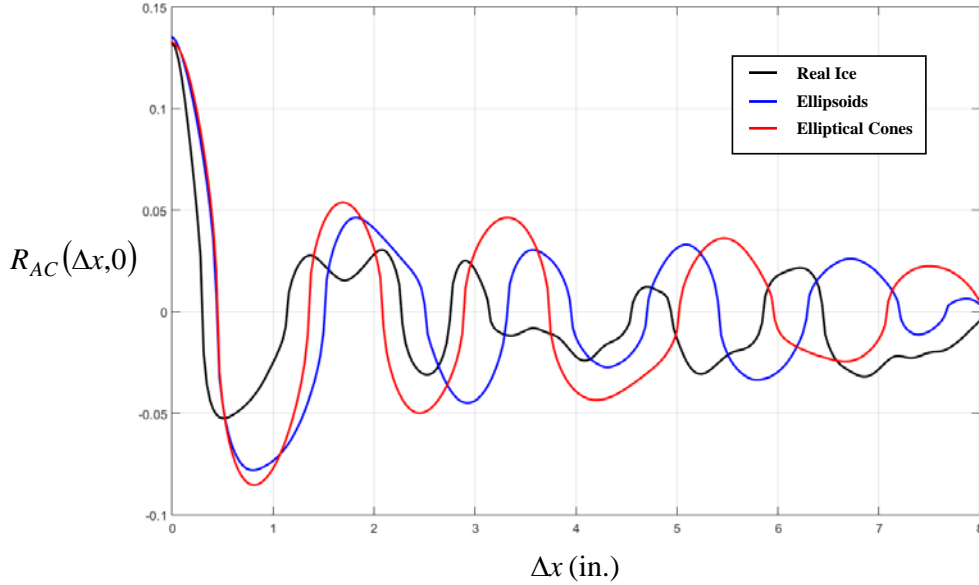


Figure 3.5: Streamwise centerline autocorrelation height comparison

As shown in Figure 3.5, the real ice 113012.04 surface exhibits a “double-hump” feature at the secondary ridge. Since the truly random features of the real ice surface were unattainable mathematically, the primary wavelength of the analog surfaces was placed at the center of the double-hump feature. The statistical results of the real ice surface and analog surfaces are presented in Table 3.1

Table 3.1: Comparison of sample statistics from the 113012.04 surface with sample statistics from the ellipsoidal analog and elliptical cone analog surfaces

Variable	113012.04_RealIce Section	113012.04_Ellipsoids Base Distribution	113012.04_EllipticalCones Base Distribution
$F_D$	~	1.5	2.14
$F_x$	~	4.79	4.0
$\varepsilon$	0.5962	0.5962	0.5962
$R_{AC}(0,0) = R_q$	0.132 in.	0.133 in.	0.135 in.
$\lambda$	1.34-2.06 in.	1.69 in.	1.81 in.

. While the double-hump feature was not captured in the analog surfaces, Table 3.1 shows that the root-mean-square and primary wavelength of the analog surfaces

match the real ice surface well. Table 3.1 also provides the values of  $F_D$  and  $F_x$  used for each analog surface. Different values were required for each surface because of the different roughness element shapes.

An additional scaling function,  $S_x(Z_i)$ , was used to scale the analog roughness element geometry in the streamwise direction to capture the full scale streamwise variation present in the real ice surface. The major axis dimensions,  $a_i$  and  $b_i$ , from Eqs. (3.4) and (3.5) were further modified using Eqs. (3.8) and (3.9).

$$a_i = F_D D_i S_x(Z_i) \quad (3.8)$$

$$b_i = \frac{F_D}{\varepsilon} D_i S_x(Z_i) \quad (3.9)$$

The scaling function consists of several hyperbolic tangent functions multiplied by a constant or a linearly-decreasing function and ranges from 0 to 1.0. Figure 3.6 shows the comparison of the real ice streamwise variation to the variation given by the scaling function applied to the analog surfaces. The full surfaces are shown in Figure 3.7. Surface statistics of the root-mean-square roughness height, skewness, and equivalent sand-grain roughness are displayed in Figure 3.8. The equivalent sand grain roughness is based on the Flack and Schultz [24] correlation in Eq. (3.10).

$$k_{s, \text{corr}} = 4.43 k_{rms} (1 + s_k)^{1.37} \quad (3.10)$$

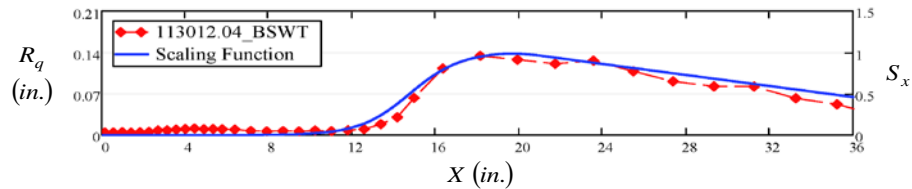


Figure 3.6: Unwrapped and Wind-Tunnel Scaled RMS Roughness Height Variation for the 113012.04 Surface and the Roughness Height Scaling Function

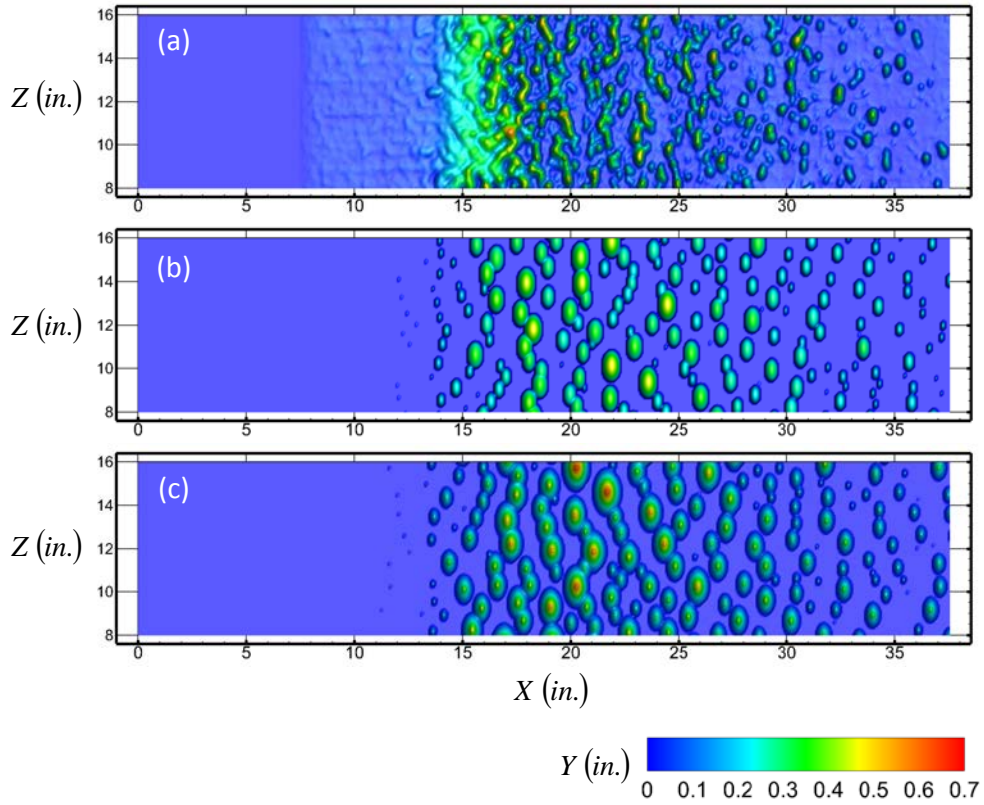


Figure 3.7: Solid models of a) real ice surface, b) ellipsoidal surface, and c) elliptical cone surface

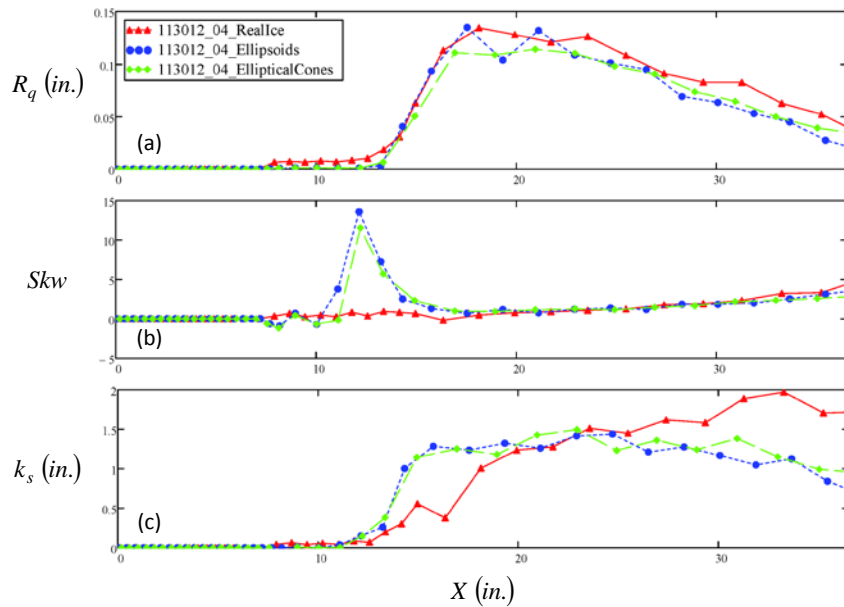


Figure 3.8: Surface statistics of the 113012.04 surface and analog surfaces: a) root-mean-square roughness height, b) skewness, c) equivalent sand-grain roughness

### *Manufacturing Model Surfaces*

Once the elliptical cone and ellipsoid surfaces were confirmed to match the real ice surface, a function was used to divide the surface into 16 panels. Each panel was then translated into an STL file to allow for 3D printing and CNC machining. The STL files of each panel were uploaded and 3D printed from ABS plastic using a Dimension SST 1200es printer. Along with full surface ABS plastic printing, the center row (Row C) of each surface was machined from Aluminum 6061 using a Haas VF 1 vertical-axis CNC mill to allow for testing of multiple materials. Row C of both the plastic and aluminum surfaces were backed with 1/16 in. neoprene to ensure even pressure across the panel and total contact between the surface panel and the thin film heaters on the test plate. Along with the neoprene, the panels were evenly coated with matte black paint to guarantee a known emissivity of 0.95. Coating the surfaces was crucial in accounting for radiation effects during the data reduction process for the heat transfer experiments.

### *Instrumented Test Plate*

In order to reproduce the conditions of the experiments of Anderson et al. [45], the test plate was designed to replicate the leading 17.1% (3.6") of a 21" NACA 0012 airfoil. This region lies directly downstream of the stagnation point of the airfoil where ice accretion is most prevalent. The 3.6" region was scaled by a factor of 10 from the leading edge resulting in a 36" test section to model the NACA 0012 airfoil. Due to the geometric scaling factor applied to the significant region of ice accretion, the test velocity used in testing was reduced by a factor of 10 so as to correspond to the Reynolds number of the airfoil.

Construction of the test plate was completed by Tecson [3]. The fundamental information about the plate significant to the experiments performed will be postulated below. For a more detailed understanding of the test plate and a complete account of construction, refer to Tecson [3]. The solid model of the test plate can be seen in Figure 3.9. In order to allow for testing of various ice accretion surfaces, the test plate was designed to house interchangeable panels that may be affixed to Plexiglas sub-plate. This eliminates the need to create a new test plate every time a new surface is created.

The four main subsystems that form the test plate to be described in greater detail are as follows: Plexiglas sub-plate, instrumentation and wiring, Mylar film heaters, and aerodynamic features.

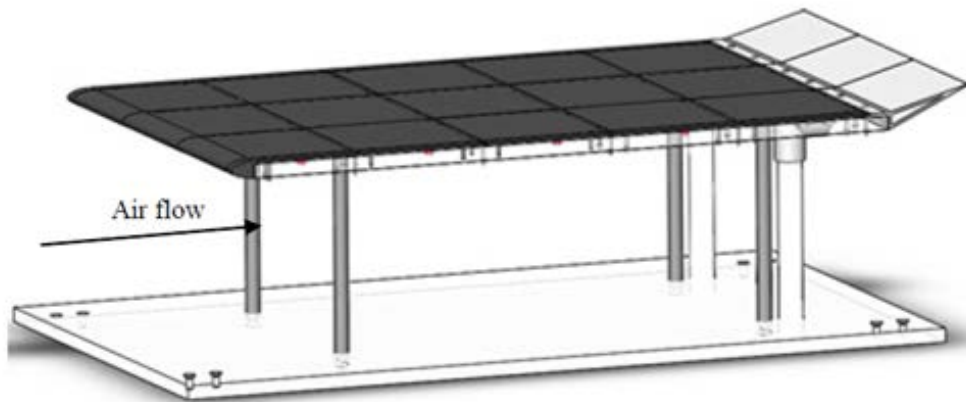


Figure 3.9: Solid model of test plate [3]

### *Plexiglas Sub-plate*

To house the interchangeable surface panels, a base plate measuring 24" x 36" x 0.75" was made of Plexiglas as shown in Figure 3.10. 0.035" channels were incised using a router with a 1/2" diameter straight bit to accommodate copper electrodes. The channels were cut to a depth to allow the copper electrodes to lie flush with the Plexiglas plate and

create clean contact with the thin film heaters. Additional channels were machined to place thermocouples inside the sub-plate. At each end of the thermocouple channels a through hole was drilled to create an exit for thermocouple wiring. Along with the copper electrode and thermocouple channels, 52 through holes were drilled where the surface panels are bolted to the sub-plate. The sub-plate is attached to the wind tunnel floor using four 0.75" diameter steel legs.



Figure 3.10: Plexiglas sub-plate [3]

### *Instrumentation and Wiring*

To capture subsurface temperatures for heat loss calculation, eight Type K thermocouples were implanted into the machined thermocouple channels mentioned previously using a plastic epoxy. All eight thermocouple beads were placed at the longitudinal centerline of the test plate at a depth of 1/16". Five of the eight thermocouples were placed at the center of each of the five heated sections. Of the remaining three thermocouples, two were added to the section closest to the leading and edge, and one to the second heated section. The additional thermocouples were included

in the design to distinguish heat loss gradients in the stream-wise direction. Along with the eight subsurface thermocouples, eight self-adhesive Type K thermocouples were applied directly below the thermocouple channels on the bottom of the plate to characterize heat loss through the plate. Each of the thermocouple pairs were numbered according to their corresponding heated section. Letters were used to designate the thermocouple pairs in the first two sections as they contain more than one pair. Figure 3.11 shows the location and label of each pair.

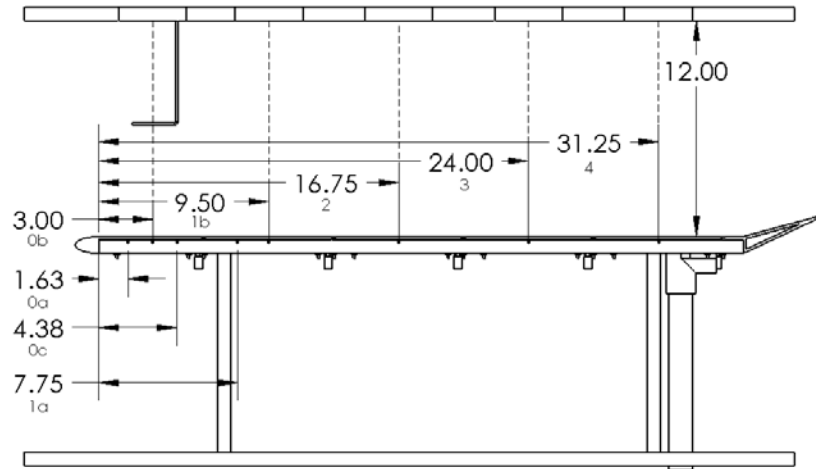


Figure 3.11: Side view of test plate showing thermocouple placement from the leading edge of the Plexiglas sub-plate (dimensions in inches, flow is from left to right) [3]

To calculate the distance from the leading edge of the test plate to the location of the thermocouple pair add 1.7825” to the dimensions reported in the figure. Along with the thermocouple pairs, copper electrodes were placed in the Plexiglas sub-plate and connected to terminal posts beneath the plate. Refer to Tecson [3] for a detailed description of the terminal wiring.

### *Mylar Film Heaters*

To create a nominally constant flux boundary condition, five independent gold-deposited Mylar thin film heaters were attached to the sub-plate and affixed between the copper electrodes as shown in Figure 3.12. Conductive silver paint was used to join each heater to the copper electrodes in order to minimize contact resistance.

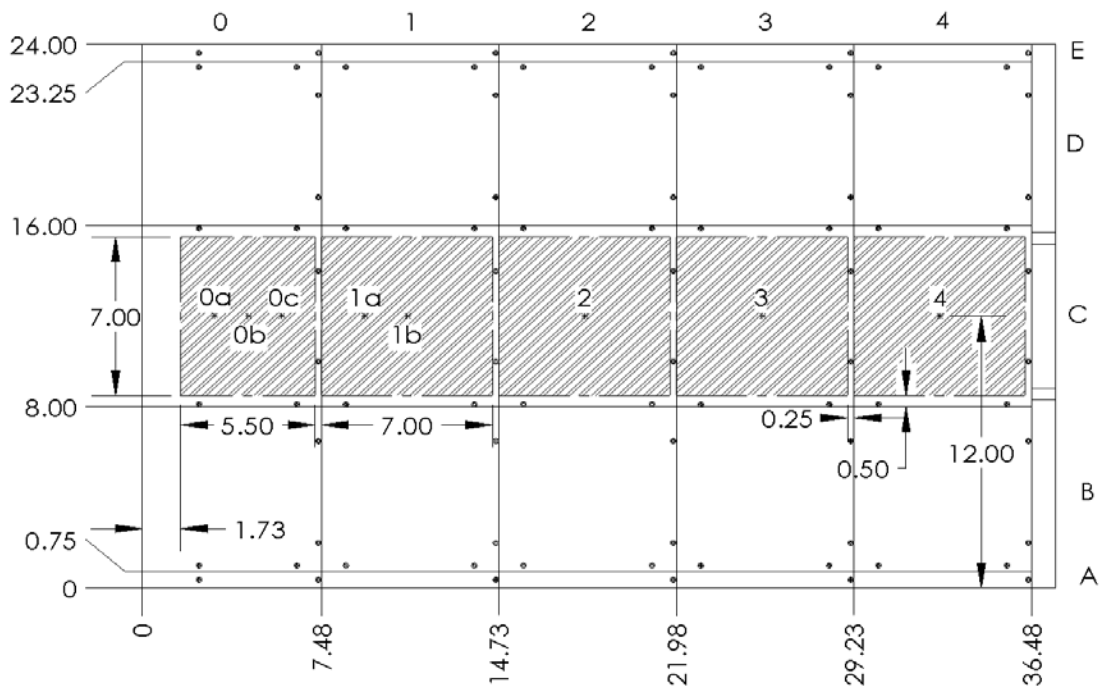


Figure 3.12: Layout of the heated sections on the Plexiglas sub-plate (dimensions in inches, flow is from left to right) [3]

Extreme care was taken during the installation of the heaters to ensure that no contaminants came in contact with the gold layer as this could result in uneven heating. Each heater was separated by a 0.25" space to allow for screw to pass through the lap joints of the surface panels. The location of each Mylar film heater on the test plate is represented by various shaded regions in Figure 3.12, along with the thermocouple placement represented by the numbers and letters where they apply.

### *Aerodynamic Features*

The design of the test plate included two significant aerodynamic features, a bullnose at the leading edge and a tail fin at the trailing edge. The bullnose was included in the design of the test plate to keep the flow attached at the leading edge of the test plate, preventing flow separation. The tail fin was included to counteract preferential flow migration from the bottom of the plate to the top due to the blockage underneath caused by various elements of the plate design. The frontal area of the tail fin was designed to equal the frontal area of the test plate legs, electrical connectors, and PVC pipes that cause the blockage underneath the plate. Refer to Figure 3.11 to see the aerodynamic features and their locations on the test plate.

### *Ceiling Insert for Flow Acceleration*

#### *Ceiling Insert Design*

A ceiling insert was designed to be placed inside the wind tunnel in order to accelerate the flow over the test plate. The design focused on matching the accelerated flow found along a 21” chord NACA 0012 airfoil at 0° angle of attack. To do this, the local Reynolds number variation of the test plate had to match that of the NACA 0012 airfoil as shown in Eq. (3.11).

$$\frac{\rho U_e x}{\mu} \Big|_{Plate} = \frac{\rho U_e s}{\mu} \Big|_{NACA 0012} \quad (3.11)$$

As a means of matching the local Reynolds number, the velocity and geometry are scaled. Eq. (3.11) shows that the flow along the test plate from the stagnation point downstream in the x-direction is matched to the flow from the stagnation point in the surface distance (s) of the NACA 0012 airfoil.

For a more detailed description of the ceiling insert design and manufacturing process refer to Shannon [7]. A brief description will be given for the purposes of the research conducted in this investigation. The design of the insert began with a vortex-panel solver that generated pressure coefficient variations along the surface of a NACA 0012 airfoil.

From the pressure coefficient variation, a velocity variation was found using Eq. (3.12) where a value of 10 was used for the surface geometry scaling factor.

$$U_e(x) = \frac{U_{\infty,IRT}}{F_s} (1 - C_p)^{1/2} \quad (3.12)$$

A plot of the resultant velocity variation can be seen in Figure 3.13.

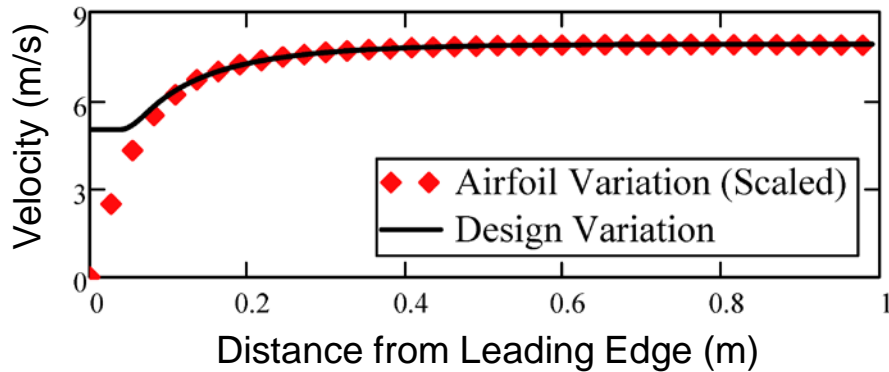


Figure 3.13: Scaled airfoil velocity variation and design velocity variation [7]

The velocity variation of the ceiling insert design was then chosen to match that of the flow around the surface of the NACA 0012 airfoil. It is important to note that the acceleration near the stagnation of the airfoil (the first 0.02%) was not matched. Due to the use of a flat plate and ceiling insert, flow stagnation cannot easily be achieved when attempting to model flow acceleration. To overcome this issue, a “cut-in” velocity of 5 m/s was used. This means that the ceiling insert was designed to impart a velocity of 5

m/s over the unheated bullnose section of the test plate. The design velocity variation then converges to the velocity variation of the airfoil just downstream of the bullnose region.

A boundary layer code was then used to calculate the momentum thickness growth on the test plate and the ceiling of the wind tunnel from the imported velocity variation. From the momentum thickness growth calculations, the thickness profile of the ceiling insert was formulated and used for the construction of the insert.

### *Ceiling Insert Construction*

A solid model of the ceiling insert is shown in Figure 3.14. A hot wire CNC foam cutter was used to cut surfboard foam in the shape of the desired ceiling insert profile. A recess was removed from the top of the foam insert to house a wood mounting plate so that the insert could be attached to the ceiling of the wind tunnel. The five cylindrical ports in the insert are located directly above the center of each heated section to allow for infrared measurements to be taken during testing. Upon inspection of Figure 3.14, it can be seen that the viewing port closest to the leading edge of the insert has a smaller diameter than the other viewing ports. This was done in order to minimize the interference of the leading port with the flow over the curved profile of the insert.

### *Experimental Setup and Procedure*

The tests were performed in the Baylor University Subsonic Wind Tunnel (BUSWT), a model 406B manufactured by Engineering Design Laboratory, Inc. A constant pitch fan powered by a 40 horsepower variable speed motor drives the flow. The fan is capable of generating flow ranging from 0.1 m/s to 50 m/s with a velocity variation

of less than  $\pm 1\%$ . The test section of the wind tunnel has cross-sectional dimensions of 24" x 24", with a length of 48" in the streamwise direction. The tunnel utilizes a honeycomb inlet and three high-porosity screens to deliver a turbulence intensity of approximately 0.2% at the inlet.

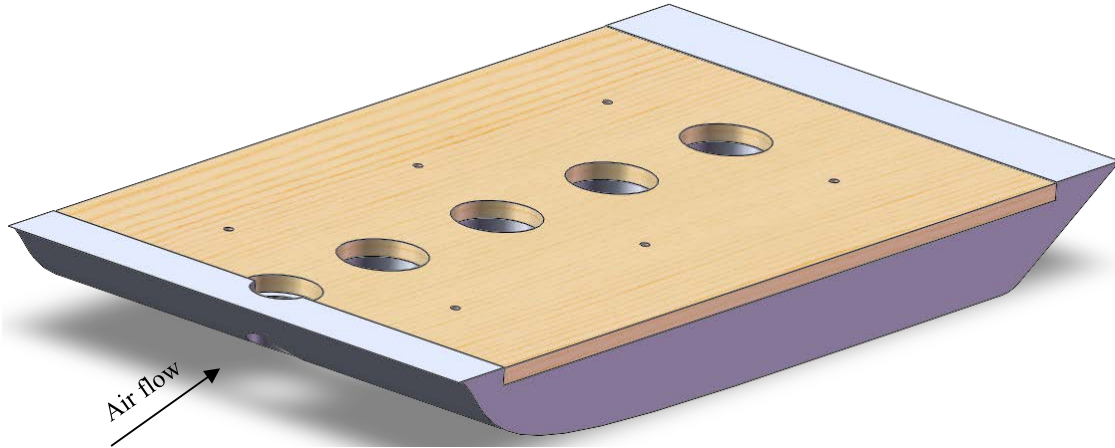


Figure 3.14: Solid model of ceiling insert [7]

Two types of experiments were performed for each of the surfaces involved in this investigation. First, steady-state convective heat transfer coefficient measurements were made on plastic and aluminum surfaces to examine the thermal properties of each surface. Second, velocity boundary layer measurements were taken for each surface to characterize the airflow over the roughness elements. The experimental setups for these experiments are shown in Figure 3.15. The following sections describe the setup and experimental procedures implemented in this study.

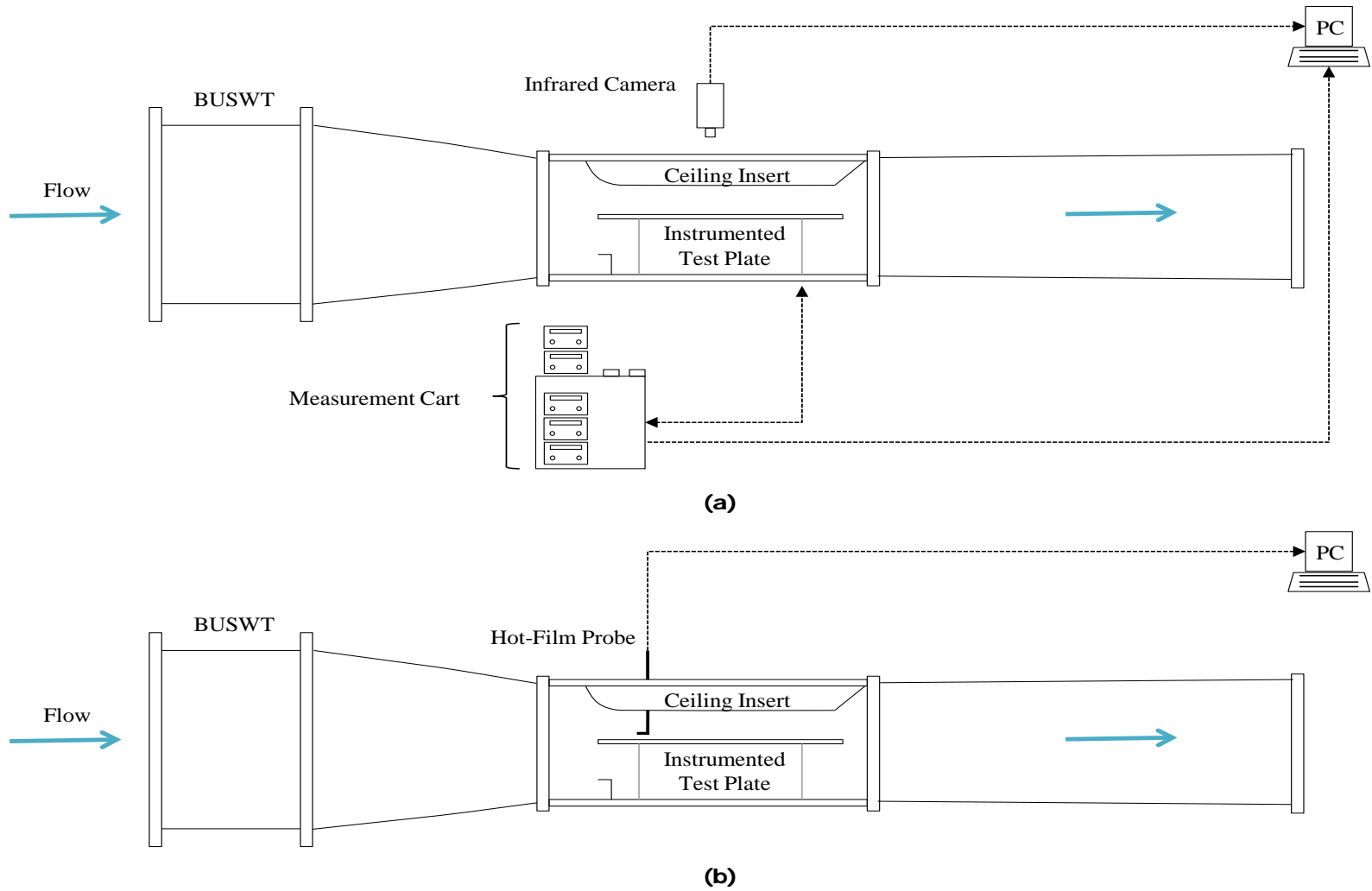


Figure 3.15: Side view of experimental setups for a) the convection tests and b) velocity boundary layer tests (not to scale) [7]

### *Convection Measurements*

A FLIR SC4000 ThermoVision IR camera with a 25 mm lens was utilized to capture the convection measurements. The camera has an indium-antimonide (InSb) detector that is able to generate 320 x 256 pixel temperature maps across a surface. Each image taken by the camera had a viewing area of 6.4” in the streamwise direction and 5.12” in the spanwise direction. The IR camera data was recorded using FLIR ExaminIR software.

The wind tunnel ceiling was designed with five viewing ports to permit image recording. Above each viewing port a FLIR IRW-3C calcium-fluoride window was installed to allow infrared access to each heated section of the test plate. The windows were mounted at an angle of 30° to eliminate reflection from the IR camera. The camera was positioned above each viewing port using a one-dimensional Velmex BiSlide traversing system. The traversing system, camera setup, and FLIR infrared windows can be seen in Figure 3.16.

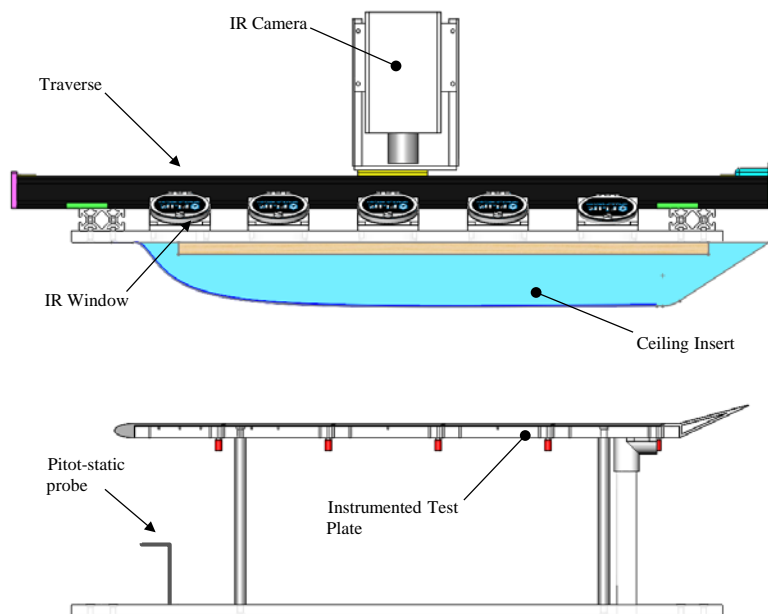


Figure 3.16: Side view of convection test section [7]

The freestream velocity was surveyed using a 6” Pitot-static probe and an Omega PCL-2A pressure transducer with a PCL MA-01 WC pressure module. The freestream temperature was measured using a Type K thermocouple joined to the Pitot-Static probe. An Omega zSeries-THBP-LCD atmospheric conditions monitor was employed to measure the ambient pressure, temperature, and relative humidity during testing. For the tests with negligible freestream acceleration, the Pitot-static probe was inserted from the ceiling of the tunnel. During the tests implementing the ceiling insert for freestream acceleration, the probe was mounted on the floor of the wind tunnel to circumvent interference with the insert. Shannon [7] performed a calibration procedure to ensure the freestream velocity desired over the top surface of the test plate was achieved with the ceiling insert installed. The dynamic pressure measured by the floor installed Pitot-static probe during this calibration process was recorded by Shannon. For repeatability in testing, the wind tunnel velocity was set by matching this pressure for all cases involving freestream acceleration. For the negligible freestream acceleration cases, the wind tunnel velocity was set at 6.7 m/s to ensure repeatability.

Tecson [3] modified a wooden rolling cart to house the following accompanying equipment required for the experiments:

- Five BK Precision power supplies, one for each heated section, used to provide power to the Mylar film heaters
- National Instruments (NI) 9929 DAQ Module used to measure the voltage across heated Sections 0-3
- Two Newport TrueRMS HHM290/N Supermeters used to measure the voltage across and current through heated Section 4

- One Powertek CTH/20A/TH/24Vdc Type 1 current transducer used to measure the current through heated Section 0
- Three Powertek CTH/10A/TH/24Vdc Type 1 current transducers used to measure the current through heated Sections 1-3
- NI 9205 DAQ Module used to read the outputs from the current transducers
- Five NI 9211 DAQ modules used to record the thermocouple measurements from the eight thermocouple pairs attached to the test plate and one freestream thermocouple
- Two NI cDAQ-9172 chassis, one to house the thermocouple DAQ modules and the other to house the current and voltage DAQ modules

The outputs from the DAQ modules were read using LabVIEW software. The equipped cart is shown in Figure 3.17. The Supermeters used to measure the voltage across and current through the Section 4 heater were used due to equipment availability.

A day before performing each convection test, the desired surface panels were affixed to the test plate and the plate was installed in the wind tunnel test section along with the Pitot-static probe. The equipment on the modified wood cart was then connected to the test plate and the LabVIEW program used to record data was run to ensure the thermocouples and power supplies were connected correctly. A black felt sheet was placed over the test section to reduce light contamination and radiation interference with the IR camera and the camera was then focused. To guarantee nominal temperature equilibrium of the test plate and ambient air, the test section was left undisturbed overnight.

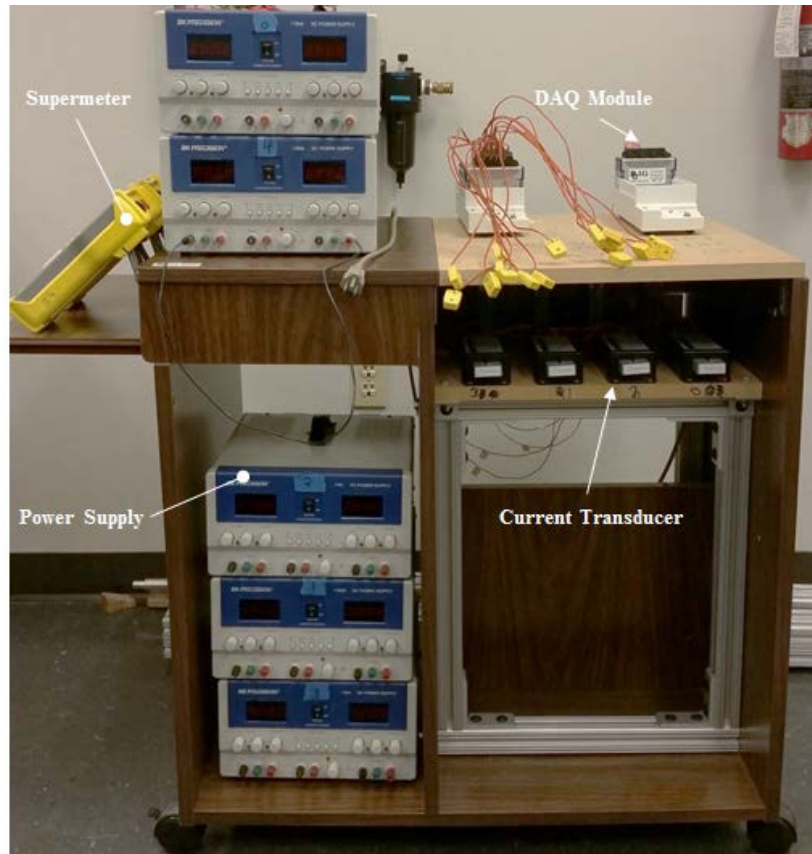


Figure 3.17: Modified wood cart outfitted with experimental equipment [7]

The following procedure was performed on the day of the convection test:

1. The IR camera was powered on and left undisturbed for fifteen minutes to allow the detector to reach operating temperature.
2. The current transducers, PCL-2A pressure transducer, DAQ systems, and camera traversing system were powered on.
3. Two LabVIEW programs were started. The first was used to read the zSeries, PCL-2A pressure measurements, and DAQ temperature, voltage, and current. The second program was used to control the traversing system for positioning the IR camera.

4. The ExaminIR software was started and calibration images were taken at each of the five heated sections. The IR camera recorded 7 frames per second for 10 seconds for a total of 70 frames per section. It is important to note that the wind tunnel was not powered on during calibration.
5. The PCL-2A pressure transducer was zeroed. The wind tunnel was then started and the velocity was set to match a dynamic pressure of 0.1595 inH<sub>2</sub>O measured by the floor Pitot-static probe [7].
6. The five power sources connected to the Mylar film heaters were powered on. Each power source was adjusted to provide a nominal heat flux of 500 W/m<sup>2</sup> to the respective heater. The heat flux for Sections 0-3 were read from the LabVIEW program. Section 4 was adjusted based on the power output calculated by multiplying the voltage and current read from the Supermeters.
7. The LabVIEW program was used to monitor the temperatures of the thermocouple pairs attached to the test plate until each thermocouple reached steady-state. This commonly took 2 hours.
8. The IR camera was used to capture steady-state images at each of the heated sections. Similarly to the calibration process, 70 frames were recorded at a rate of 7 frames per second.
9. When the IR camera captured the Section 4 images, the voltage and current were manually recorded by reading the Supermeters.
10. The LabVIEW program was stopped and the equipment was powered down beginning with the power supplies.

### *Velocity Boundary Layer Measurements*

To understand the nature of the flow over the test surfaces, velocity boundary layer measurements were taken at the center of each heated section. A model 1246-20 x-array hot film probe was used to perform hotwire anemometry tests to characterize the velocity boundary layers. Along with the x-array probe, the PCL-2A pressure transducer, Pitot-static probe, and zSeries atmospheric conditions monitor from the previous tests were used. The test plate was not heated for the boundary layer tests, so temperature and power measurements were not recorded and the equipment on the modified wooden cart was not used. To allow for vertical traversing with the hot wire probe, the test section ceiling was modified to house a Velmex two-dimensional traversing system as shown in Figure 3.18. The probe was powered by a TSI Inc., IFA 300 constant temperature anemometry system. ThermalPro software was implemented to initialize the IFA 300 and assign channels to the x-array probe.

Prior to testing, the probe was calibrated without the ceiling insert in the wind tunnel test section. The probe was attached to a Velmex B487TS rotary table that was controlled by a LabVIEW program. The program rotated the probe in  $5^\circ$  increments over a range of  $\pm 20^\circ$  while a velocity sweep ranging from 0-20 m/s was performed at each rotation angle. An NI 9223 DAQ module in an NI cDAQ-9178 chassis was used to capture the velocity data of each wire at every rotation angle and freestream velocity.

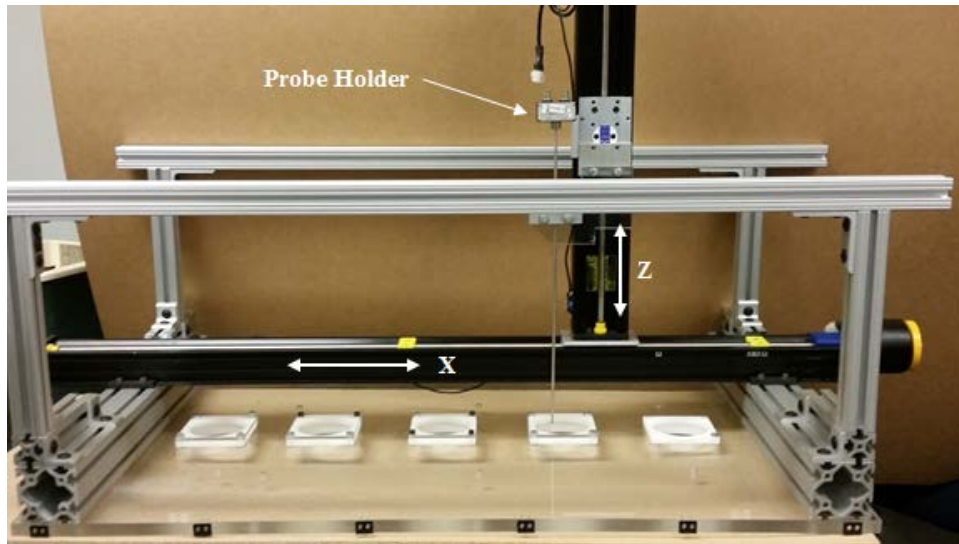


Figure 3.18: Wind tunnel ceiling with two-dimensional traversing system [7]

The freestream velocity in the wind tunnel for the boundary layer tests was set using the same method used for the convection heat transfer tests. The x-array probe was positioned over the center of each test plate and lowered through the measurement ports in the ceiling. The probe was situated as close to the surface of the test plate as possible (within  $1/64''$ ). The measurement port in use at each section was sealed with special foam guards to allow the probe access into the test section. The ports not in use were sealed with Plexiglas squares that were screwed into the ceiling of the test section. After the probe was positioned, a LabVIEW program was used to perform a boundary layer scan by raising the probe in the Z-direction. The probe was traversed through a 6", 101 station, geometrically expanding grid with an expansion factor of 1.07. An NI 9223 DAQ module in an NI cDaq-9178 chassis captured velocity data at each of the 101 measurement stations. At each station, 300,000 samples were taken from each wire at a rate of 200,000 samples per second.

Convection Measurements

A one-dimensional energy balance was implemented to track the heat transfer in the test section for the steady state convection measurements. Four modes of heat transfer were considered in the data reduction process and can be seen in Figure 3.19.

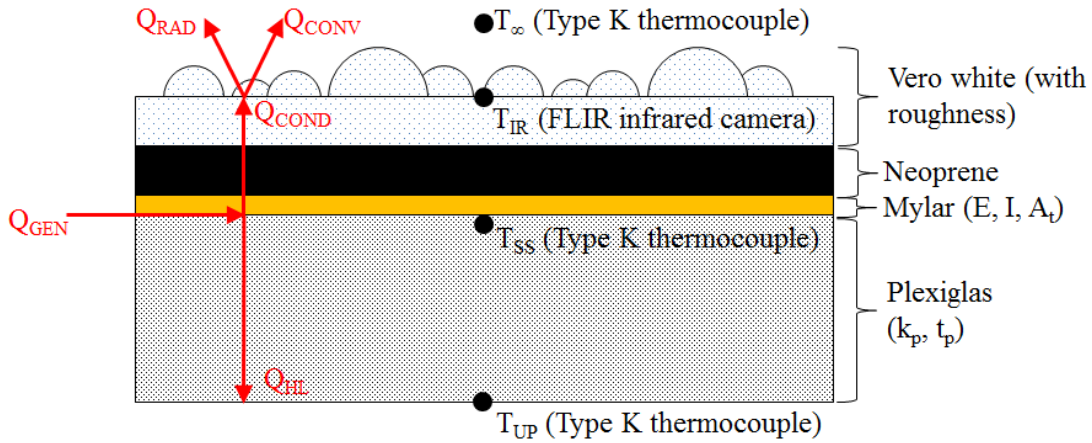


Figure 3.19: Heated section one-dimensional heat schematic (not to scale) [7]

Heat is added to the test section system through the power supplied to the Mylar film heaters ( $Q_{GEN}$ ). The three modes of heat loss considered are the conduction losses through the Plexiglas sub-plate ( $Q_{HL}$ ), losses due to radiation from the test surface ( $Q_{RAD}$ ), and the heat convected away from the test surface ( $Q_{CONV}$ ). Applying a one-dimensional energy balance with the four modes of heat transfer measured results in Eq. (3.13).

$$Q_{GEN} = Q_{HL} + Q_{RAD} + Q_{CONV} \quad (3.13)$$

Eq. (3.13) is then broken down further to solve for the heat transfer coefficient. The generation term, heat added to the system by the Mylar film heater on a per pixel basis, is given by Eq. (3.14). Using Ohm's law of power,  $E$  represents the voltage across

the thin film heater,  $I$  is the current through the thin film heater,  $A_{pix}$  is the pixel area, and  $A_t$  is the total area of the thin film heater.

$$Q_{GEN} = EI \frac{A_{pix}}{A_t} \quad (3.14)$$

Fourier's law of conduction is used to account for the conductive heat loss through the Plexiglas sub-plate. Eq. (3.15) shows the conductive heat loss term on a per pixel basis where  $k_p$  is the Plexiglas thermal conductivity,  $t_p$  is the thickness of the sub-plate,  $T_{ss}$  is the subsurface temperature of the sub-plate recorded from the thermocouples embedded in the plate,  $T_{UP}$  is the temperature recorded from the thermocouples placed on the bottom of the plate directly underneath the embedded thermocouples, and  $C_k$  is the conduction parameter.

$$Q_{HL} = C_k \frac{k_p A_{pix} (T_{SS} - T_{UP})}{t_p} \quad (3.15)$$

Stefan-Boltzmann's law of radiation is used to account for losses due to radiation from the surface panels. Eq. (3.16) represents the heat loss due to radiation on a per pixel basis, where  $\varepsilon$  is the known surface panel emissivity,  $\sigma$  is the Stefan-Boltzmann constant,  $T_{IR}$  is the pixel surface temperature measured by the infrared camera, and  $T_\infty$  is the measured freestream temperature.

$$Q_{RAD} = \varepsilon \sigma A_{pix} (T_{IR}^4 - T_\infty^4) \quad (3.16)$$

Newton's law of cooling is used to account for the heat loss due to convection. Eq. (3.17) shows the calculation based on a per pixel basis where  $T_{IR}$ ,  $T_\infty$ , and  $A_{pix}$  are the same values mentioned above and  $h$  is the convective heat transfer coefficient.

$$Q_{CONV} = h A_{pix} (T_{IR} - T_\infty) \quad (3.17)$$

Eqs. (3.14) – (3.17) are then substituted into Eq. (3.13) to solve for the convective heat transfer coefficient at each pixel, given by Eq. (3.18).

$$h = \frac{\frac{EI}{A_t} - C_k \frac{k_p (T_{SS} - T_{UP})}{t_p} - \varepsilon \sigma (T_{IR}^4 - T_\infty^4)}{T_{IR} - T_\infty} \quad (3.18)$$

During the derivation of Eq. (3.18), Walker [4] made three major assumptions. First, that lateral conduction in the spanwise direction is negligible allowing application of a one-dimensional model. Second, that a uniform flux is generated by the Mylar film heaters. Third, that the heat loss through the Plexiglas sub-plate is constant across each heated section, as measured by the middle thermocouple pair.

Throughout validation of the instrumented test plate, Walker [4] found that the convective heat transfer coefficients for the smooth-laminar and smooth-turbulent cases did match those of accepted theoretical correlations. Upon investigation, Walker found that using the accepted thermal conductivity of Plexiglas was not accurate due to the embedded thermocouples being coated in epoxy. Therefore, Walker found a correction factor,  $C_k$  (as seen in Eq. (3.15) and Eq. (3.18)), to match theoretical correlations. Each heated section of the test area has a different conduction parameter and the values can be seen in Table 3.2. For a more in depth account of the experiments run to find each conduction parameter refer to Walker [4].

### *Air Properties*

Due to the testing of multiple surfaces and the time required for each experiment, the data sets were recorded over a period of several weeks. To compare the convection measurements, non-dimension Stanton numbers were used requiring the examination of the air properties during each test. The properties recorded include the ambient air

temperature, pressure, and relative humidity at the inlet of the wind tunnel. An Omega zSeries zED-THPB-LCD was used to record the values. The method used for obtaining air properties is the same as that of Tecson [3], Walker [4], Shannon [7], and Hawkins [8]. Using a program implementing the International Association for the Properties of Water and Steam guidelines [46], Sutherland's Law [47], and Wilke's equation for gas mixtures [48], the air density, dynamic viscosity, specific heat, thermal conductivity, and Prandtl number were calculated. These values were then used to calculate the Stanton numbers used to compare the data sets.

Table 3.2: Conduction parameter values [4]

Heated Section Number	$C_k$
0	0.90
1	0.90
2	1.05
3	1.10
4	1.05

### *Thermocouple Calibration*

The thermocouples were calibrated using an *in situ* calibration. A region of pixel temperatures measured by the IR camera was averaged as a reference for the thermocouple calibration. Eq. (3.19) shows this process.

$$T_{TC,calibrated} = T_{TC,test} - (T_{TC,cal} - \bar{T}_{IR,cal}) \quad (3.19)$$

The pixel regions used to obtain the average temperature  $\bar{T}_{IR,cal}$  were square regions centered on the thermocouple pairs. The averaged center pixel regions used were

50x50 (1" square) and 100x100 (2" square), consistent with Hawkins [8]. The thermocouples were calibrated to the IR camera measurement by section. For example, the thermocouples in heated Section 1 were calibrated using the IR temperature measurements taken by the camera at Section 1.

### *Smooth Surface Validation*

Smooth surface panels were placed on the instrumented test plate and a set of convection experiments run to validate Eq. (3.18), the derived convective heat transfer equation. The heat transfer coefficients were compared to theoretical values of flat plate flow. Walker [4] validated laminar and turbulent flows with negligible acceleration and Shannon [7] validated accelerated laminar and turbulent flows. The experiments performed for the purposes of this paper share an identical setup to that of the validation experiments performed by Walker and Shannon.

### *Uncertainty Analysis*

Uncertainties of the area averaged heat transfer coefficients displayed in Chapter Five were calculated based on the method used by Shannon [7], and Hawkins [8]. Using the large sample size method of Coleman and Steele [49], an expansion of the work of Kline and McClintock [50], the uncertainties of the heat transfer coefficients were found. The total uncertainty of each variable present in Eq. (3.18) is shown in Table 3.3.

Table 3.3: Convective Heat Transfer Coefficient Measurement Uncertainty [7]

Variable	Total Uncertainty	Uncertainty Components
$E$	$\sqrt{U_{E, fixed}^2 + \left(\frac{tS_E}{\sqrt{N}}\right)^2}$	$U_{E, fixed} = 0.03\% E$ (sections 0 - 3) $U_{E, fixed} = 0.25\% E$ (section 4)
$I$	$\sqrt{U_{I, fixed}^2 + \left(\frac{tS_I}{\sqrt{N}}\right)^2}$	$U_{I, fixed} = 0.1 A$ (section 0) $U_{I, fixed} = 0.05 A$ (sections 1 - 3) $U_{I, fixed} = 2.5\% I$ (section 4)
$A_t$	$\sqrt{(U_{d, fixed} W_{ha})^2 + (U_{d, fixed} L_{ha})^2}$	$U_{d, fixed} = 1/32''$
$T_{IR}$	$\sqrt{B_T^2 + \left(\frac{tS_{T_{IR}}}{\sqrt{N}}\right)^2}$	$B_T = 1.4 K$
$T_{SS}$	$\sqrt{B_T^2 + \left(\frac{tS_{T_{IR}}}{\sqrt{N}}\right)_{cal}^2 + \left(\frac{tS_{T_{SS}}}{\sqrt{N}}\right)_{cal}^2 + \left(\frac{tS_{T_{SS}}}{\sqrt{N}}\right)_{test}^2}$	$B_T = 1.4 K$
$T_{UP}$	$\sqrt{B_T^2 + \left(\frac{tS_{T_{IR}}}{\sqrt{N}}\right)_{cal}^2 + \left(\frac{tS_{T_{UP}}}{\sqrt{N}}\right)_{cal}^2 + \left(\frac{tS_{T_{UP}}}{\sqrt{N}}\right)_{test}^2}$	$B_T = 1.4 K$
$T_{\infty}$	$\sqrt{B_T^2 + \left(\frac{tS_{T_{IR}}}{\sqrt{N}}\right)_{cal}^2 + \left(\frac{tS_{T_{\infty}}}{\sqrt{N}}\right)_{test}^2}$	$B_T = 1.4 K$

The random uncertainty of each variable is found using Eq. (3.20), where  $t$  is the Student's t-value,  $S$  is the standard deviation of the measurement, and  $N$  is the sample size.

$$U_{random} = \frac{t \cdot S}{\sqrt{N}} \quad (3.20)$$

The uncertainty related to the thickness of the Plexiglas sub-plate is not considered as it is accounted for in the conduction correction factor. Refer to Walker [4] for further explanation.

### *Velocity Boundary Layer Measurements*

The x-array probe was calibrated by sampling multiple velocities at known angles in a rotary holder. Eqs. (3.21) and (3.22) were used to calculate the effective velocity experienced by each wire of the x-array probe. In these equations,  $V_{meas}$  is the velocity measured by the Pitot-static probe,  $\alpha$  is the angle of the wire relative to the flow direction, and  $\kappa$  is the tangential velocity attenuation factor. The value of  $\kappa$  for each wire was 0.115 as reported by the probe manufacturer.

$$V_{eff,1} = \sqrt{(V_{meas} \cos \alpha_1)^2 + \kappa^2 (V_{meas} \sin \alpha_1)^2} \quad (3.21)$$

$$V_{eff,2} = \sqrt{(V_{meas} \sin \alpha_2)^2 + \kappa^2 (V_{meas} \cos \alpha_2)^2} \quad (3.22)$$

A fourth-order polynomial was then fit to the calculated effective velocities for each wire of the x-array probe to complete probe calibration, as shown in Figure 3.20.

The normal and tangential flow velocity components experienced by the x-array probe were obtained using an identical method to Shannon [7]. Using the voltage measurements taken during boundary layer testing, the flow velocity normal and flow velocity tangent to the first wire of the probe were assessed using Eqs. (3.23) and (3.24), respectively.

$$V_{N1} = \left( \frac{V_{eff,1}^2 - \kappa^2 V_{eff,2}^2}{1 - \kappa^4} \right)^{1/2} \quad (3.23)$$

$$V_{T1} = \left( \frac{V_{eff,2}^2 - \kappa^2 V_{eff,1}^2}{1 - \kappa^4} \right)^{1/2} \quad (3.24)$$

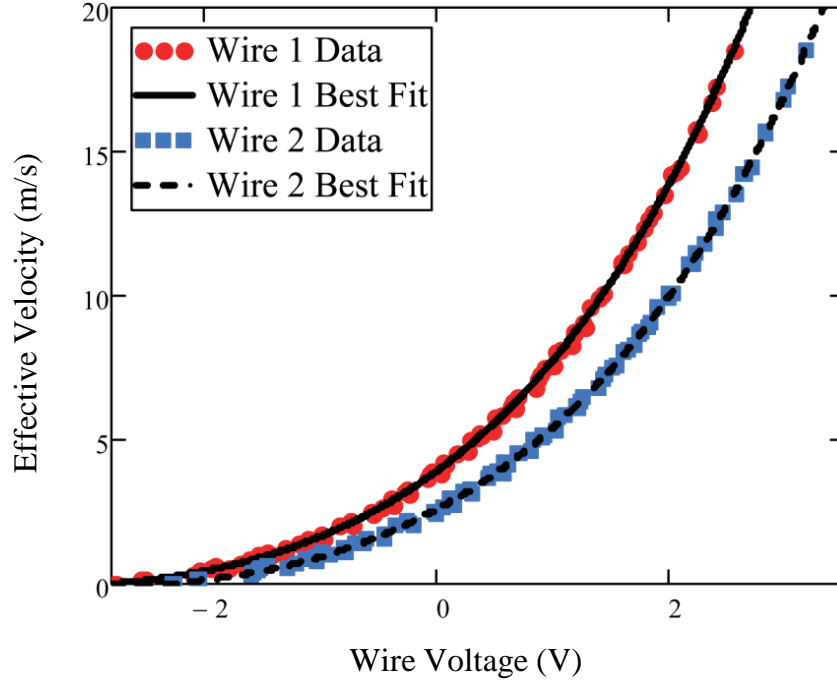


Figure 3.20: Hot-film probe calibration plot

From the normal and tangential components, the x and z-components of the flow velocity relative to the probe were calculated using Eqs. (3.25) and (3.26), respectively.

$$u_i = \frac{V_{T1} + V_{N1}}{\sqrt{2}} \quad (3.25)$$

$$w_i = \frac{V_{T1} - V_{N1}}{\sqrt{2}} \quad (3.26)$$

The mean velocity components at each of the 101 measurement stations are determined using Eqs. (3.27) and (3.28).

$$\bar{u} = \frac{1}{N} \sum_{i=1}^N u_i \quad (3.27)$$

$$\bar{w} = \frac{1}{N} \sum_{i=1}^N w_i \quad (3.28)$$

Lastly, the root-mean-square of the turbulent fluctuating velocity components are determined using Eqs. (3.29) and (3.30).

$$u'_{RMS} = \sqrt{\frac{1}{N-1} \sum_{i=1}^N (u_i - \bar{u})^2} \quad (3.29)$$

$$w'_{RMS} = \sqrt{\frac{1}{N-1} \sum_{i=1}^N (w_i - \bar{w})^2} \quad (3.30)$$

## CHAPTER FOUR

### Results and Discussion

This chapter presents the results of the convection heat transfer tests for the ellipsoid and elliptical cone surfaces in comparison to the 113012.04 RealIce surface with and without freestream acceleration. All data concerning the 113012.04 RealIce surface was first presented by Hawkins [8] and is replicated here for comparison. The smooth turbulent and smooth laminar correlations used in the Stanton number plots were acquired from Walker [4] for the negligible acceleration cases and from Shannon [7] for the accelerated cases. The results of the velocity boundary layer tests for the previously mentioned surfaces are also presented and discussed in this chapter. The data sets for all tests are given in Appendix A.

#### *Convection Results*

The local heat transfer coefficient contour maps for the negligible freestream acceleration cases (i.e. without ceiling insert) are displayed in Figures 4.1 and 4.2. The results from the three plastic surfaces investigated are shown in Figure 4.1 and the aluminum surface results are shown in Figure 4.2. As expected, the heat transfer coefficients for the aluminum surfaces are higher than those of the plastic surfaces. The contour maps of the ellipsoid and elliptical cone surfaces match the RealIce surface well in heated Sections 0-3 for both the plastic and aluminum surfaces. For both materials the RealIce surface displays slightly higher heat transfer coefficients in heated Section 4 due to scattered roughness elements causing more convection from the surface panel. Further,

the two analog surfaces match nearly exactly upon inspection of the contour maps. This result is important to this study as it shows the surface generation method is capable of repeatability regardless of the shape implemented to replicate roughness.

The local heat transfer coefficient contour maps of the cases with freestream acceleration for the three surfaces tested are shown in Figures 4.3 and 4.4. Figure 4.3 shows the plastic surface results and Figure 4.4 shows the aluminum surface results. The heat transfer coefficients for the accelerated cases are higher than those of the negligible acceleration cases as expected. For the accelerated flow cases, the same data trends from the negligible acceleration cases appear between the analog surfaces and the RealIce surface. Heated Section 4 has slightly higher heat transfer and the model surfaces match one another well.

For a more detailed comparison of the test results, the area averaged heat transfer coefficients were used to calculate localized Stanton numbers. A 2" square (100x100 pixels) centered on each of the thermocouple pairs affixed to the Plexiglas sub-plate was averaged to find the heat transfer coefficient used in the Stanton number calculation. As mentioned in Chapter Three, the non-dimensional Stanton numbers take air properties into account, allowing for a detailed comparison of surfaces tested over a period of weeks. The Stanton numbers are plotted against non-dimensional Reynolds numbers that were calculated using the air properties and velocities recorded during testing. Figure 4.5 displays the Stanton number results for each case comparing the real ice and analog surfaces. Figures 4.6 and 4.7 display the Stanton number results for the previously simulated IRT surfaces along with the real ice surface and analog surfaces. Figure 4.6 is for flow with negligible acceleration and Figure 4.7 is for accelerated flow.

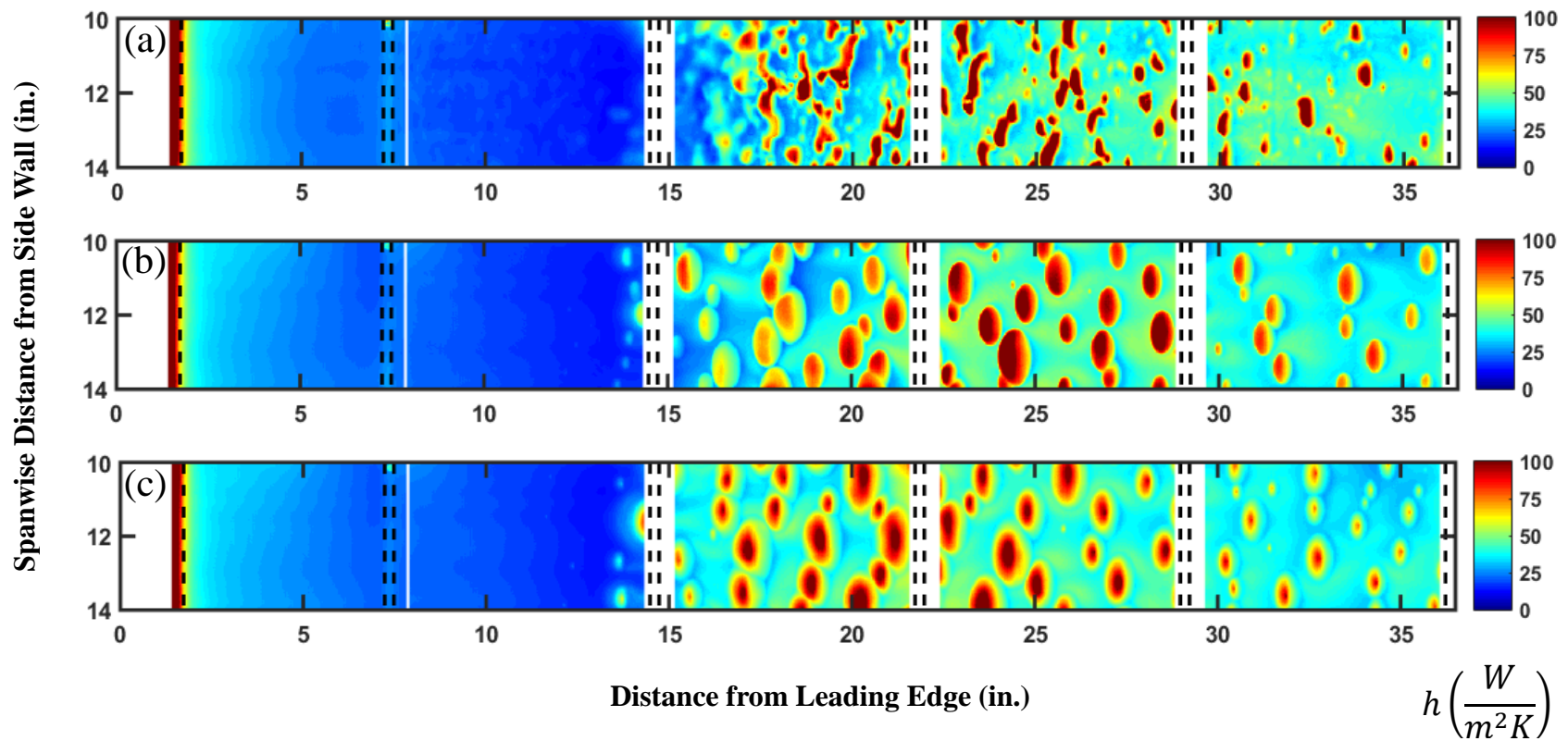


Figure 4.1: Convection coefficient contour maps of plastic surfaces without ceiling insert for the a) 113012.04 RealIce surface, b) ellipsoid surface, and c) elliptical cone surface

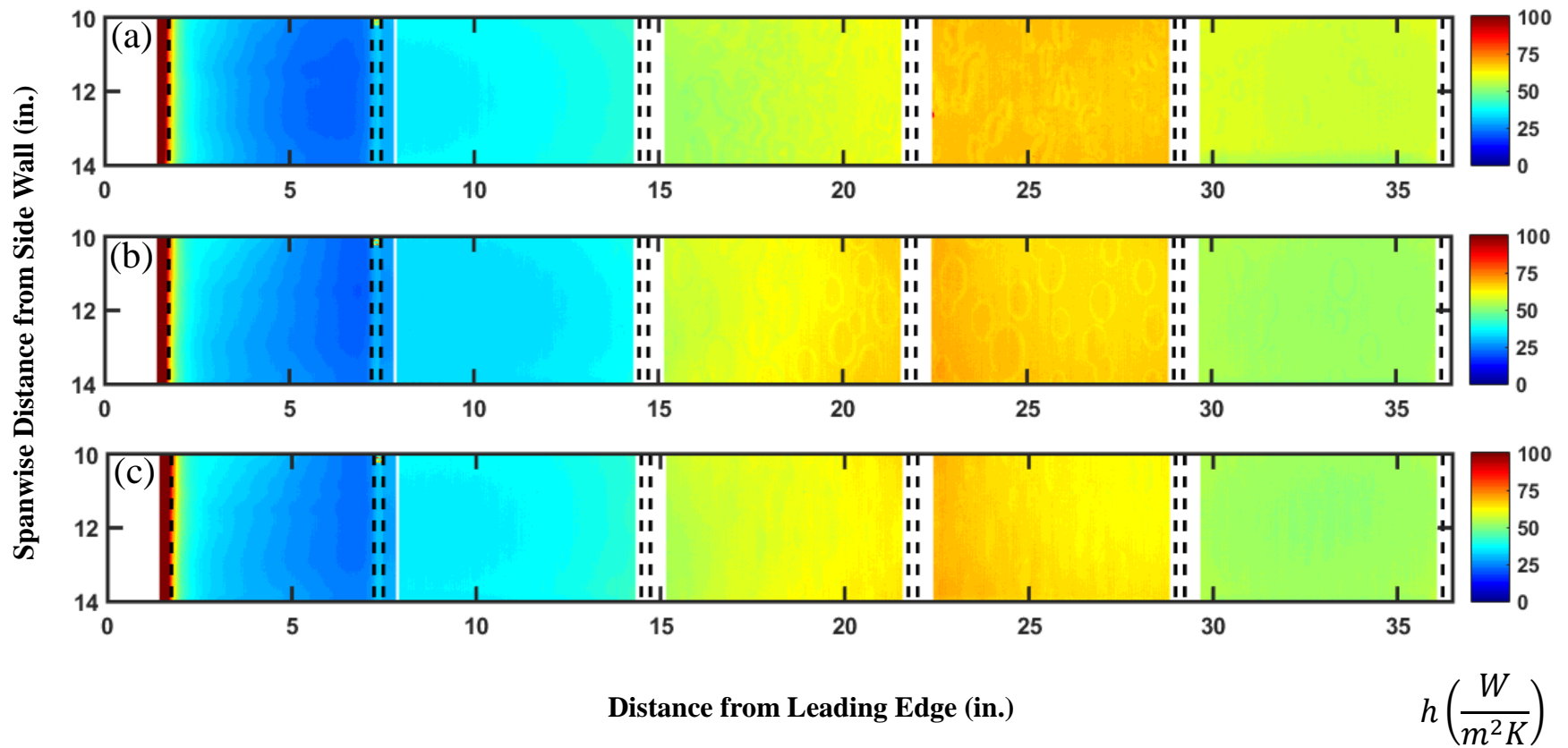


Figure 4.2: Convection coefficient contour maps of aluminum surfaces without ceiling insert for the a) 113012.04 RealIce surface, b) ellipsoid surface, and c) elliptical cone surface

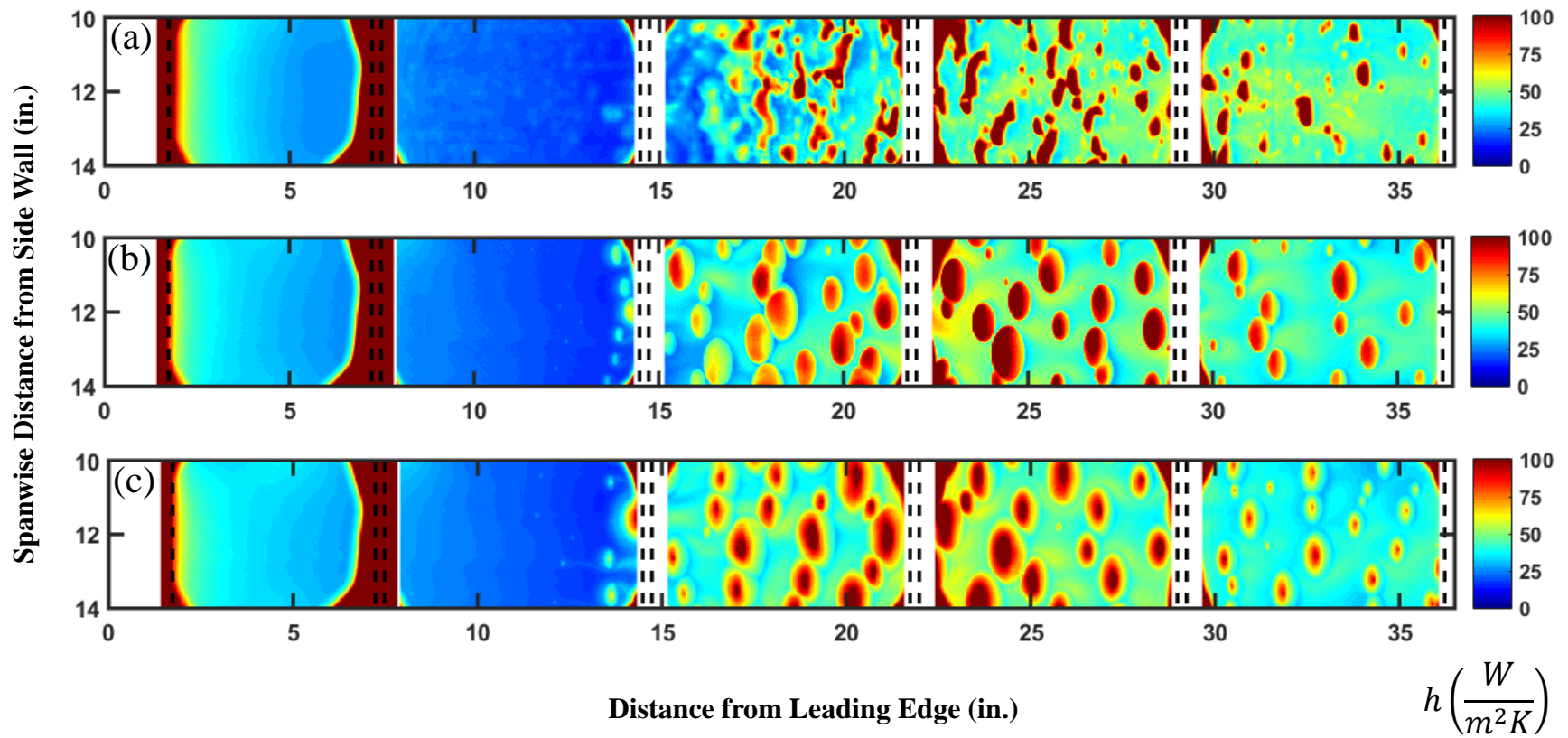


Figure 4.3: Convection coefficient contour maps of plastic surfaces with ceiling insert for the a) 113012.04 RealIce surface, b) ellipsoid surface, and c) elliptical cone surface

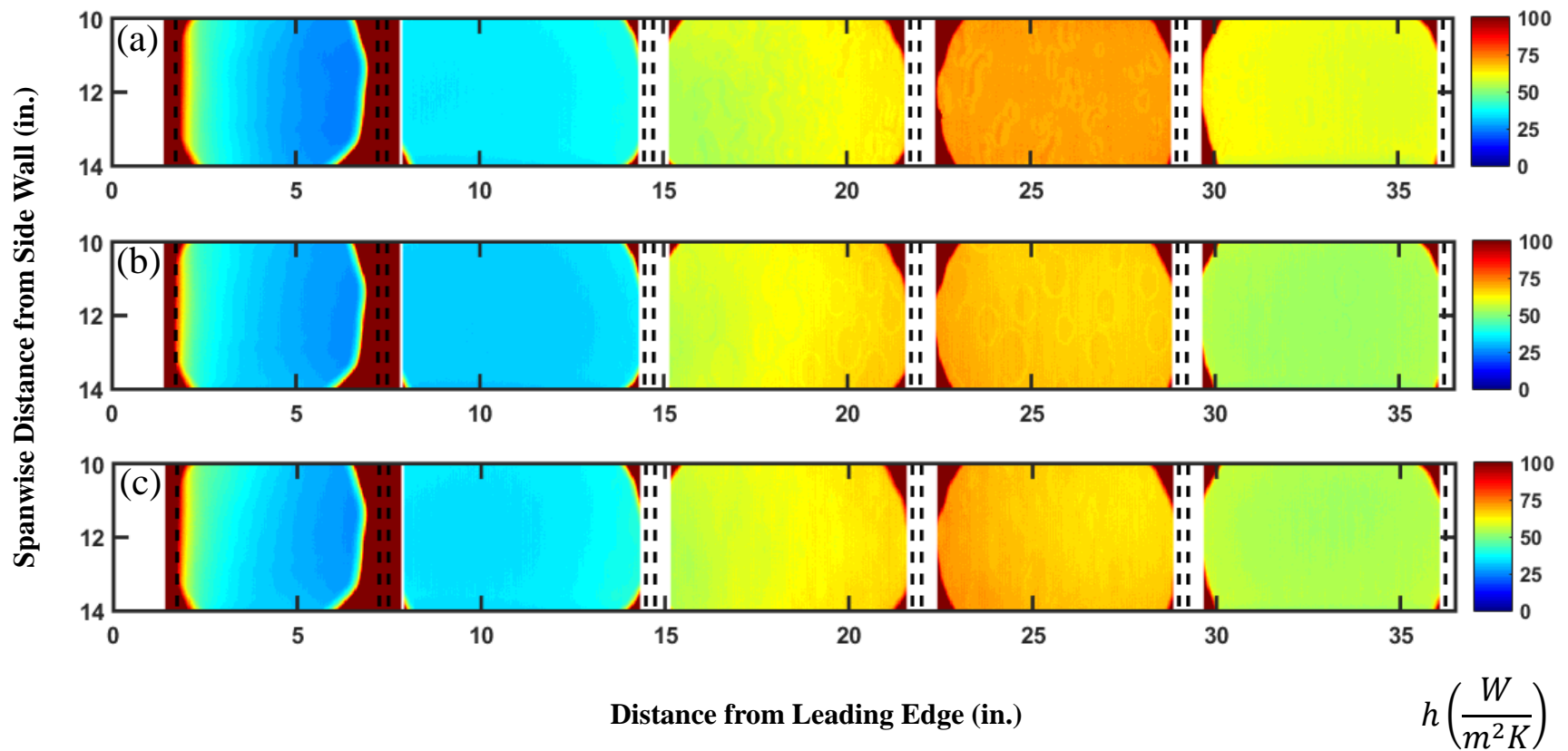


Figure 4.4: Convection coefficient contour maps of aluminum surfaces with ceiling insert for the a) 113012.04 RealIce surface, b) ellipsoid surface, and c) elliptical cone surface

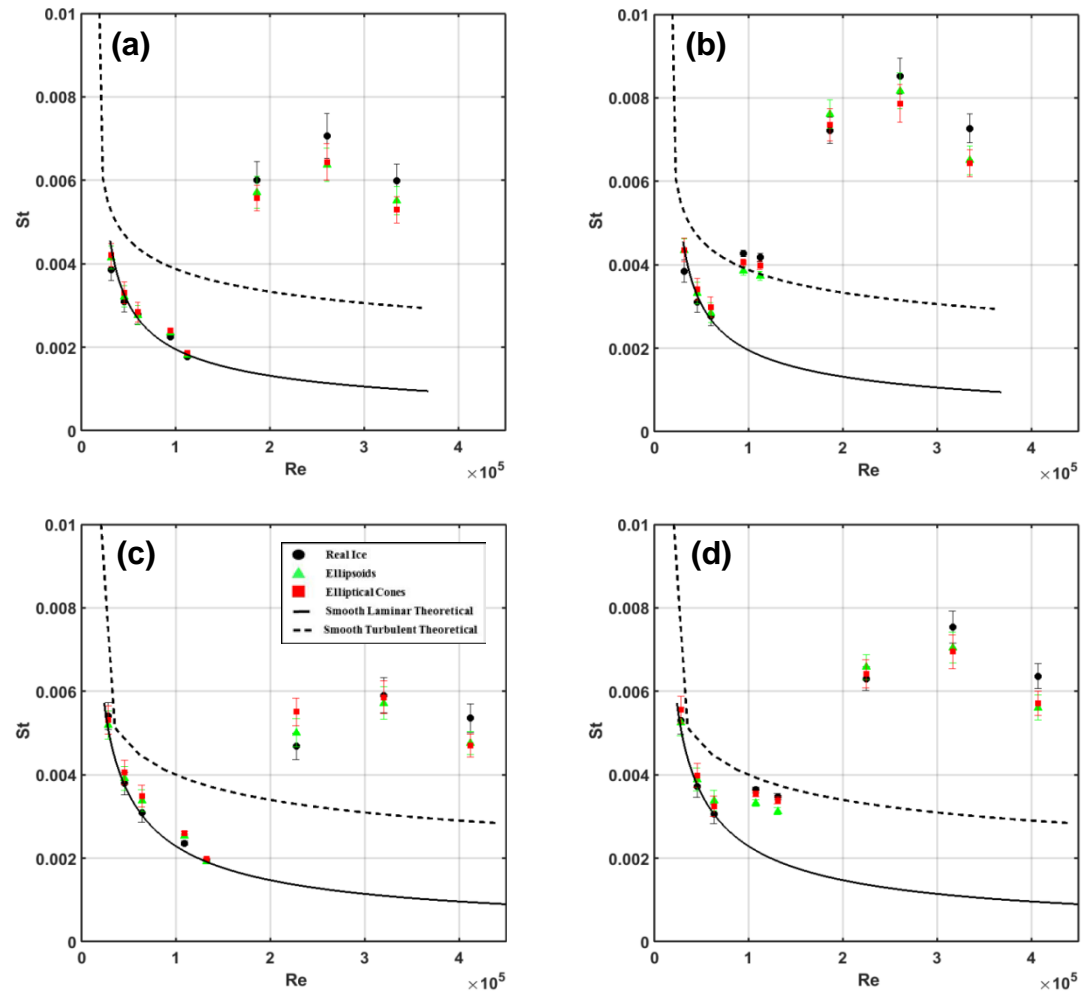


Figure 4.5: Stanton number plots for a) plastic surfaces with negligible acceleration, b) aluminum surfaces with negligible acceleration, c) plastic surfaces with acceleration, and d) aluminum surfaces with acceleration

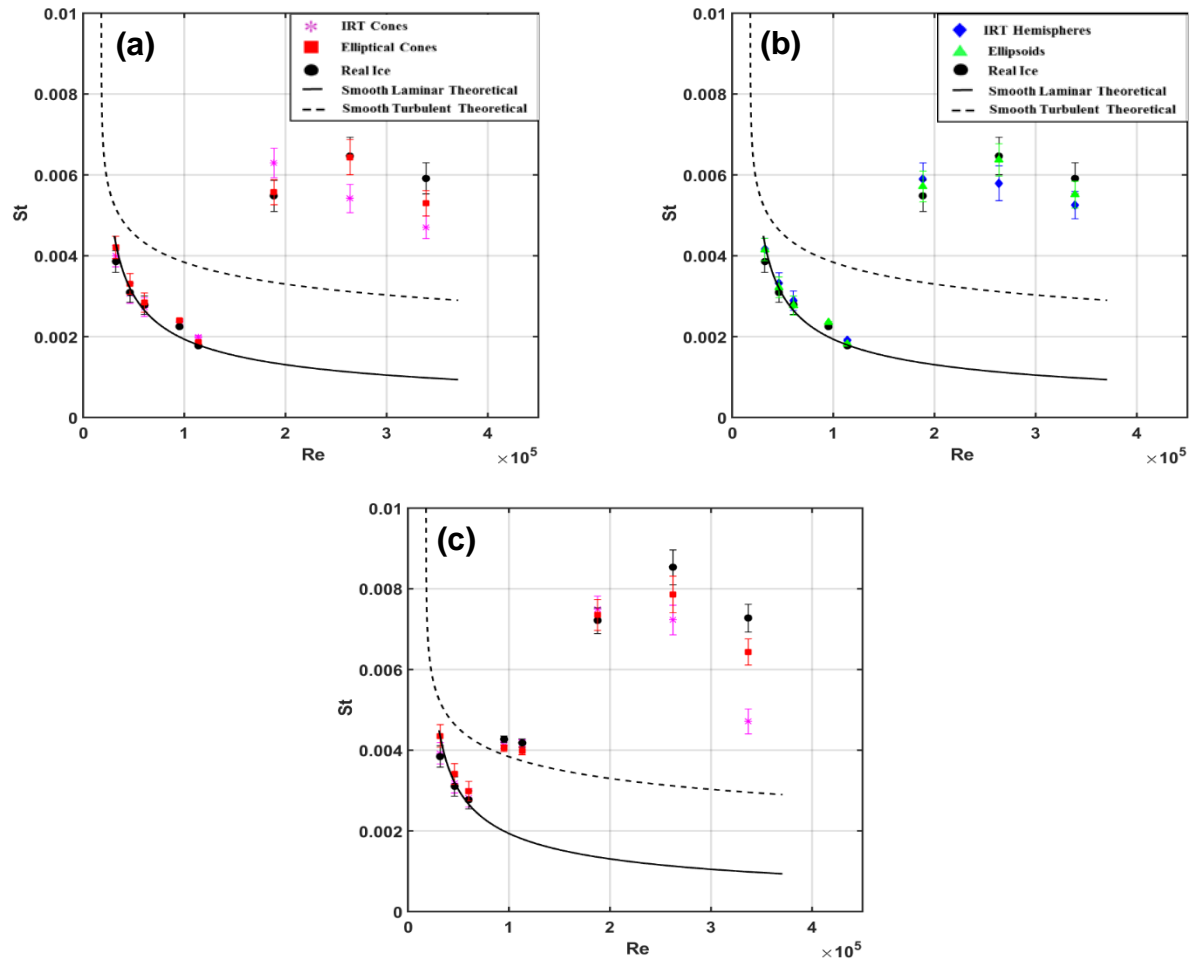


Figure 4.6: Stanton number plots comparing the IRT surfaces, analog surfaces, and the 113012.04 Real Ice surface in flow with negligible acceleration: a) Plastic IRT cones and elliptical cones, b) plastic IRT hemispheres and ellipsoids, and c) aluminum IRT cones and elliptical cones

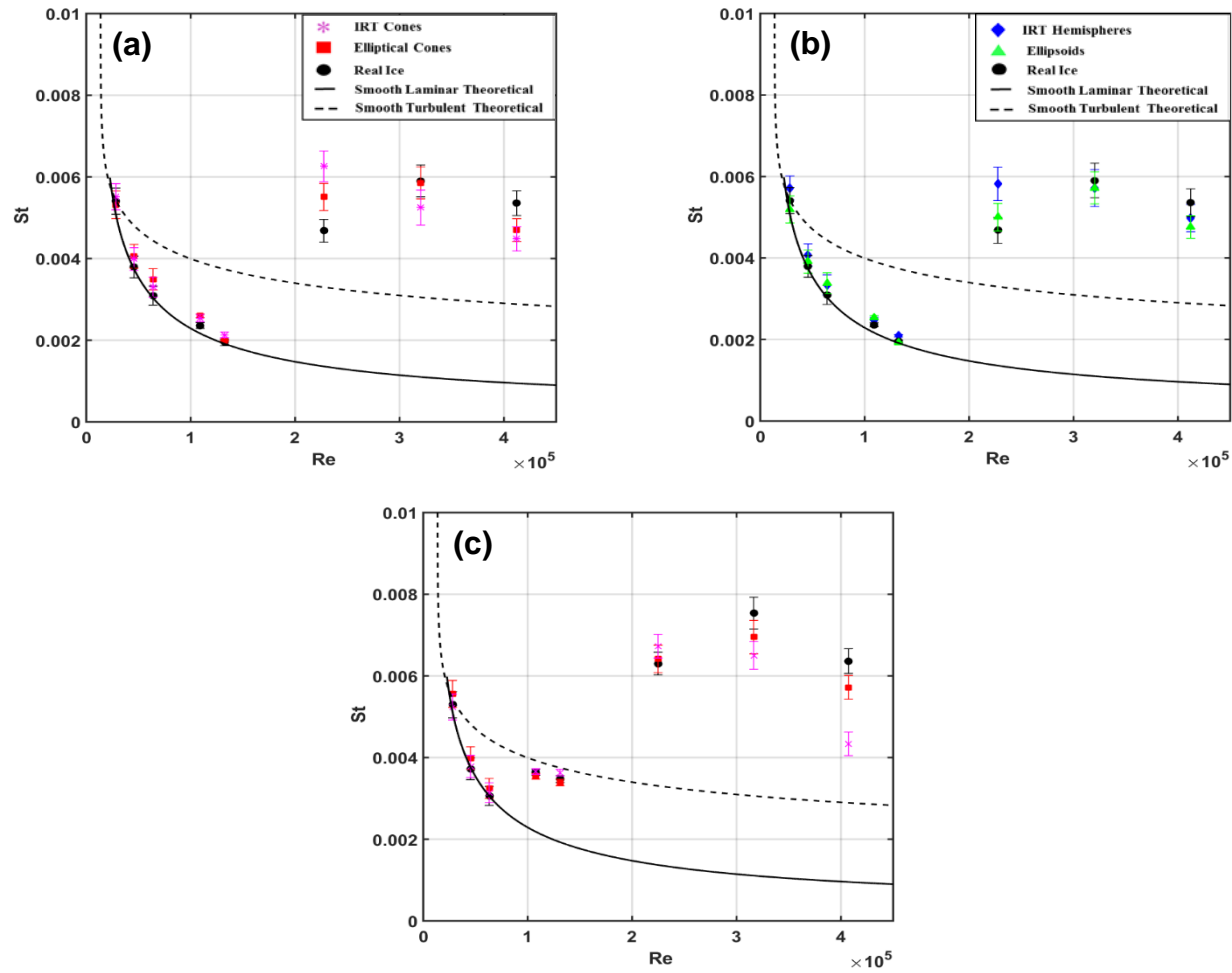


Figure 4.7: Stanton number plots comparing IRT surfaces, analog surfaces, and the 113012.04 Real Ice surface in accelerated flow: a) Plastic IRT cones and elliptical cones, b) plastic IRT hemispheres and ellipsoids, and c) aluminum IRT cones and elliptical cones

Figure 4.5 (a) and (b) display the Stanton number results of the negligible flow acceleration cases over the plastic and aluminum surfaces, respectively. All three surfaces follow the smooth laminar correlation through the second heated section due to minimal or no roughness. Once the flow reaches the roughness elements, it transitions to turbulent flow. The ellipsoid and elliptical cone surfaces agree well for both the plastic and aluminum data. As with the convection contour maps, this shows repeatability in the surface generation process. Regarding the surface matching with the 113012.04 RealIce surface, the ellipsoids and elliptical cones display slightly lower Stanton numbers. However, the analog surfaces can be considered respectable representations of the real ice surface as all of the Stanton numbers are within the uncertainty bands of one another.

The aluminum plate results shown in Figure 4.5 (b) exhibit higher Stanton numbers than the plastic plates. This is expected due to the change in thermal conductivity of the materials. Again, the analog surfaces match each other well from the leading edge to the trailing edge and represent the RealIce surface from heated Sections 0-3. The RealIce surface exhibits a marginally larger Stanton number in Section 4 due to more roughness elements and lateral conduction occurring between those elements.

Figure 4.5 (c) and (d) display the Stanton number results of the accelerated flow cases over the plastic and aluminum surfaces, respectively. Comparing Figures 4.5 (a) and (b) to Figures 4.5 (c) and (d), it can be seen that the accelerated cases generate marginally lower Stanton numbers than those recorded from the negligible flow acceleration tests. The ceiling insert used to accelerate the flow creates a favorable pressure gradient as the roughness increases causing less turbulence near the roughness. Although the convective heat transfer is higher as shown in Figures 4.3 and 4.4, the

increasing velocity in the accelerated cases yield marginally lower Stanton numbers and larger Reynolds numbers.

As with the negligible flow acceleration experiments, the accelerated cases confirm that the two analog surfaces agree well. Inspecting the plastic surface comparison in Figure 4.5 (c), it can be seen that the analog surfaces are within the uncertainty bands of the 113012.04 surface for all heated sections except Section 4. The analog surfaces match the RealIce surface through Section 3 and then decay to a Stanton number lower than that of the RealIce surface in Section 4. The aluminum surface comparison in Figure 4.5 (d) and the negligible acceleration cases in Figure 4.5 (a) and (b) follow the same trend. From this result, it can be inferred that the surface matching program does not accurately replicate the 113012.04 surface near the trailing edge. As stated in Chapter Three, the autocorrelation function used for pattern recognition on the RealIce surface captured an 8" by 8" region approximately 17" downstream of the leading edge. Since the trailing edge is furthest from the center point of the autocorrelation, the characteristics of the RealIce surface were likely not captured downstream of the peak roughness. The analog surfaces do not portray the random nature of small roughness elements scattered in Section 4 of the 113012.04 surface. The autocorrelation also acquired the RMS height of the RealIce roughness in the 8" by 8" region and the analog surfaces matched that region well. However, the decay rate of ice accretion from the peak roughness to the trailing edge is not matched by the analog surfaces at the trailing edge causing slightly lower Stanton numbers.

The results in Figures 4.6 and 4.7 show the comparison of Stanton numbers for the real ice surface studied by Hawkins [8], the analog surfaces created for this

investigation, and IRT surfaces studied by Shannon and McClain [41]. The results are set up in a manner that shows the comparison of the IRT conical surface to the elliptical cones surface and the IRT hemispherical surface to the ellipsoid surface. Figure 4.6 displays the results in flow with negligible acceleration for: a) the plastic conical surfaces and real ice surface, b) the plastic hemispherical surfaces and real ice surface, and c) the aluminum conical surfaces and real ice surface. Figure 4.7 displays the results of the surfaces for the accelerated flow cases in a similar fashion. For the aluminum cases, the only IRT surface created was the cone surface and the last heated section is made of plastic which is why the Stanton number is much lower.

In each case displayed in Figures 4.6 and 4.7, the analog surfaces match the real ice surface better than the IRT surfaces. Also, the analog surfaces display convective heat transfer trends that correspond with the trends found in the real ice surface. The IRT surfaces tend to have higher Stanton numbers in heated Section 3 and lower Stanton numbers in heated Sections 4 and 5, while exhibiting a neatly linear decay. This trend does not match the trend found in the real ice and analog surfaces where the Stanton number reaches a maximum in Section 4.

The analog surfaces investigated in this study use multiple length scales to match the real ice surface, while the IRT surfaces only employ the global streamwise height variation. The length scales matched in the analog surfaces are based on the hypothesis that shed vortices and their interactions with downstream roughness cause increased convective heat transfer. By matching the primary wavelength of the real ice surface, the analog surfaces captured the roughness element spacing that was not captured by the closely packed IRT surfaces.

## *Discussion*

Based on the data presented, the analog surface creation method used in this investigation is a promising method to replicate naturally random rough surfaces with deterministic features. The method proves to be valid for the 113012.04 real ice surface, but must be used to analyze and investigate many other surfaces to be validated. There is opportunity for improvement in the method in the region near the trailing edge of the rough surface as it did not capture the heat transfer values as well as the region of maximum roughness. Also, the method is only applied to an ice accretion formed on a NACA 0012 airfoil. To further validate the method, ice accretions on various airfoils and swept wings should be investigated.

A recent study done by McCarrell [51] investigated three additional real ice surfaces for convective enhancement and velocity boundary layer development using the same techniques used in this study. To aid in validation of the analog surface method, the three remaining surfaces may be matched using analog surfaces and tested for similarities to the real ice surfaces.

Creating analog surfaces to mathematically describe complex roughness has many other applications in engineering research. The method created in this investigation must be employed in other applications to develop the analog roughness database before being deemed acceptable to represent random roughness in any engineering application.

### *Velocity Boundary Layer Results*

Figures 4.8 and 4.9 display the velocity boundary layer measurements at the center of each surface panel in the test section for each surface in this investigation. Figure 4.8 presents the results for the cases with negligible flow acceleration and Figure

4.9 presents the accelerated flow results. The locations where velocity measurements do not begin at the zero y-location are representative of regions where the x-array probe could not reach the test surface due to large roughness elements.

For the cases with negligible acceleration, the boundary layers form as expected. For each surface, the velocity at each plate converges to the test velocity of about 6.7 m/s. In sections such as Section 4 on Figure 4.8 (a) and Section 2 on Figure 4.8 (c), the velocity profile moves vertically before growing. Regions where this phenomena is visible represent locations where the x-array probe was located directly behind a roughness element and did not experience an increase in velocity until vertically traversed above the roughness.

The accelerated cases in Figure 4.9 show similar boundary layer measurements from all three surfaces. The freestream velocities for each surface converge to similar values as expected. At Section 2 in Figure 4.9 (b), there is a decrease in velocity before a normal boundary layer growth begins. This result on the ellipsoid surface is due to the probe being placed behind an ellipsoidal roughness element. The probe is likely experiencing cross flow as the flow accelerates around the ellipsoidal element.

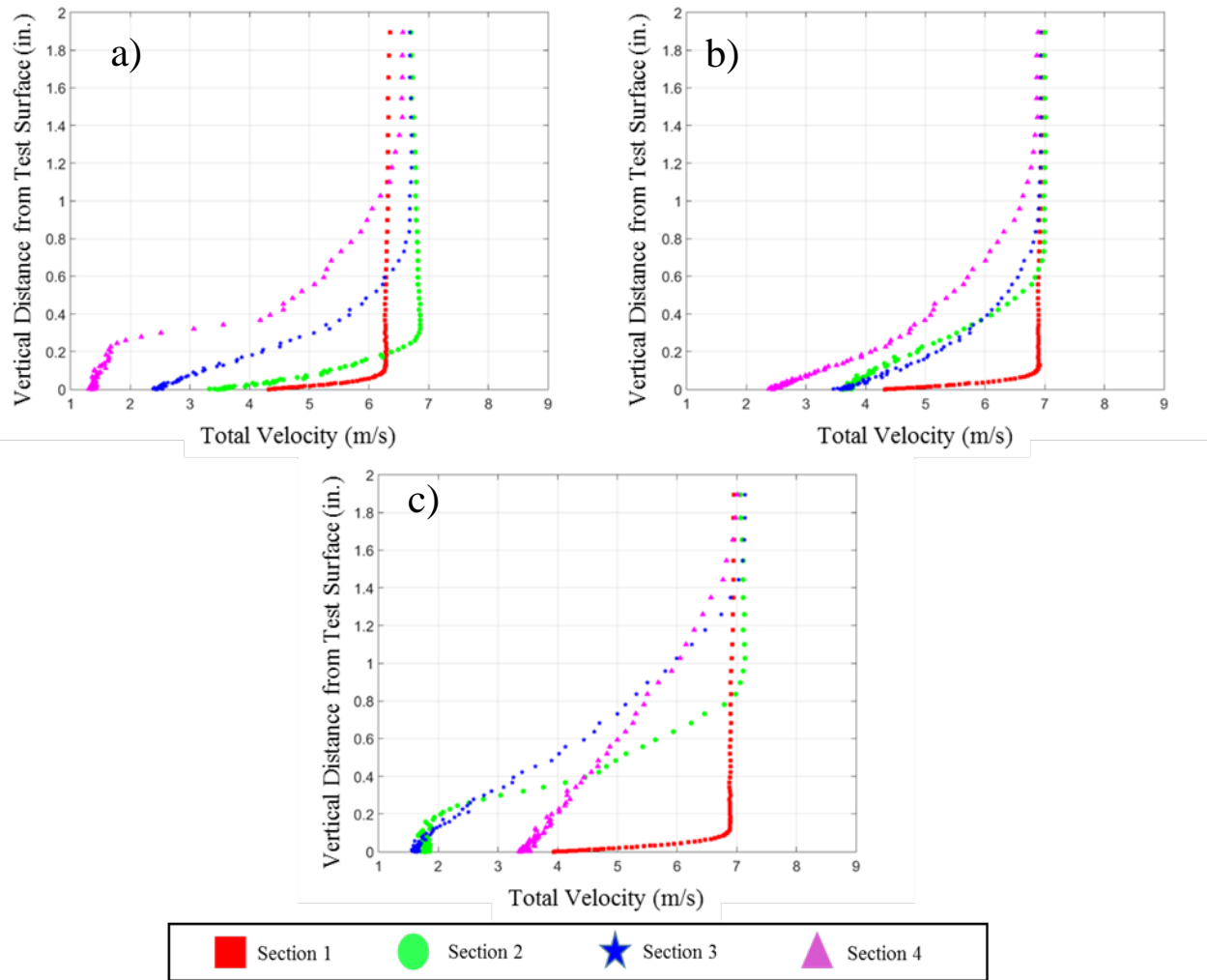


Figure 4.8: Velocity boundary layer traces with negligible acceleration for the a) 113012.04 Real Ice surface, b) ellipsoid surface, and c) elliptical cone surface

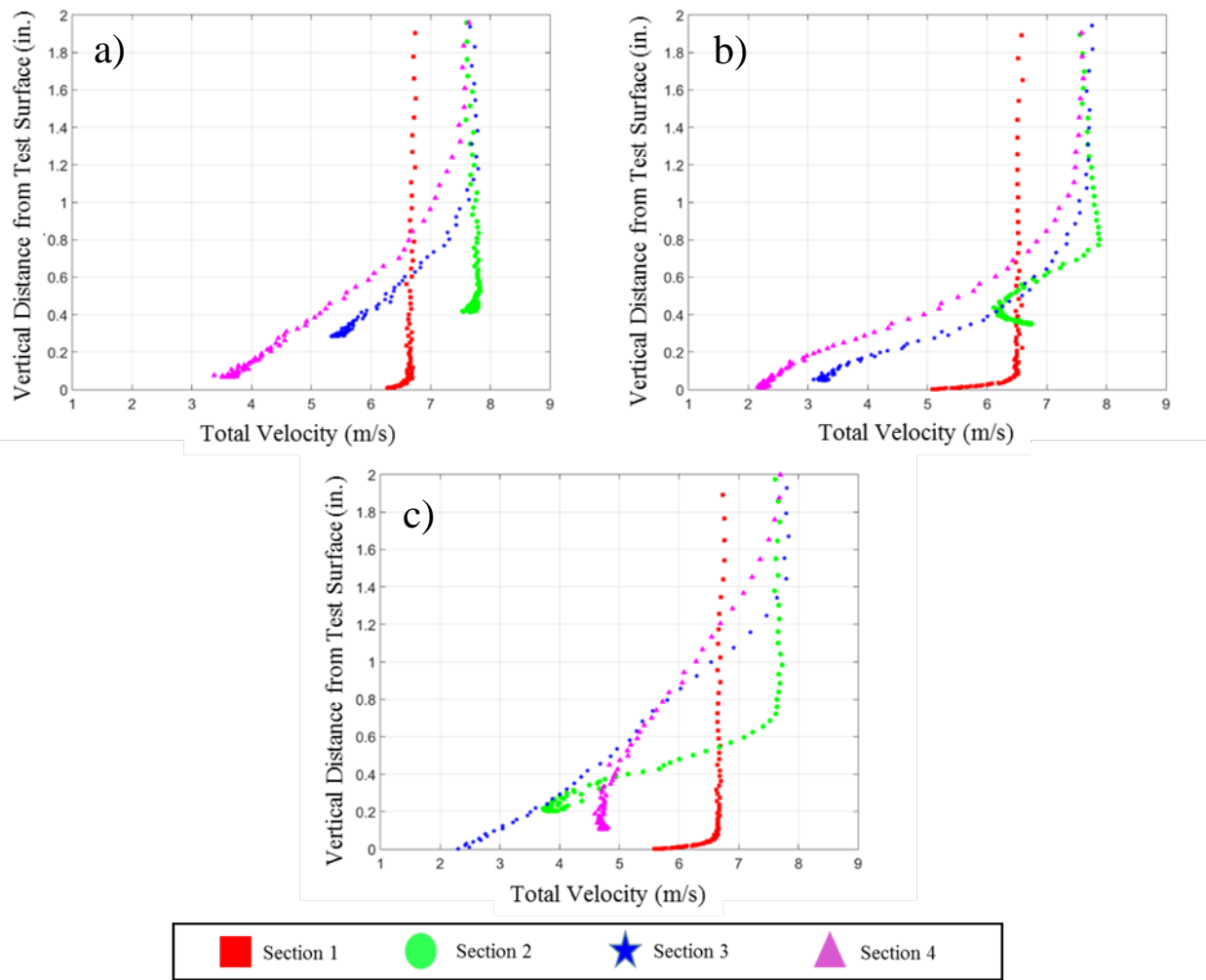


Figure 4.9: Velocity boundary layer traces with acceleration for the a) 113012.04 Surface, b) ellipsoid surface, and c) elliptical cone surface

## CHAPTER FIVE

### Conclusions

#### *Summary of Work*

A new method was created to generate analog roughness surfaces from a laser-scanned real ice roughness surface. The method is based on the hypothesis that the primary convective heat transfer enhancement on ice accretions comes from the interaction of shed vortices with the next downstream roughness elements. The method uses an autocorrelation function to analyze the real ice surface in the region of maximum roughness.

From the autocorrelation, three primary features are retained including the root-mean-square roughness height, the primary wavelength from the maximum roughness to the next downstream roughness elements, and the microscale aspect ratio (eccentricity) of an average roughness elements. The features from the real ice autocorrelation are used to generate analog surfaces that match global, macroscale, and microscale length scales of the real ice surface.

For this study, two analog surfaces, one with ellipsoidal elements and one with elliptical cone elements, were created to match the 113012.04 real ice surface tested by Hawkins. Hawkins investigated the convective heat transfer and boundary layer development on the 113012.04 surface and similar experiments were performed on the two analog surfaces created for this study. The surfaces were created from ABS plastic and aluminum and tested in flows with negligible acceleration and the acceleration

matching that of a NACA 0012 airfoil. The findings from Hawkins investigation were then compared to the results of this investigation.

The primary findings were:

- The new method created to match real ice surfaces with analog surfaces works well in both flows with and without acceleration and for both plastic and aluminum composition. In all convective heat transfer experiments performed, the ellipsoid surface and elliptical cone surface have Stanton numbers within the uncertainty of one another along the entirety of the rough surfaces.
- In comparison with the 113012.04 surface tested by Hawkins, the analog surfaces match the real ice surface well in the region of maximum roughness where the autocorrelation was performed. The only region in which the analog surfaces are not within the uncertainty of the real ice surface is near the trailing edge of the roughness. An explanation for this is that although the root-mean square height is matched, the analog surfaces have slightly fewer roughness elements near the trailing edge and therefore have slightly less Stanton number values.
- The analog surfaces show better agreement with the convective heat transfer results of the real ice surface than the conical and hemispherical IRT surfaces tested by Shannon and McClain [41]. The elliptical cone surface and ellipsoid surface match the real ice surface better than the IRT cones and IRT hemispheres, respectively. The trend of increased convective heat transfer from Section 3 to Section 4 found on the real ice surface was not replicated by the IRT surfaces, but was replicated by both the ellipsoid and elliptical cone surfaces.

### *Future Work*

This investigation is the first use of the analog representation method and applies directly to aircraft ice roughness. To validate the method, future studies must investigate other real ice surfaces and their analogs for similarity. Along with ice accretions formed on a NACA 0012 airfoil, further investigations should be performed on different airfoils and swept wings to provide additional data for validation.

The analog surfaces created for this experiment were tested at velocities to replicate a 21 inch NACA 0012 airfoil. Future research efforts will also attempt to scale flow velocities to replicate a larger airfoil and compare the results of the 113012.04 real ice surface with the analog surfaces created for this investigation.

This method can be used to model surface roughness in many other engineering applications to better understand flow interactions and heat transfer enhancement. Future research efforts can be conducted to apply this method to surface roughness models in areas such as gas turbine blade cooling, ship hull roughness, and conduit roughness. Additional data in these fields must be acquired for the method to be considered acceptable.

## APPENDIX

## APPENDIX A

This appendix provides the test data for the all of the 113012.04 Real Ice, ellipsoids, and elliptical cones convective heat transfer tests.

Table A.1: Un-Accelerated 113012.04 Plastic [8]

Parameter	0a	0b	0c	1a	1b	2	3	4
x (in)	3.10	4.48	5.85	9.23	10.98	18.23	25.48	32.73
A <sub>t</sub> (in <sup>2</sup> )	35.06	35.06	35.06	44.62	44.62	44.62	44.62	44.62
$\varepsilon$	0.95	0.95	0.95	0.95	0.95	0.95	0.95	0.95
$\sigma$ (W/m <sup>2</sup> K <sup>4</sup> )	5.67e-8							
t <sub>p</sub> (in)	0.72	0.72	0.72	0.72	0.72	0.72	0.72	0.72
C <sub>k</sub>	0.90	0.90	0.90	0.90	0.90	1.05	1.10	1.05
E (V)	5.98	5.98	5.98	5.89	5.89	5.86	6.26	6.18
I (A)	2.06	2.06	2.06	2.61	2.61	2.60	2.72	2.55
k <sub>p</sub> (W/mK)	0.205	0.205	0.205	0.205	0.205	0.205	0.205	0.205
T <sub>SS</sub> (K)	316.92	317.24	318.03	320.02	322.27	318.31	316.40	316.26
T <sub>UP</sub> (K)	300.12	300.53	301.23	301.00	300.98	301.50	301.59	301.50
T <sub>∞</sub> (K)	295.45	295.45	295.45	295.45	295.45	295.45	295.45	295.45
T <sub>IR</sub> (K)	305.83	307.92	308.96	309.92	311.40	301.69	302.10	302.52
h (W/m <sup>2</sup> K)	30.37 ± 2.10	24.31 ± 1.88	21.88 ± 1.77	17.67 ± 0.21	13.99 ± 0.20	47.32 ± 3.51	55.67 ± 4.23	47.21 ± 3.09

Table A.2: Un-Accelerated 113012.04 Aluminum [12]

Parameter	0a	0b	0c	1a	1b	2	3	4
x (in)	3.10	4.48	5.85	9.23	10.98	18.23	25.48	32.73
A <sub>t</sub> (in <sup>2</sup> )	35.06	35.06	35.06	44.62	44.62	44.62	44.62	44.62
$\varepsilon$	0.95	0.95	0.95	0.95	0.95	0.95	0.95	0.95
$\sigma$ (W/m <sup>2</sup> K <sup>4</sup> )	5.67E-08							
t <sub>p</sub> (in)	0.72	0.72	0.72	0.72	0.72	0.72	0.72	0.72
C <sub>k</sub>	0.90	0.90	0.90	0.90	0.90	1.05	1.10	1.05
E (V)	6.00	6.00	6.00	5.87	5.87	5.85	6.20	6.09
I (A)	2.06	2.06	2.06	2.65	2.65	2.60	2.75	2.61
k <sub>p</sub> (W/mK)	0.205	0.205	0.205	0.205	0.205	0.205	0.205	0.205
T <sub>SS</sub> (K)	316.84	317.13	317.47	309.97	311.61	307.31	306.95	307.32
T <sub>UP</sub> (K)	300.13	300.51	301.10	299.10	299.05	298.54	298.71	298.77
T <sub>∞</sub> (K)	295.09	295.09	295.09	295.09	295.09	295.09	295.09	295.09
T <sub>IR</sub> (K)	305.64	307.69	308.95	306.05	305.83	301.93	301.88	302.29
h (W/m <sup>2</sup> K)	30.06 ± 2.08	24.23 ± 1.87	21.64 ± 1.74	33.39 ± 0.64	32.64 ± 0.81	56.46 ± 2.50	66.64 ± 3.36	56.81 ± 2.69

Table A.3: Un-Accelerated Ellipsoids Plastic

Parameter	0a	0b	0c	1a	1b	2	3	4
x (in)	3.10	4.48	5.85	9.23	10.98	18.23	25.48	32.73
A <sub>t</sub> (in <sup>2</sup> )	35.06	35.06	35.06	44.62	44.62	44.62	44.62	44.62
$\varepsilon$	0.95	0.95	0.95	0.95	0.95	0.95	0.95	0.95
$\sigma$ (W/m <sup>2</sup> K <sup>4</sup> )	5.67E-08							
t <sub>p</sub> (in)	0.72	0.72	0.72	0.72	0.72	0.72	0.72	0.72
C <sub>k</sub>	0.90	0.90	0.90	0.90	0.90	1.05	1.10	1.05
E (V)	6.13	6.13	6.13	5.95	5.95	5.97	6.47	6.01
I (A)	2.05	2.05	2.05	2.59	2.59	2.59	2.65	2.64
k <sub>p</sub> (W/mK)	0.205	0.205	0.205	0.205	0.205	0.205	0.205	0.205
T <sub>SS</sub> (K)	315.41	315.97	316.96	314.77	317.34	314.96	311.99	313.49
T <sub>UP</sub> (K)	298.79	296.22	297.22	297.85	298.17	298.77	298.85	299.25
T <sub>∞</sub> (K)	293.28	293.28	293.28	293.28	293.28	293.28	293.28	293.28
T <sub>IR</sub> (K)	303.14	304.57	305.75	308.16	310.09	300.48	300.86	301.47
h (W/m <sup>2</sup> K)	33.48 ± 2.21	25.68 ± 2.03	22.69 ± 1.91	18.57 ± 0.17	14.37 ± 0.31	42.56 ± 2.74	51.49 ± 3.26	41.14 ± 2.42

Table A.4: Un-Accelerated Ellipsoids Aluminum

Parameter	0a	0b	0c	1a	1b	2	3	4
x (in)	3.10	4.48	5.85	9.23	10.98	18.23	25.48	32.73
A <sub>t</sub> (in <sup>2</sup> )	35.06	35.06	35.06	44.62	44.62	44.62	44.62	44.62
ε	0.95	0.95	0.95	0.95	0.95	0.95	0.95	0.95
σ (W/m <sup>2</sup> K <sup>4</sup> )	5.67E-08							
t <sub>p</sub> (in)	0.72	0.72	0.72	0.72	0.72	0.72	0.72	0.72
C <sub>k</sub>	0.90	0.90	0.90	0.90	0.90	1.05	1.10	1.05
E (V)	6.14	6.14	6.14	5.94	5.94	5.97	6.43	6.01
I (A)	2.03	2.03	2.03	2.62	2.62	2.57	2.67	2.64
k <sub>p</sub> (W/mK)	0.205	0.205	0.205	0.205	0.205	0.205	0.205	0.205
T <sub>SS</sub> (K)	315.43	315.97	316.71	310.64	312.53	305.73	306.24	309.33
T <sub>UP</sub> (K)	299.50	296.48	297.38	297.21	297.60	297.01	297.26	298.01
T <sub>∞</sub> (K)	293.78	293.78	293.78	293.78	293.78	293.78	293.78	293.78
T <sub>IR</sub> (K)	303.35	304.77	305.95	304.84	304.72	300.27	300.64	301.03
h (W/m <sup>2</sup> K)	35.07 ± 2.26	24.46 ± 2.07	23.42 ± 1.95	30.88 ± 0.76	29.93 ± 0.86	60.89 ± 2.76	65.24 ± 3.44	52.17 ± 2.78

Table A.5: Un-Accelerated Elliptical Cones Plastic

Parameter	0a	0b	0c	1a	1b	2	3	4
x (in)	3.10	4.48	5.85	9.23	10.98	18.23	25.48	32.73
A <sub>t</sub> (in <sup>2</sup> )	35.06	35.06	35.06	44.62	44.62	44.62	44.62	44.62
$\varepsilon$	0.95	0.95	0.95	0.95	0.95	0.95	0.95	0.95
$\sigma$ (W/m <sup>2</sup> K <sup>4</sup> )	5.67E-08							
t <sub>p</sub> (in)	0.72	0.72	0.72	0.72	0.72	0.72	0.72	0.72
C <sub>k</sub>	0.90	0.90	0.90	0.90	0.90	1.05	1.10	1.05
E (V)	6.14	6.14	6.14	5.97	5.97	5.99	6.39	6.01
I (A)	2.05	2.05	2.05	2.60	2.60	2.56	2.68	2.64
k <sub>p</sub> (W/mK)	0.205	0.205	0.205	0.205	0.205	0.205	0.205	0.205
T <sub>SS</sub> (K)	315.92	316.41	317.28	316.05	319.14	312.16	313.21	313.21
T <sub>UP</sub> (K)	298.85	296.31	297.27	297.91	298.59	298.57	299.19	299.08
T <sub>∞</sub> (K)	293.45	293.45	293.45	293.45	293.45	293.45	293.45	293.45
T <sub>IR</sub> (K)	303.05	304.35	305.51	307.61	309.43	299.94	301.43	302.00
h (W/m <sup>2</sup> K)	34.09 ± 2.22	26.50 ± 2.06	23.46 ± 1.94	19.14 ± 0.23	14.75 ± 0.23	51.35 ± 3.08	46.77 ± 2.96	39.06 ± 2.25

Table A.6: Un-Accelerated Elliptical Cones Aluminum

Parameter	0a	0b	0c	1a	1b	2	3	4
x (in)	3.10	4.48	5.85	9.23	10.98	18.23	25.48	32.73
A <sub>t</sub> (in <sup>2</sup> )	35.06	35.06	35.06	44.62	44.62	44.62	44.62	44.62
$\varepsilon$	0.95	0.95	0.95	0.95	0.95	0.95	0.95	0.95
$\sigma$ (W/m <sup>2</sup> K <sup>4</sup> )	5.67E-08							
t <sub>p</sub> (in)	0.72	0.72	0.72	0.72	0.72	0.72	0.72	0.72
C <sub>k</sub>	0.90	0.90	0.90	0.90	0.90	1.05	1.10	1.05
E (V)	6.21	6.21	6.21	5.94	5.94	5.98	6.55	6.01
I (A)	2.03	2.03	2.03	2.59	2.59	2.56	2.62	2.64
k <sub>p</sub> (W/mK)	0.205	0.205	0.205	0.205	0.205	0.205	0.205	0.205
T <sub>SS</sub> (K)	312.71	312.91	313.69	305.92	307.36	305.88	305.54	305.81
T <sub>UP</sub> (K)	296.69	293.82	294.74	294.27	294.58	294.96	295.10	295.32
T <sub>∞</sub> (K)	291.28	291.28	291.28	291.28	291.28	291.28	291.28	291.28
T <sub>IR</sub> (K)	300.95	302.33	303.39	302.17	302.01	297.51	298.06	298.72
h (W/m <sup>2</sup> K)	35.40 ± 2.28	27.46 ± 2.09	24.65 ± 1.98	32.77 ± 0.69	32.27 ± 0.80	59.34 ± 3.10	63.50 ± 3.66	52.02 ± 2.62

Table A.7: Accelerated 113012.04 Plastic [8]

Parameter	0a	0b	0c	1a	1b	2	3	4
x (in)	3.10	4.48	5.85	9.23	10.98	18.23	25.48	32.73
A <sub>t</sub> (in <sup>2</sup> )	35.06	35.06	35.06	44.62	44.62	44.62	44.62	44.62
$\varepsilon$	0.95	0.95	0.95	0.95	0.95	0.95	0.95	0.95
$\sigma$ (W/m <sup>2</sup> K <sup>4</sup> )	5.67E-08							
t <sub>p</sub> (in)	0.72	0.72	0.72	0.72	0.72	0.72	0.72	0.72
C <sub>k</sub>	0.90	0.90	0.90	0.90	0.90	1.05	1.10	1.05
E (V)	6.00	6.00	6.00	5.87	5.87	5.88	6.27	6.14
I (A)	2.09	2.09	2.09	2.63	2.63	2.59	2.72	2.57
k <sub>p</sub> (W/mK)	0.205	0.205	0.205	0.205	0.205	0.205	0.205	0.205
T <sub>SS</sub> (K)	314.31	315.30	316.45	317.92	320.03	317.41	315.09	314.67
T <sub>UP</sub> (K)	297.53	298.31	298.91	299.71	300.23	301.10	300.98	300.83
T <sub>∞</sub> (K)	295.32	295.32	295.32	295.32	295.32	295.32	295.32	295.32
T <sub>IR</sub> (K)	304.30	306.28	307.40	308.47	309.61	301.73	301.90	301.81
h (W/m <sup>2</sup> K)	37.04 ± 2.20	29.05 ± 2.03	25.33 ± 1.91	20.92 ± 0.45	17.62 ± 0.28	46.91 ± 3.34	57.77 ± 4.25	53.54 ± 3.51

Table A.8: Accelerated 113012.04 Aluminum [8]

Parameter	0a	0b	0c	1a	1b	2	3	4
x (in)	3.10	4.48	5.85	9.23	10.98	18.23	25.48	32.73
A <sub>t</sub> (in <sup>2</sup> )	35.06	35.06	35.06	44.62	44.62	44.62	44.62	44.62
$\varepsilon$	0.95	0.95	0.95	0.95	0.95	0.95	0.95	0.95
$\sigma$ (W/m <sup>2</sup> K <sup>4</sup> )	5.67E-08							
t <sub>p</sub> (in)	0.72	0.72	0.72	0.72	0.72	0.72	0.72	0.72
C <sub>k</sub>	0.90	0.90	0.90	0.90	0.90	1.05	1.10	1.05
E (V)	6.00	6.00	6.00	5.87	5.87	5.87	6.19	6.05
I (A)	2.07	2.07	2.07	2.64	2.64	2.61	2.75	2.60
k <sub>p</sub> (W/mK)	0.205	0.205	0.205	0.205	0.205	0.205	0.205	0.205
T <sub>SS</sub> (K)	314.70	315.69	316.23	310.44	311.91	307.47	307.01	307.37
T <sub>UP</sub> (K)	297.71	298.56	299.15	298.92	299.05	298.78	298.94	299.11
T <sub>∞</sub> (K)	295.47	295.47	295.47	295.47	295.47	295.47	295.47	295.47
T <sub>IR</sub> (K)	304.48	306.44	307.67	306.61	306.50	302.15	301.92	302.35
h (W/m <sup>2</sup> K)	36.04 ± 2.18	28.37 ± 2.03	24.90 ± 1.90	32.05 ± 0.64	31.22 ± 0.75	58.69 ± 2.61	70.56 ± 3.65	59.68 ± 2.84

Table A.9: Accelerated Ellipsoids Plastic

Parameter	0a	0b	0c	1a	1b	2	3	4
x (in)	3.10	4.48	5.85	9.23	10.98	18.23	25.48	32.73
A <sub>t</sub> (in <sup>2</sup> )	35.06	35.06	35.06	44.62	44.62	44.62	44.62	44.62
$\varepsilon$	0.95	0.95	0.95	0.95	0.95	0.95	0.95	0.95
$\sigma$ (W/m <sup>2</sup> K <sup>4</sup> )	5.67E-08							
t <sub>p</sub> (in)	0.72	0.72	0.72	0.72	0.72	0.72	0.72	0.72
C <sub>k</sub>	0.90	0.90	0.90	0.90	0.90	1.05	1.10	1.05
E (V)	6.26	6.26	6.26	5.92	5.92	5.95	6.50	6.01
I (A)	2.04	2.04	2.04	2.59	2.59	2.58	2.66	2.64
k <sub>p</sub> (W/mK)	0.205	0.205	0.205	0.205	0.205	0.205	0.205	0.205
T <sub>SS</sub> (K)	314.88	316.09	316.19	314.35	317.46	314.87	313.18	313.02
T <sub>UP</sub> (K)	296.12	297.10	297.74	298.09	298.29	298.91	299.19	299.53
T <sub>∞</sub> (K)	293.36	293.36	293.36	293.36	293.36	293.36	293.36	293.36
T <sub>IR</sub> (K)	302.42	303.78	304.64	306.31	307.91	299.94	300.52	301.11
h (W/m <sup>2</sup> K)	35.59 ± 2.28	29.98 ± 2.17	27.71 ± 2.09	22.57 ± 0.41	17.39 ± 0.17	46.81 ± 3.16	53.94 ± 3.67	44.96 ± 2.61

Table A10: Accelerated Ellipsoids Aluminum

Parameter	0a	0b	0c	1a	1b	2	3	4
x (in)	3.10	4.48	5.85	9.23	10.98	18.23	25.48	32.73
A <sub>t</sub> (in <sup>2</sup> )	35.06	35.06	35.06	44.62	44.62	44.62	44.62	44.62
$\epsilon$	0.95	0.95	0.95	0.95	0.95	0.95	0.95	0.95
$\sigma$ (W/m <sup>2</sup> K <sup>4</sup> )	5.67E-08							
t <sub>p</sub> (in)	0.72	0.72	0.72	0.72	0.72	0.72	0.72	0.72
C <sub>k</sub>	0.90	0.90	0.90	0.90	0.90	1.05	1.10	1.05
E (V)	6.20	6.20	6.20	5.89	5.89	5.94	6.36	6.01
I (A)	2.07	2.07	2.07	2.61	2.61	2.59	2.70	2.64
k <sub>p</sub> (W/mK)	0.205	0.205	0.205	0.205	0.205	0.205	0.205	0.205
T <sub>SS</sub> (K)	314.56	315.88	315.78	310.66	312.43	306.10	305.99	309.38
T <sub>UP</sub> (K)	296.14	296.92	297.41	297.12	297.50	297.03	297.21	297.96
T <sub>∞</sub> (K)	293.41	293.41	293.41	293.41	293.41	293.41	293.41	293.41
T <sub>IR</sub> (K)	302.72	304.10	305.08	304.73	304.70	299.80	300.22	300.57
h (W/m <sup>2</sup> K)	35.40 ± 2.22	29.55 ± 2.11	27.05 ± 2.02	29.25 ± 0.69	28.09 ± 0.75	61.33 ± 2.84	66.14 ± 3.44	52.61 ± 2.82

Table A.11: Accelerated Elliptical Cones Plastic

Parameter	0a	0b	0c	1a	1b	2	3	4
x (in)	3.10	4.48	5.85	9.23	10.98	18.23	25.48	32.73
A <sub>t</sub> (in <sup>2</sup> )	35.06	35.06	35.06	44.62	44.62	44.62	44.62	44.62
$\varepsilon$	0.95	0.95	0.95	0.95	0.95	0.95	0.95	0.95
$\sigma$ (W/m <sup>2</sup> K <sup>4</sup> )	5.67E-08							
t <sub>p</sub> (in)	0.72	0.72	0.72	0.72	0.72	0.72	0.72	0.72
C <sub>k</sub>	0.90	0.90	0.90	0.90	0.90	1.05	1.10	1.05
E (V)	6.32	6.32	6.32	5.95	5.95	6.02	6.67	6.01
I (A)	2.03	2.03	2.03	2.57	2.57	2.55	2.60	2.64
k <sub>p</sub> (W/mK)	0.205	0.205	0.205	0.205	0.205	0.205	0.205	0.205
T <sub>SS</sub> (K)	313.87	314.53	314.69	312.82	315.75	311.05	311.95	312.48
T <sub>UP</sub> (K)	295.35	296.16	296.72	296.96	297.37	297.74	298.27	298.51
T <sub>∞</sub> (K)	292.68	292.68	292.68	292.68	292.68	292.68	292.68	292.68
T <sub>IR</sub> (K)	301.65	302.80	303.56	305.56	307.21	298.97	300.11	300.91
h (W/m <sup>2</sup> K)	36.88 ± 2.32	32.15 ± 2.24	29.86 ± 2.16	23.17 ± 0.41	18.07 ± 0.14	54.19 ± 3.28	52.97 ± 3.44	41.43 ± 2.39

Table A12: Accelerated Elliptical Cones Aluminum

Parameter	0a	0b	0c	1a	1b	2	3	4
x (in)	3.10	4.48	5.85	9.23	10.98	18.23	25.48	32.73
A <sub>t</sub> (in <sup>2</sup> )	35.06	35.06	35.06	44.62	44.62	44.62	44.62	44.62
$\varepsilon$	0.95	0.95	0.95	0.95	0.95	0.95	0.95	0.95
$\sigma$ (W/m <sup>2</sup> K <sup>4</sup> )	5.67E-08							
t <sub>p</sub> (in)	0.72	0.72	0.72	0.72	0.72	0.72	0.72	0.72
C <sub>k</sub>	0.90	0.90	0.90	0.90	0.90	1.05	1.10	1.05
E (V)	6.23	6.23	6.23	5.93	5.93	5.97	6.56	6.01
I (A)	2.06	2.06	2.06	2.59	2.59	2.56	2.63	2.64
k <sub>p</sub> (W/mK)	0.205	0.205	0.205	0.205	0.205	0.205	0.205	0.205
T <sub>SS</sub> (K)	310.33	312.16	313.06	305.38	306.89	305.15	304.74	304.92
T <sub>UP</sub> (K)	293.06	293.81	294.28	293.60	293.97	294.24	294.35	294.51
T <sub>∞</sub> (K)	290.48	290.48	290.48	290.48	290.48	290.48	290.48	290.48
T <sub>IR</sub> (K)	299.36	300.92	302.08	301.55	301.46	296.54	296.99	297.57
h (W/m <sup>2</sup> K)	38.59 ± 2.28	30.93 ± 2.15	26.90 ± 2.03	31.80 ± 0.64	31.05 ± 0.73	60.79 ± 3.21	66.33 ± 3.90	54.69 ± 2.78

## REFERENCES

- [1] Nikuradse, J., 1933, "Laws for Flows in Rough Pipes," *VDI-Forschungsheft*, **4**, pp. 361.
- [2] Schlichting, H., 1936, "Experimental Investigation of the Problem of Surface Roughness," TM-832, National Advisory Committee on Aeronautics.
- [3] Tecson, L., 2013, "Convective Heat Transfer from Realistic Ice Roughness Distributions," MS thesis, Department of Mechanical Engineering, Baylor University.
- [4] Walker, C. W., 2014, "Convection from Manufactured Ice Roughness with Varying Flux Boundary Conditions," MS thesis, Department of Mechanical Engineering, Baylor University.
- [5] McClain, S.T., Reed, D., Vargas, M., Kreeger, R.E., and Tsao, J.-C., 2014, "Ice roughness in Short Duration SLD Icing Events," 6th AIAA Atmospheric and Space Environments Conference, 16-20 June, Atlanta, GA, AIAA-2014-2330.
- [6] McClain, S.T. and Kreeger, R.E., (2013), "Assessment of Ice Shape Roughness Using a Self-Organizing Map Approach," Presented at the 5th AIAA Atmospheric and Space Environments Conference, June 24-27, 2013, San Diego, CA, AIAA-2013-2546.
- [7] Shannon, T. A., 2015, "Convection from Realistic Ice Roughness on a Simulated NACA 0012 Airfoil," MS thesis, Department of Mechanical Engineering, Baylor University.
- [8] Hawkins, D.M., 2016, "Convection from Laser-Scanned Real Ice Roughness on a Simulated NACA 0012 Airfoil," MS thesis, Department of Mechanical Engineering, Baylor University.
- [9] Hama, F. R., 1954, "Boundary Layer Characteristics for Smooth and Rough Surfaces," *Naval Architects Marine Engineers*, Trans 62.
- [10] Clauser, F., 1956, "The Turbulent Boundary Layer," *Advances in Applied Mechanics*, Vol 4.
- [11] Rotta, J., 1950, "Über die Theorie der turbulenten Grenzschichten," *Mitteilungen MPI Stromungs Forschung*, Vol. 1.

- [12] Dvorak, F. A., 1969, "Calculation of Turbulent Boundary Layers on Rough Surfaces in Pressure Gradients," *AIAA Journal*, Vol. 7, pp. 1752-1759.
- [13] Betterman, D., 1969, "Contribution a l'Etude de la Convection Force Turbulente le Long de Plaques Plaques Rugueuses," *AIAA Journal*, Vol. 9, pp. 153 – 164
- [14] Simpson R. L., 1973, "A Generalized Correlation of Roughness Density Effects on the Turbulent Boundary Layer," *AIAA Journal*, Vol. 11, pp. 242-244
- [15] Dirling, R. B., 1973, "A Method for Computing Rough Wall Heat Transfer Rates on Reentry Nose Tips," AIAA Paper No. 73-763.
- [16] Coleman, H. W., Moffat, R. J., and Kays, W. M., 1981, "Heat Transfer in the Accelerated Fully Rough Turbulent Boundary Layer," *Journal of Heat Transfer*, Vol. 103, No. 1, pp. 153-158.
- [16] Chakroun, W., and Taylor, R. P., 1993, "The Effects of Moderately Strong Acceleration on Heat Transfer in the Turbulent Rough-Wall Boundary Layer," *Journal of Heat Transfer*, Vol. 115, No. 3, pp. 1187-1201.
- [17] Sigal, A. and Danberg, J. E., (1990), "New Correlation of Roughness Density Effect on the Turbulent Boundary Layer," *AIAA Journal*, Vol. 28, No. 3, pp. 554-556.
- [18] Bons, J.P., 2002, "St and Cf Augmentation for Real Turbine Roughness with Elevated Freestream Turbulence," *Journal of Turbomachinery*, **124**, pp. 632-644
- [19] McClain, S.T., Reed, D., Vargas, M., Kreeger, R.E., and Tsao, J.C., 2014, "Ice Roughness in Short Duration SLD Icing Events," 6<sup>th</sup> AIAA Atmospheric and Space Environments Conference, 16-20 June, Atlanta, GA, AIAA-2014-2330.
- [20] McClain, S.T., Vargas, M., Kreeger, R.E., and Tsao, J., 2015, "A Reevaluation of Appendix C Ice Roughness Using Laser Scanning," SAE Technical Paper 2015-01-2098, 2015, doi:10.4271/2015-01-2097.
- [21] McClain, S.T., and Kreeger, R.E., 2013, "Assessment of Ice Shape Roughness Using a Self-Organizing Map Approach," 5<sup>th</sup> AIAA Atmospheric and Space Environments Conference, 24-27 June, San Diego, CA, AIAA-2013-2546
- [22] Bons, J. P., and McClain, S. T., 2004, "The Effect of Real Turbine Roughness with Pressure Gradient on Heat Transfer," *Journal of Turbomachinery*, Vol. 126, No. 3, pg 385-394.
- [23] "What is Surface Roughness?," *Introduction To Roughness, KEYENCE America* Available: <https://www.keyence.com/ss/products/microscope/roughness/line/index.jsp>.

- [24] Flack, K. A., Schultz, M. P., 2010, "Review of Hydraulic Roughness Scales in the Fully Rough Regime," *Journal of Fluids Engineering*, Vol. 132, No. 041203, pg. 1-10.
- [25] Munson, B.R., Okiishi, T.H., Huebsch, W.W., and Rothmayer, A.P., 2013, *Fundamentals of Fluid Mechanics*, 7th ed., John Wiley & Sons, Inc., Hoboken, NJ, pp. 482.
- [26] White, F. M., 2006, *Viscous Fluid Flow*, 3rd Ed, Boston, McGraw-Hill, Inc., New York, NY.
- [27] Moran, M. J., and Shapiro, H. N., 2008, *Fundamentals of Engineering Thermodynamics*, 6th ed., John Wiley & Sons, Inc., Hoboken, NJ.
- [28] Bejan, A., 2004, *Convection Heat Transfer*, 3rd ed., John Wiley & Sons, Inc., Hoboken, NJ.
- [29] "Compliance of Transport Category Airplanes with Certification Requirements for Flight in Icing Conditions," 2014, AC No: 25-28.
- [30] "14 CFR Part 25: Airworthiness Standards: Transport Category Airplanes - Appendix C, Part I: Atmospheric Icing Conditions," 2012, *Code of Federal Regulations*.
- [31] "14 CFR Part 25: Airworthiness Standards: Transport Category Airplanes - Appendix O, Part I: Meteorology," 2014, *Code of Federal Regulations*.
- [32] Barbagallo, J., 2015, Deputy Director, Flight Standards Service, "Pilot Guide: Flight in Icing Conditions," Advisory Circular, U.S. Department of Transportation, AC No: 91-74B.
- [33] Olsen, W., Walker, E., 1986, "Experimental Evidence for Modifying the Current Physical Model for Ice Accretion on Aircraft Surfaces," NASA TM-87184.
- [34] Anderson, D. N., and Shin, J., 1997, "Characterization of Ice Roughness from Simulated Icing Encounters," NASA TM-107400.
- [35] Messinger, B.L., 1953, "Equilibrium Temperature of an Unheated Icing Surface as a Function of Air Speed," *Journal of Aeronautical Sciences*, pp. 29-42.
- [36] Wright, W.B., 2002, "User Manual for the NASA Glenn Ice Accretion Code LEWICE," NASA/CR-2002-211793.
- [37] Shin, J., 1994, "Characteristics of Surface Roughness Associated With Leading Edge Ice Accretion," NASA TM-106459.

- [38] Croce, G., De Candido, E., Habashi, W. G., Munzar, J., Aubé M. S., Baruzzi, G. S., and Aliaga, C., 2010, “FENSAP-ICE: Analytical Model for Spatial and Temporal Evolution of In-Flight Icing Roughness,” *Journal of Aircraft*, **47**(4), pp. 1283-1289.
- [39] Tecson, L. and McClain, S.T., (2013), “Modeling of Realistic Ice Roughness Element Distributions to Characterize Convective Heat Transfer,” 5th AIAA Atmospheric and Space Environments Conference, 24-27 June, San Diego, CA, AIAA-2013-3059.
- [40] Walker C. W., McClain S. T., and Shannon T. A., (2014), “Convection from Ice Roughness with Varying Flux Boundary Conditions,” 6th AIAA Atmospheric and Space Environments Conference, 16-20 June, Atlanta, GA, AIAA-2014-2463.
- [41] Shannon, T. A., and McClain, S. T., 2016, “Convection from a Simulated NACA 0012 with Icing Roughness of Different Shape and Thermal Conductivity,” 8th AIAA Atmospheric and Space Environments Conference, 13-17 June, Washington, DC, AIAA-2016-3588.
- [42] McClain, S. T., Tiño, P., and Kreeger, R. E., 2011, “Ice Shape Characterization Using Self-Organizing Maps,” *Journal of Aircraft*, **48**(2), pp. 724-729.
- [43] McClain, S.T. and Kreeger, R.E., 2013, “Assessment of Ice Shape Roughness Using a Self-Organizing Map Approach,” Presented at the 5th AIAA Atmospheric and Space Environments Conference, June 24-27, 2013, San Diego, CA, AIAA-2013-2546.
- [44] McClain, S. T., 2016, “Manual Point Cloud Registration for Combined Ice Roughness and Ice Thickness Measurements,” 8th AIAA Atmospheric and Space Environments Conference, June 13-17, Washington, DC, AIAA-2016-3590.
- [45] Anderson, D. N., Hentschel, D. B., and Ruff, G. A., 1998, “Measurement and Correlation of Ice Accretion Roughness,” NASA CR-2003-211823.
- [46] The International Association for the Properties of Water and Steam, 2007, “Revised Release on the IAPWS Industrial Formulation 1997 for the Thermodynamic Properties of Water and Steam,” <http://www.iapws.org/>.
- [47] White, F. M., 2006, *Viscous Fluid Flow*, 3rd Ed, Boston, McGraw-Hill, Inc., New York, NY.
- [48] Wilke, C. R., 1950, “A Viscosity Equation for Gas Mixtures,” *Journal of Chemical Physics*, **18**(4), pp. 517-519.
- [49] Coleman, H. W., and Steele, W. G., 1999, *Experimentation and Uncertainty Analysis for Engineers*, 2nd ed., John Wiley and Sons, Inc., Hoboken, NJ.

- [50] Kline, S. J., and McClintock, F. A., 1953, "Describing Uncertainties in Single-Sample Experiments," *Mechanical Engineering*, **75**, pp. 3-8.
- [51] McCarrell, J., 2017, "Convection from Laser-Scanned Ice Roughness at Multiple Accretion Event Times," MS thesis, Department of Mechanical Engineering, Baylor University.